Linear changes/trends in stratospheric O_3 and BrO as seen by SCIAMACHY limb measurements during the decade 2002-2012

Dissertation
zur Erlangung des Grades Dr. rer. nat.
am Fachbereich Physik der Universität Bremen

vorgelegt von

Dipl. Phys. Claus Gebhardt

Institut für Umweltphysik,
Fachbereich 1, Physik und Elektrotechnik,
Universität Bremen

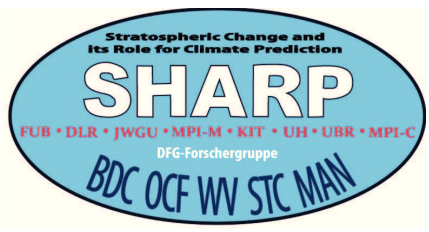

1. Gutachter	:	Prof. Dr. J. P. Burrows
2. Gutachter	:	Prof. Dr. O. Schrems
weitere Prüfer	:	Dr. H. Fischer, Dr. habil. V. Perlick

Eingereicht am	:	06.06.2014
Tag des Promotionskolloquiums	:	29.08.2014

Abstract

The stratospheric O_3 layer is known to undergo changes on decadal time scale. In recent times, one potential driver for increases of stratospheric O_3 is reduced O_3 depletion as a result of the gradual decline of the stratospheric halogen load, which is generally accepted to be a consequence of the Montreal Protocol of 1986 and its amendments. As the upper stratosphere is highly sensitive to the halogen chemistry, evidence for a turnaround of the halogen driven O_3 depletion is expected to show up there first. Indeed, evidence for a slow-down of the O_3 depletion since the late 1990s was reported in [Steinbrecht et al., 2006; Jones et al., 2009] for the altitude range in question. In addition, dynamical factors are a potential driver of changes in stratospheric O_3 as well. A tendency towards decadal decreases of O_3 in the lowermost tropical stratosphere was reported and attributed to enhanced tropical upwelling in Randel and Thompson [2011].

Brominated species are part of the stratospheric halogen load. Accordingly, they are expected to undergo a long-term decrease as a result of the Montreal Protocol and its amendments. Evidence for the stratospheric bromine load reaching a maximum in the early 2000s and levelling-off or decreasing thereafter was found by Dorf et al. [2006] and Hendrick et al. [2008].

The space-borne spectrometer SCIAMACHY, hosted by the European Research Satellite ENVISAT (2002-2012), performed measurements in different geometries including the limb viewing geometry. Scanning the limb in consecutive vertical steps, vertically resolved information on various atmospheric species is provided by SCIAMACHY. Vertical profiles of O_3 are retrieved over the broad altitude range from 10 to more than 60 km. For BrO, the altitude range of retrieval is 13-33 km. In this thesis, SCIAMACHY limb O_3 in the 15-50 km range and BrO in the 16-26 km range are in the focus. These are altitude ranges of high retrieval sensitivity for both species.

This thesis investigates monthly time series of O_3 and BrO as a function of the altitude and latitude. They extend over the period 08/2002-04/2012. In addition to long-term changes on decadal time-scale, time series of stratospheric O_3 and BrO exhibit various periodic variabilities. In order to account for both, multivariate linear regression is appropriate as method of time series analysis. For the decade from 2002-2012, a combination of linear and periodic regression terms is a sufficiently complete approach. The resulting "linear decadal changes" are synonymously referred to as "trends". Decadal increases/decreases are statistically described by positive/negative trends.

In the tropics and at midlatitudes, vertical profiles of O_3 and BrO trends from

SCIAMACHY are presented and subsequently confirmed by trend comparisons to other instruments:

- For O_3, trends from SCIAMACHY are compared to those from OSIRIS/Odin and EOS MLS, other space-borne limb sounders, and SHADOZ ozonesondes. The comparisons to other limb sounders cover the altitude range 15-50 km and are performed in the tropics and at midlatitudes. The comparison to SHADOZ ozonesondes covers altitudes from 15-30 km and is performed in the inner tropics. Good agreement between SCIAMACHY and the other measurements is obtained in the 20-50 km range and reasonable agreement in the 15-20 km range.
- For BrO, trends from SCIAMACHY are compared to those from OSIRIS/Odin and ground-based measurements at Harestua, Norway. The comparison to OSIRIS/Odin is performed in the tropics at altitudes from 20 to 26 km. The comparison to ground-based measurements is made at the geolocation of Harestua and at the altitude of 21 km. The comparison between SCIAMACHY and OSIRIS/Odin shows good agreement. The ground-based measurements don't confirm the full strength of the negative change of BrO seen by SCIAMACHY.

Sources of error which are relevant to trends from SCIAMACHY are discussed as well (potential instrumental and algorithmic issues are considered).

This is followed by presenting the O_3 and BrO trends seen by SCIAMACHY in a global view. As a function of the latitude and altitude, they are shown from 60°N to 60°S (in the 15-50 km range for O_3 and in the 16-26 km range for BrO):

- Positive O_3 trends in the upper stratosphere extend from the tropics through to the midlatitudes. In the tropics, the observed pattern of O_3 trends is characterised further by a double peak structure of positive trends in the lower stratosphere and a single peak structure of negative trends in the middle stratosphere. At midlatitudes, the O_3 trends exhibit a hemispheric asymmetry in the 25-35 km altitude range with negative trends in the north and positive trends in the south. For the pattern of O_3 trends obtained from SCIAMACHY, atmospheric phenomena potentially responsible are discussed.
- Significant negative BrO trends are seen by SCIAMACHY limb at practically any latitude and altitude. These trends are interpreted in the context of the Montreal Protocol and its amendments.

Periodic variabilities of O_3 and BrO as seen by SCIAMACHY limb are presented further as a function of the latitude and altitude. The consistency with relevant literature is discussed.

Publications and contributions

Journal Publications

Gebhardt, C., Rozanov, A., Hommel, R., Weber, M., Bovensmann, H., Burrows, J. P., Degenstein, D., Froidevaux, L., and Thompson, A. M.: Stratospheric ozone trends and variability as seen by SCIAMACHY from 2002 to 2012, Atmos. Chem. Phys., 14, 831-846, doi:10.5194/acp-14-831-2014, 2014.

Aschmann, J., Burrows, J. P., Gebhardt, C., Rozanov, A., Hommel, R., Weber, M., and Thompson, A. M.: On the hiatus in the acceleration of tropical upwelling since the beginning of the 21st century, Atmos. Chem. Phys. Discuss., 14, 9951-9973, doi:10.5194/acpd-14-9951-2014, 2014.

Oral Contributions to National and International Conferences

Gebhardt, C., Rozanov, A., Weber, M., and Burrows, J. P.: *Stratospheric trends of ozone and bromine oxide from SCIAMACHY limb measurements*. DPG Spring Meeting 2012, 25. – 30.03.2012, Berlin, Germany.

Gebhardt, C., Rozanov, A., Weber, M., and Burrows, J. P.: *A decade of ozone and bromine profiles from SCIAMACHY measured in limb mode*. European Geosciences Union General Assembly 2012, 22. – 27.04.2012, Vienna, Austria.

Gebhardt, C., Rozanov, A., Hommel, R., Weber, M., Burrows, J. P., Degenstein, D., and Froidevaux, L., Thompson, A. M.: *Ozone profile trends from SCIAMACHY satellite observations (2002-2012)*. Quadrennial Ozone Symposium 2012, 27.-31.08.2012, Toronto, Canada.

Gebhardt, C., Rozanov, A., Hommel, R., Weber, M., Burrows, J. P., Degenstein, D., and Froidevaux, L., Thompson, A. M.: *Decadal changes in* $\mathrm{O_3}$*,* $\mathrm{NO_2}$*, and* BrO *from SCIAMACHY limb soundings and inter-instrumental comparisons*. European Geosciences Union General Assembly 2013, 07. – 12.04.2013, Vienna, Austria.

Gebhardt, C., Rozanov, A., Hommel, R., Weber, M., Burrows, J. P., Degenstein, D., and Froidevaux, L., Thompson, A. M.: *Vertically resolved trends in stratospheric ozone seen by SCIAMACHY/ENVISAT from 2002 to 2012*. Davos Atmosphere and Cryosphere Assembly - DACA-13, 08. – 12.07.2013, Davos, Switzerland.

Weigel, K., Rozanov, A., Azam, F., Eichmann, K.-U., Gebhardt, C., Weber, M., Stiller, G. P., Bovensmann, H., and Burrows, J. P.: *Water vapour from SCIAMACHY limb measurements*. SPARC WAVAS Workshop, 4.–6.12.2013, Pasadena, USA.

Poster Contributions to National and International Conferences

Gebhardt, C., Rozanov, A., Hommel, R., Weber, M., and Burrows, J. P.: *Stratospheric ozone profile trends from a decade of SCIAMACHY limb observations*. ESA Atmospheric Science Conference - ATMOS 2012, 18. – 22.06.2012, Bruges, Belgium.

Gebhardt, C., Rozanov, A., Hommel, R., Weber, M., Burrows, J. P., Degenstein, D., and Froidevaux, L., Thompson, A. M.: *Decadal trends in ozone, bromine monoxide, and nitrogen dioxide from SCIAMACHY limb measurements and multi-instrument comparisons*. DPG Spring Meeting 2013, 25.02. – 01.03.2013, Jena, Germany.

Brinkhoff, L. A., Ernst, F., Rozanov, A., v. Savigny, C., Hommel, R., Gebhardt, C., Bovensmann, H., and Burrows, J. P.: *Variability in the stratospheric aerosol load from SCIAMACHY limb-scatter observations*. Davos Atmosphere and Cryosphere Assembly - DACA-13, 08. – 12.07.2013, Davos, Switzerland.

Brinkhoff, L. A., Rozanov, A., Ernst, F., Hommel, R., v. Savigny, C., Gebhardt, C., Bovensmann, H., and Burrows, J. P.: *Variability in the stratospheric aerosol load from SCIAMACHY limb-scatter observations*. ESA Living Planet Symposium 2013, 9 – 13.09.2013, Edinburgh, Scotland.

Brinkhoff, L. A., Rozanov, A., Ernst, F., Hommel, R., v. Savigny, C., Gebhardt, C., Bovensmann, H., and Burrows, J. P.: *Stratospheric Aerosol Extinction from SCIAMACHY*. Stratospheric Sulfur and its Role in Climate (SSiRC), 28 – 30.10.2013 Atlanta, Georgia, USA.

Weigel, K., Rozanov, A., Azam, F., Bramstedt, K., Eichmann, K.-U., Gebhardt, C., Weber, M., Stiller, G. P., Bovensmann, H., and Burrows, J. P.: *Time series of water vapor in the UTLS from SCIAMACHY limb measurements, 2002-2012, analysis and comparisons*. American Geophysical Union Fall Meeting, 9.–13.12.2013, San Francisco, USA.

Weigel, K., Rozanov, A., Azam, F., Bramstedt, K., Eichmann, K.-U., Gebhardt, C., Weber, M., Bovensmann, H., Stiller, G. P., and Burrows, J. P.: *Water vapor time series in the UTLS from SCIAMACHY limb measurements*. European Geosciences Union General Assembly 2014, 27.04. – 02.05.2014, Vienna, Austria.

PICO (=Presenting Interactive COntent) Contributions

Gebhardt, C., Rozanov, A., Hommel, R., Weber, M., Burrows, J. P., Hendrick, F., and Van Roozendael, M.: *Linear changes/trends of stratospheric BrO as seen by SCIAMACHY limb for the decade 2002-12*. European Geosciences Union General Assembly 2014, 27.04. – 02.05.2014, Vienna, Austria.

Contents

1 Introduction **4**
- 1.1 The importance of research studies on the stratospheric chemical composition . . . 4
- 1.2 Motivation of thesis . . . 5
- 1.3 Outline of thesis . . . 6

2 Stratospheric ozone **10**
- 2.1 Ozone in the Earth's atmosphere . . . 10
- 2.2 Transport of O_3 . . . 12
- 2.3 Stratospheric O_3 chemistry . . . 15
  - 2.3.1 Oxygen-only chemistry . . . 15
  - 2.3.2 Homogeneous O_3 chemistry . . . 16
  - 2.3.3 Heterogeneous O_3 chemistry . . . 17
- 2.4 Past and future development of O_3 and ozone depleting substances . . . 18
  - 2.4.1 Stratospheric halogens . . . 18
  - 2.4.2 Stratospheric nitrogen . . . 19
  - 2.4.3 Stratospheric O_3 . . . 19

3 Stratospheric bromine **22**
- 3.1 Stratospheric bromine and its sources . . . 22
- 3.2 Bromine chemistry . . . 23
- 3.3 Temporal evolution of stratospheric bromine . . . 24

4 SCIAMACHY limb measurements **27**
- 4.1 The SCIAMACHY mission from 2002-2012 . . . 27
- 4.2 Scientific objectives of SCIAMACHY . . . 29
- 4.3 O_3 retrieval from SCIAMACHY limb . . . 30
- 4.4 BrO retrieval from SCIAMACHY limb . . . 32

5 Ozone time series from SCIAMACHY **36**
- 5.1 Overview of the time series and their periodic variability . . . 36
- 5.2 The (semi-)annual oscillation in O_3 . . . 37
- 5.3 The quasi-biennial oscillation in O_3 . . . 38
- 5.4 Signatures of the (semi-)annual and quasi-biennial oscillation in O_3 time series from SCIAMACHY limb . . . 39

6 O_3 trends from SCIAMACHY: methods **43**
- 6.1 Concept of decadal linear changes/trends . . . 43

6.2 Statistical trend model used for O_3 time series . . . 44
6.2.1 Overview of terms . . . 44
6.2.2 Linear terms . . . 44
6.2.3 Seasonal terms . . . 45
6.2.4 QBO terms . . . 46
6.2.5 Solar cycle terms . . . 47
6.2.6 ENSO terms . . . 49
6.3 Multivariate linear regression . . . 50
6.4 Regression results for O_3 time series from SCIAMACHY . . . 53
6.4.1 Regression results for selected time series . . . 53
6.4.2 Resulting trend profiles in the tropics and at midlatitudes . . . 63

7 Comparison of O_3 trends between SCIAMACHY and other instruments 68
7.1 Overview of the comparisons . . . 68
7.2 Trend comparison between SCIAMACHY and OSIRIS/Odin . . . 68
7.2.1 OSIRIS/Odin: Instrumentation and data preparation . . . 68
7.2.2 Comparison results . . . 70
7.3 Trend comparison between SCIAMACHY and EOS MLS . . . 72
7.3.1 EOS MLS: Instrumentation and data preparation . . . 72
7.3.2 Comparison results . . . 72
7.4 Trend comparison between 3 instruments: SCIAMACHY, EOS MLS, and OSIRIS/Odin . . . 75
7.5 Trend comparison between SCIAMACHY and ozonesondes . . . 77
7.5.1 Ozonesondes: instrumentation and data preparation . . . 77
7.5.2 Comparison results . . . 78

8 Discussion of error sources 80
8.1 Mispointing of the line of sight . . . 80
8.2 Pressure and temperature . . . 82
8.2.1 Stability of O_3 trends with respect to data unit conversion . . . 82
8.2.2 Auxiliary data on pressure and temperature as a minor source of error . . . 85
8.3 Sensitivity of the O_3 retrieval . . . 85

9 Ozone trends and variabilities from SCIAMACHY in a global view 87
9.1 Overview . . . 87
9.2 Trends and autocorrelation . . . 87
9.3 The amplitude and phase of the annual oscillation . . . 89
9.4 The amplitude of the semi-annual oscillation . . . 93
9.5 The QBO amplitude . . . 95
9.6 The solar cycle and ENSO response of O_3 . . . 96

10 Potential drivers of the observed O_3 trends 100
10.1 Halogen chemistry . . . 100
10.2 The tropical upwelling . . . 101
10.3 Role of the subtropical mixing barriers . . . 102
10.4 Combined effects of the NO_X chemistry and age of air . . . 103

10.5 Role of changes in the stratospheric temperature . . . 105
10.6 Summary . . . 105

11 Trends and variabilities of BrO as seen by SCIAMACHY 108
11.1 Time series . . . 108
11.2 Periodic variabilities of BrO . . . 109
11.3 Time series analysis by multivariate linear regression . . . 111
11.3.1 Regression model for BrO . . . 111
11.3.2 Fit quality . . . 112
11.3.3 Trend profiles at midlatitudes and in the tropics . . . 116
11.4 BrO as seen by SCIAMACHY limb in a global view . . . 118

12 Comparison of BrO trends 121
12.1 Comparison to OSIRIS/Odin . . . 121
12.1.1 Preparation and analysis of data . . . 121
12.1.2 Comparison of time series and trends . . . 123
12.2 Comparison to ground-based measurements at Harestua . . . 125
12.2.1 Ground-based measurements of stratospheric BrO . . . 125
12.2.2 Preparation of data . . . 126
12.2.3 Comparison of time series and trends . . . 128

13 Summary and conclusion 132
13.1 O_3 related chapters . . . 132
13.2 BrO related Chapters . . . 133

1 Introduction

1.1 The importance of research studies on the stratospheric chemical composition

Stratospheric O_3 is a key component for the chemistry and dynamics of the Earth's atmosphere [e.g. Wayne, 2000]. Being a strong absorber in the ultraviolet spectral range of the solar spectrum, it shields the ground and the lower atmosphere from harmful radiation. Incoming solar radiation in the 240-280 nm range is practically entirely absorbed before reaching the ground. UVB radiation in the 280-320 nm range is reduced to biologically compatible levels near the ground. As a result of the absorption of energetic radiation, O_3 is the main heat source of the stratosphere. It is responsible for the stratospheric temperature and drives the stratospheric circulation [e.g. Weber et al., 2011]. Thus, changes in the abundance of stratospheric O_3 are of climatological relevance as well.

Being an atmospheric trace constituent, the abundance of O_3 is sensitive to a variety of factors which are both related to the chemical composition and dynamics of the atmosphere. As a result of man-made changes to the stratosphere, O_3 moved into the focus of research during the last three to four decades. The most prominent example for anthropogenically driven perturbation of O_3 is the Antarctic ozone hole [Farman et al., 1985; WMO, 2011, and references therein]. Since its discovery in the early 1980s, it was regularly observed during southern hemisphere winter and spring. The ozone hole arises from a combination of both chemical and dynamical factors. Anthropogenically released chlorine and bromine compounds play a key role in its formation. Also for the future, stratospheric O_3 is expected to be influenced by anthropogenic forcing. As a result of action undertaken to control the human release of halogen compounds (the Montreal Proto-

col of 1986 and its amendments), a recovery of stratospheric O_3 to pre 1980 levels is predicted [WMO, 2011, and references therein]. This recovery is, however, not expected before the middle of the 21st century. At the end of the 21st century, greenhouse gas induced stratospheric cooling might even have led to higher than pre 1980 levels. This scenario is known as the super recovery of stratospheric O_3. Then and now, O_3 as well as other stratospheric constituents are in the focus of attention and give rise to research activity.

1.2 Motivation of thesis

The stratospheric chemical composition has been monitored for the last few decades by satellite and other measurements. Extensive data records on O_3 and other stratospheric constituents are available. Analysing related time series by multivariate linear regression, trends have been widely inferred to characterise the temporal change of stratospheric species [WMO, 2011, and references therein]. In addition to the trend terms, the regression models used typically include further terms which approximate periodic variabilities of stratospheric species. The autocorrelation of the noise, i.e. the fit residuals, is accounted for as well.

Various studies inferred O_3 trends from vertically resolved satellite datasets. With SAGE II and HALOE, two satellite instruments providing vertically resolved O_3 data ceased operation in 2005. This led to discontinuity in trend studies on vertically resolved O_3 [WMO, 2011]. With respect to other profiling satellite instruments, major concerns were that their measurement technique was still under test and the length of their record not sufficient to allow for studies on long-term changes in O_3. Thus, analysing datasets merged between different instruments came into the focus. In Jones et al. [2009], O_3 trends from a merged dataset including a range of profiling satellite instruments within the period 1979-2008 were investigated. SCIAMACHY/ENVISAT, OSIRIS/Odin, and SMR/Odin contributed data to their analysis in the years after 2002 and 2001, respectively, and were proven to agree with one another to a high extent. Further trend studies on merged datasets have been made [Randel and Thompson, 2011;

Kyrölä et al., 2013; Sioris et al., 2014] or are underway [Bourassa et al., 2014]. In recent times, trend studies were conducted on the basis of the decadal data records from SCIAMACHY/ENVISAT and MIPAS/ENVISAT as well [Gebhardt et al., 2014; Eckert et al., 2014]. These studies focused on unmerged satellite data within the decade 2002-2012.

This thesis investigates trends in stratospheric O_3 seen by SCIAMACHY limb measurements by using the method of multivariate linear regression. For the record from SCIAMACHY limb, the maximal time series length possible is limited by the duration of SCIAMACHY: August 2002 to April 2012, i.e. practically one decade. Previously, the study of Mieruch et al. [2012] inferred O_3 trends from SCIAMACHY limb for purposes of validation covering only the shorter period from 2002 to 2008. Here, the full record of SCIAMACHY is studied. Two other limb measuring satellite instruments, which have similar vertical resolution and sampling patterns, are selected to consolidate our findings by trend comparisons to SCIAMACHY.

Establishing a robust set of O_3 trends is further a solid basis for trend studies on other species retrieved from SCIAMACHY limb like BrO, NO_2, aerosol, etc.. In this thesis, BrO is included as well. A comprehensive analysis of BrO trends is performed.

1.3 Outline of thesis

This thesis is divided into 3 parts. Part I (Chapters 2 and 4) gives a concise overview of the fundamentals. Part II (Chapters 5 to 10) comprises the O_3 related chapters. Part III (Chapters 11 to 13) includes the BrO related chapters, and also the conclusive summary of both O_3 and BrO related chapters.

In Chapters 2 and 3, O_3 and BrO in the Earth's stratosphere are introduced. Basic aspects of the atmospheric chemistry of these species are described. Chapter 4 is dedicated to the SCIAMACHY instrument with focus on its measurements in limb viewing geometry.

Chapters 5 to 8 focus on the time series of stratospheric O_3 from

SCIAMACHY limb at latitude bands which are representative for the midlatitudes and tropics. In Chapter 5, decadal time series of O_3 from SCIAMACHY limb are presented for selected altitudes through the stratosphere. Periodic variabilities of O_3 reflected by the time series are explained. In Chapter 6, the statistical modelling of O_3 time series is introduced. The components of statistic regression models accounting both for linear changes/trends and periodic variabilities of O_3 are described. The regression terms are demonstrated to model the time series under investigation appropriately by applying the method of multivariate linear regression, which is also explained. For the tropics and midlatitudes, vertical profiles of O_3 trends from SCIAMACHY limb are presented and their robustness is proven by stability tests. In Chapter 7, the O_3 trends from SCIAMACHY are compared to those from other instruments in the tropics and at midlatitudes. Other space-borne limb sounders and balloon-borne ozonesondes serve as comparison instruments. Chapter 8 discusses potential sources of error relevant to trends of O_3 seen by SCIAMACHY limb.

In global view, Chapter 9 presents linear changes/trends, autocorrelations, and periodic variabilities of O_3 as seen by SCIAMACHY limb. The latitude range from 60°N to 60°S and the altitude range from 15-50 km are covered. Findings from other studies on stratospheric O_3 is given attention where relevant. In Chapter 10, atmospheric phenomena are discussed as potential drivers of the observed O_3 trends. Section 13.1 gives a conclusive summary on the O_3 related chapters.

Chapter 11 focuses on the record of BrO from SCIAMACHY limb measurements. Time series are presented for selected latitude bands in the tropics and at midlatitudes. Their periodic variability is explained. Subsequently, a regression model comprising linear and harmonic terms is proven to sufficiently approximate decadal changes and the periodic variability of BrO. Subsequently, the inferred linear changes/trends of BrO are presented as a function of latitude and altitude within the 60°N-60°S latitude range and 16-26 km altitude range. In Chapter 12, comparisons of BrO trends are performed. The trends from SCIAMACHY are compared to those from OSIRIS/Odin, another limb sounder, at tropical latitudes and to those from ground-based measurements at Harestua, Norway. In Section 13.2, the BrO

related chapters are summarised and the resulting BrO trends are interpreted in the context of the Montreal Protocol.

Part I

Fundamentals

2 Stratospheric ozone

2.1 Ozone in the Earth's atmosphere

Oxygen is a prerequisite for life on Earth, e.g. the breathing of O_2. Ozone (O_3) is another oxygen species which is of utmost importance to life on Earth. A detailed description of the molecular properties of O_2 and O_3 can be found in many standard books on molecular physics [e.g. Banwell and McCash, 1994].

The abundance of atmospheric trace constituents is typically expressed as number density or volume mixing ratio. Number density is equivalent with the number of trace gas molecules per cubic centimetre and volume mixing ratio with the fraction of trace gas molecules among all particles in air. Mixing ratios of stratospheric O_3 are typically expressed in units of parts per million (ppmv). 1 ppmv means that one ozone molecule is among one million particles of air. Another quantity is given by total columns of atmospheric trace constituents. They are equivalent with the vertical integration of the number density. Total O_3 is expressed in units of molecules per square centimetre or Dobson units (DU). One Dobson unit is equivalent with an amount of O_3 which would form a 10 µm thick layer under normal pressure and temperature.

The O_3 abundance in the Earth's atmosphere varies with altitude. The largest part of atmospheric O_3 resides in the Earth's stratosphere and minor parts in the lower mesosphere and upper troposphere. A vertical profile of O_3 typical for northern midlatitude conditions is shown in Figure 2.1, both in units of number density and volume mixing ratio. The largest O_3 number densities and, accordingly, the largest part of total O_3 are located in the altitude range from roughly 15 to 35 km. This is commonly referred to as the O_3 layer.

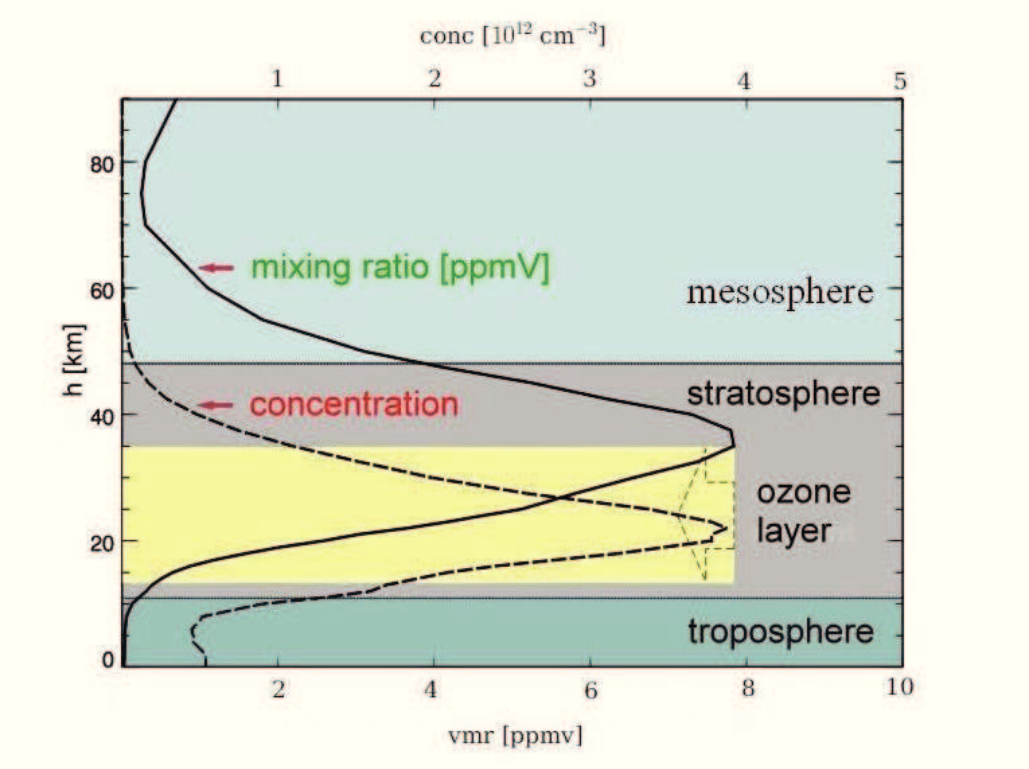

Figure 2.1: O_3 abundance as a function of altitude for typical northern midlatitude conditions [adapted from Kai-Uwe Eichmann, IUP Bremen]. The vertical profile of O_3 is provided both in units of volume mixing ratio and number density. Atmospheric regions such as the troposphere, stratosphere, and mesosphere appear grey and blue shaded. The maximum of O_3 is above 30 km in units of volume mixing ratio and at around 20 km in units of number density. The O_3 layer is highlighted by yellow shading.

In units of volume mixing ratio, the maximum of O_3 typically occurs at altitudes higher than in units of number density. In Figure 2.1, the maximum of volume mixing ratio is above 30 km and the maximum of number density at around 20 km. The altitude of the maximum of O_3 decreases from the tropics towards higher latitudes. As illustrated for number density in Figure 2.2, the maximum is between 25 and 30 km in the tropics and at around 20 km at midlatitudes.

Note that the abundance of O_3 climbs again below 5 km in Figure 2.2. This is a typical indication for the production of O_3 in the lower troposphere due to anthropogenic pollution. The latter may be enhanced by special meteorological conditions like temperature inversions and intense solar radiation. Its most extreme form is the photochemical smog with O_3 being one of the involved species harmful to human health. More information on tropospheric O_3 due to air pollution can be found in Wayne [2000]. O_3 in the lower troposphere

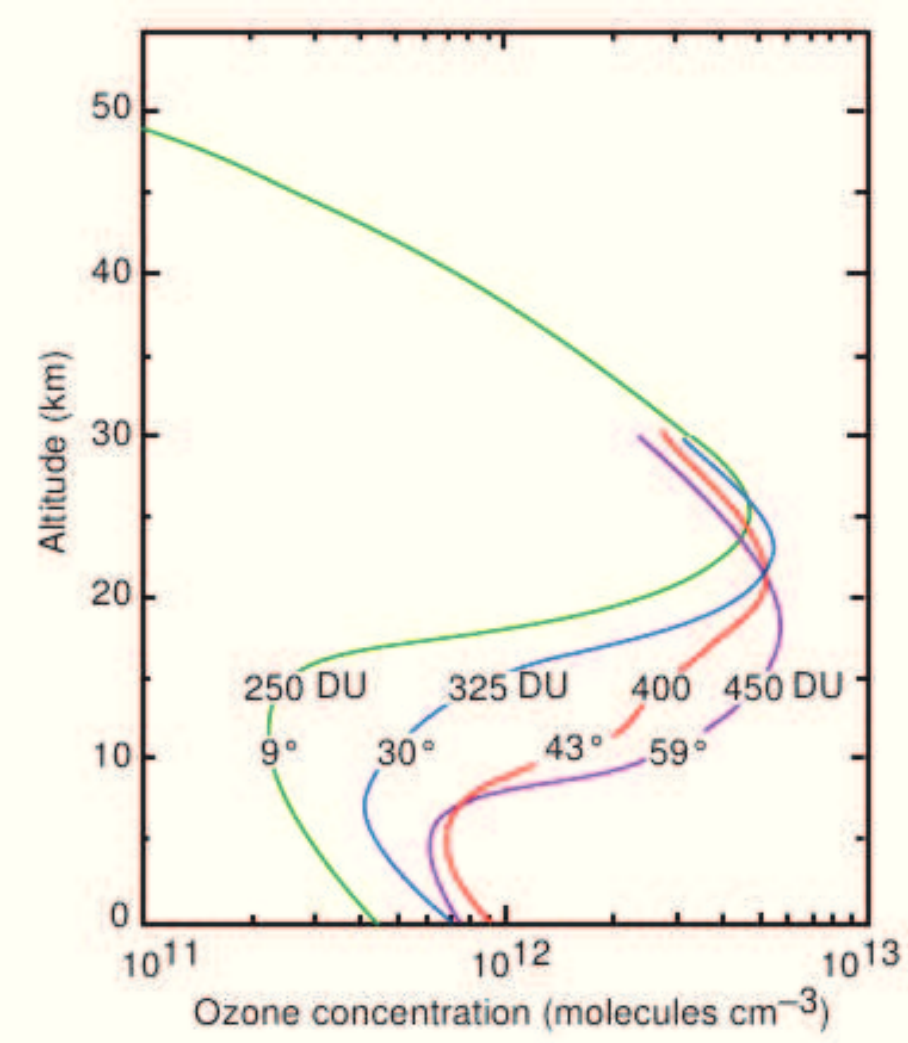

Figure 2.2: Vertical profiles of O_3 typical for the following latitudes in the northern hemisphere: 9°N, 30°N, 43°N, 59°N, [by Wallace and Hobbs [2006]]. O_3 is provided as number density in units of molecules per cm^3. The corresponding total column of O_3 (in Dobson units) is added for each profile. In the tropics at 9°N, the maximum of O_3 is located near 25 km. Towards higher latitudes, the altitude of the maximum of O_3 decreases.

is, however, beyond the scope of this thesis.

2.2 Transport of O_3

As follows from Figure 2.2, the total amount of O_3 at midlatitudes is higher than that in its photochemical source region in the tropics. This is a result of the hemispheric-scale transport of O_3 from the tropics towards the mid- to high latitudes. This meridional transport is historically termed Brewer-Dobson circulation (BDC). The BDC was originally hypothesized to explain measurements of the distribution

of water vapour and O_3 in the stratosphere [Brewer, 1949; Dobson, 1956].

The BDC is a residual circulation pattern [e.g. Andrews, 1987], i.e. it is overlaid to the general stratospheric flow which is in zonal direction. Its drivers are Rossby and gravity waves which originate from orographic forcing and thermal land sea contrast. The waves propagate into the stratosphere and break. At the breaking of waves, easterly momentum is deposited. This decelerates westerly zonal stratospheric flow. As a consequence, a poleward meridional drift of air reestablishes the balance between the Coriolis force and pressure gradient force. By mass continuity, the poleward and downward branches of circulation at higher latitudes are accompanied by vertical ascent of air in the tropics.

As a result of a larger orographic forcing and thermal land sea contrast, the wave activity and the BDC of the northern hemisphere are more pronounced than in the southern hemisphere [Wayne, 2000]. In each hemisphere, the wave activity and, hence, the BDC are strongest in winter time. Another effect of the breaking of waves is the horizontal mixing of air over a broad region in the extratropical winter hemisphere. This horizontally well-mixed region is known as the stratospheric surf zone [Plumb, 2002]. It is limited by the edge of the polar vortex and the subtropical mixing barriers.

As illustrated in Figure 2.3, the overall BDC circulation separates into shallow branches in the lower stratosphere and a deep branch in the winter hemisphere which extends into the upper stratosphere [review in Plumb, 2002]. In addition, a meridional overturning circulation in the mesosphere is directed from the summer pole towards the winter pole. The shallow branches are predominantly driven by synoptic-scale atmospheric waves, the deep branch by planetary scale Rossby waves, and the mesospheric overturning circulation by gravity waves. The propagation of planetary scale Rossby waves into the stratosphere requires westerly wind regimes. This explains the absence of a deep branch of BDC in the summer hemisphere stratosphere. Westerly wind conditions are mainly given in the winter hemisphere stratosphere (the polar night jet is westerly). Similarly, the east and west phases of the quasi-biennial oscillation (QBO) of the tropical

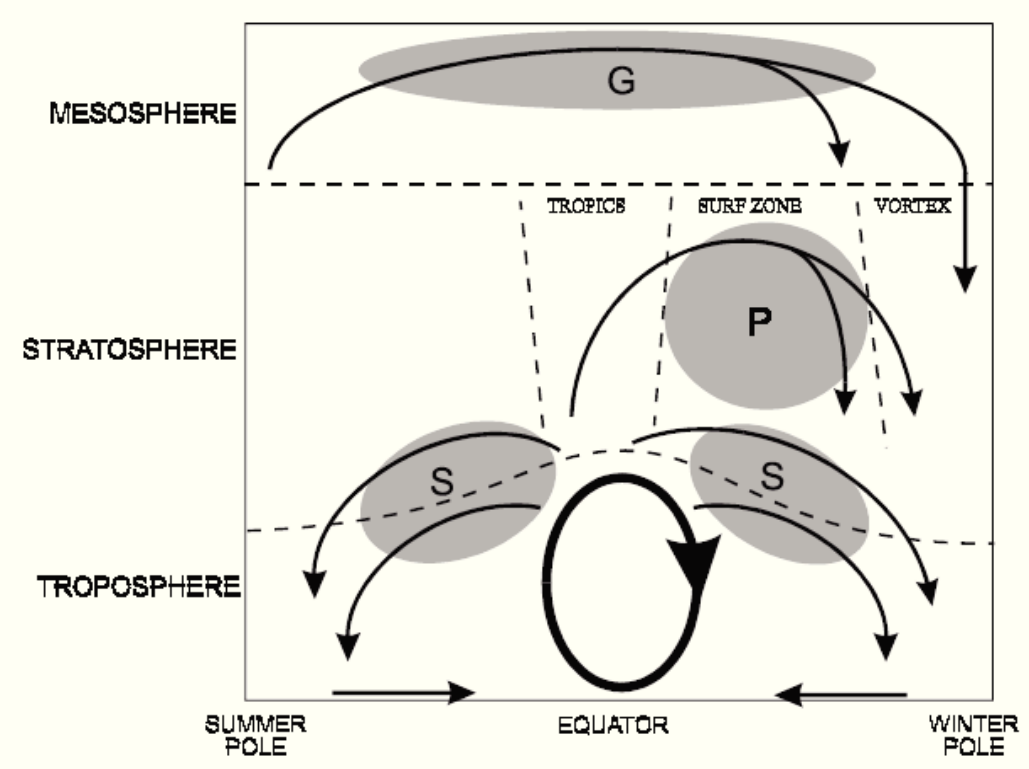

Figure 2.3: Scheme of the Brewer-Dobson circulation [by Plumb [2002]]. In the stratosphere, the BDC consists of shallow branches in the lower stratosphere, in both hemispheres, and a deep branch extending into the upper stratosphere in the winter hemisphere. The meridional overturning circulation in the mesosphere which is directed from the summer pole towards the winter pole. The letters S, P, and G denote the main drivers being synoptic-scale atmospheric waves, planetary scale Rossby waves, and gravity waves, respectively. The stratospheric surf zone, which is limited by edge of the polar vortex and the subtropical mixing barriers is shown as well. Besides, air rising in the tropical troposphere, which is part of the Hadley circulation cell, is indicated.

mid-stratospheric winds modulate the wave propagation [Chen and Huang, 2002]. For easterly QBO phase, the zero wind line (boundary between westerly and easterly winds) is shifted north of the tropics. Accordingly, the wave activity and, hence, the meridional transport of O_3 is enhanced at northern mid- to high latitudes. Thus, the QBO is one driver of the inter-annual variability of the transport of O_3 at higher latitudes. Another contributor is the northern annular mode [Weber et al., 2011, and references therein].

The stratospheric temperature is a key parameter for the atmospheric transport coupling with the O_3 chemistry [Weber et al., 2011]. The BDC is one factor governing the stratospheric temperature. Chemical reactions of the O_3 chemistry are, in turn, temperature dependent. Gas-phase catalytic cycles of O_3 depletion slow down in the case of

reduced temperature. In the future, greenhouse gas induced stratospheric cooling is possible. In combination with enhanced O_3 transport as a result of a future intensification of the Brewer-Dobson circulation, this may give rise to a recovery of stratospheric O_3 towards values higher than those before the anthropogenic depletion of the O_3 layer. This scenario is known as the super recovery of stratospheric O_3.

2.3 Stratospheric O_3 chemistry

2.3.1 Oxygen-only chemistry

The first attempt of theoretical explanation of the existence of a stratospheric O_3 layer was the oxygen-only chemistry proposed by Sydney Chapman in 1930 [Chapman, 1930]. The following reactions, including oxygen species only, were suggested to govern the abundance of ozone:

$$O_2 + h\nu \rightarrow O + O \tag{2.1}$$
$$O + O_2 + M \rightarrow O_3 + M \tag{2.2}$$
$$O_3 + h\nu \rightarrow O + O_2 \tag{2.3}$$
$$O + O_3 \rightarrow 2O_2. \tag{2.4}$$

Reactions 2.1 results in the formation of atomic oxygen (O) by photolysis of O_2 molecules. Reaction 2.2 is termolecular, i.e. involves a third body M, and changes O into O_3. The third body is required for reasons of energy conservation. Typically, atmospheric bulk constituents, such as N_2 and O_2, serve as third body. Reaction 2.3 converts O_3 back to O by photolysis. Reaction 2.4 acts as loss mechanism for O and O_3.

Reactions 2.2 and 2.3 rapidly interconverting O and O_3 gives rise to the concept of odd oxygen, also denoted as O_X. Odd oxygen is the sum O and O_3. For stratospheric altitudes, odd oxygen consists for more than 99% of O_3 and is practically equivalent to O_3 accordingly. Odd oxygen is produced by reaction 2.1 and lost by 2.4.

2.3.2 Homogeneous O_3 chemistry

Homogeneous O_3 chemistry involves gas-phase reactions only. With reaction 2.4 being the only loss mechanism of odd oxygen, the oxygen-only chemistry overestimated O_3 abundances compared to the real atmosphere. Initially, trace gases which are not part of the oxygen-only chemistry were considered not to be able to contribute to O_3 loss. As their abundance is typically by orders of magnitude lower than that of O_3, they were thought to be consumed entirely before having a notable effect on O_3 [Wayne, 2000]. This contradiction was resolved by the discovery of O_3 depletion by catalytic cycles related to the atmospheric hydrogen chemistry [Bates and Nicolet, 1950], nitrogen chemistry [Crutzen, 1970], and halogen chemistry [Stolarski and Cicerone, 1974; Molina and Rowland, 1974].

At the end of each catalytic cycle, odd oxygen has been depleted and the catalytically active species restored. Denoting the catalytic species by Z, catalytic cycles in the stratosphere follow largely this pattern:

$$\begin{aligned} Z + O_3 &\rightarrow ZO + O_2 \\ ZO + O &\rightarrow Z + O_2 \end{aligned}$$

$$\text{Net:} \qquad O_3 + O \rightarrow 2O_2.$$

The dominant catalytic cycles are given by $Z = H$, $Z = HO$, $Z = HO_2$ for the hydrogen chemistry, by $Z = NO$ for the nitrogen chemistry, and $Z = Cl$ for the chlorine chemistry [WMO, 1999]. These catalytic cycles are grouped into the well known HO_X, NO_X, and ClO_X families of catalytic cycles (possibly, also BrO_X is dominant as described below). The abundance of atomic oxygen decreases with decreasing altitude. Particularly below altitudes of ~25 km, catalytic cycles without involving atomic oxygen may gain importance as pointed out by Wayne [2000]. One of these catalytic cycles is the HO_X cycle given by:

$$\begin{aligned} OH + O_3 &\rightarrow HO_2 + O_2 \\ HO_2 + O_3 &\rightarrow OH + 2O_2 \end{aligned}$$

$$\text{Net:} \qquad 2O_3 \rightarrow 3O_2.$$

For maximum conditions of stratospheric halogens (which are still close to today's conditions), the partitioning of ClO_X catalytic cycles at the overall O_3 loss maximises at altitudes of around 40 km [Osterman et al., 1997; WMO, 1999]. There, it is comparable to the partitioning of NO_X and HO_X. The NO_X partitioning becomes dominant at O_3 loss towards next lower altitudes and the HO_X partitioning towards next higher altitudes. At non-polar regions, HO_X is also the dominant species at catalytic O_3 depletion in the lower stratosphere below ∼25 km. Depending on the contribution from very short lived substances (VSLS) to stratospheric bromine, BrO_X may have a partitioning at O_3 depletion similar to that of HO_X in the lower stratosphere [WMO, 2007].

Homogeneous O_3 chemistry prevails at non-polar regions. By contrast, processes of heterogeneous O_3 chemistry are responsible for the formation of the polar O_3 hole as described in the next Section.

2.3.3 Heterogeneous O_3 chemistry

The occurrence of Polar Stratospheric Clouds (PSCs) under conditions given within the polar vortex [Wayne, 2000] is a prerequisite for the formation of the (Ant-)arctic O_3 hole. PSC particles act as surfaces for heterogeneous reactions which release halogens from chemically inactive reservoir species. For instance, ClONO_2 and HCl which are important reservoir species for chlorine undergo the following heterogeneous reaction on PSC particles:

$$ClONO_2 + HCl \rightarrow Cl_2 + HNO_3. \tag{2.5}$$

HNO_3 is trapped by the PSC particles so that the renewed formation of reservoir species is prevented. This process is known as denoxification. Depending on the type of PSC particles (for details see e.g. Wayne [2000]), this may be followed by the sedimentation of the PSC particles. This process is known as denitrification and removes the species needed for the formation of reservoir species more effectively. The chlorine molecules formed are activated by photolysis:

$$Cl_2 + h\nu \rightarrow 2Cl, \tag{2.6}$$

either by the polar vortex extending beyond polar night or sunlight returning in polar spring. As explained in detail in Section 3.2, bromine is released similarly. The chlorine and bromine radicals deplete O_3 by fatal chain reactions which are, in principle, terminated not earlier than at the break-up of the polar vortex in spring. With PSCs occurring at lower stratospheric altitudes, O_3 is typically destroyed for largest parts. This phenomenon is commonly referred to as the O_3 hole. The chain reactions responsible follow mainly the ClO dimer cycle [Molina and Molina, 1987] and the ClO-BrO cycle [McElroy et al., 1986].

2.4 Past and future development of O_3 and ozone depleting substances

2.4.1 Stratospheric halogens

Source gases of stratospheric halogens, in particular chlorofluorocarbons (CFCs), were widely used for industrial purposes. Because of the absence of other sinks for these species, their main removal mechanism is photolysis by intense UV radiation in the stratosphere. CFCs release their halogen radicals when being photolysed. This was first recognised by Molina and Rowland [1974].

The Montreal Protocol of 1986, its adjustments, and amendments aim at a phaseout of the anthropogenic use of chlorine and bromine compounds which are major sources of the stratospheric halogen load. As a consequence of these countermeasures, the stratospheric halogen load reached its maximum in the late 1990s and declined gradually thereafter.

For the upper stratosphere around 40 km, maximum percentage losses of O_3 due to the halogen driven O_3 depletion were predicted by a range of modelling studies starting in the 1970s [e.g. Crutzen, 1974] and subsequently confirmed by various measurements [WMO, 1999, and references therein]. This is because of the aforementioned high sensitivity of O_3 with respect to depletion by catalytic cycles of chlorine at these altitudes. Similarly, evidence for the onset of a

recovery of global O_3 from the halogen impact is expected to show up in the upper stratosphere first.

2.4.2 Stratospheric nitrogen

The main source gas of stratospheric nitrogen is N_2O which is released by microbial activity. In addition to natural sources, N_2O has anthropogenic sources, e.g. fertilizers used in agriculture. In the stratosphere, N_2O is converted to NO_X both by photolysis and reaction with excited atomic oxygen. As a result of the N_2O source being enhanced by anthropogenic activity, NO_X are predicted to increase throughout the 21st century. Related effects on O_3 are expected on centennial rather than on decadal time scale [Jackman et al., 1996; Nevison and Holland, 1997; WMO, 1999].

2.4.3 Stratospheric O_3

In WMO [2007], the following major stages of the recovery of the global O_3 layer from impacts due to anthropogenically emitted O_3 depleting substances (ODS) were defined:

- Stage 1: the slow-down of the O_3 decline,
- Stage 2: the onset of an increase, i.e. a turnaround in O_3, and
- Stage 3: the recovery of O_3 to pre 1980 values.

The evolution of global O_3, based on measurements and model projections into the future, is schematically shown in Figure 2.4: at pre 1980 conditions, global O_3 was not significantly affected by halogens. This initial period is followed by a continuous O_3 decline on decadal time scale which is related to ODS. Stage 1 is marked by significant departures towards smaller values of decline. Significant increases in O_3 are indicative of stage 2. It is evident that stage 3, the recovery of stratospheric O_3, is more in distant than in near future.

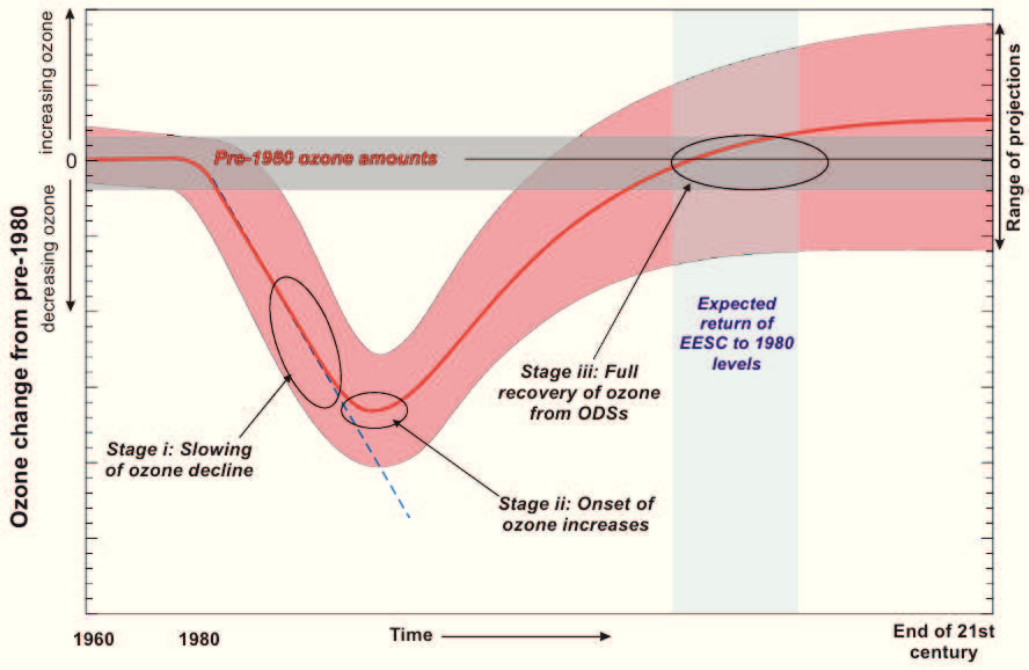

Figure 2.4: Temporal evolution of global O_3 from pre 1980 conditions until the end of the 21st century from a composite of measurements and future projections by models [by WMO [2007]]. The red solid line is the resulting behaviour of O_3 and the red shaded region is the range of variation of the included measurements and model results. Enclosing by black auxiliary lines highlights the onset of the stages of O_3 recovery defined by WMO [2007]: stage i, stage ii, stage iii. (Stage 1, Stage 2, and Stage 3 are used synonymous in the text of this section).

More recent studies concur that stratospheric O_3 is

1. somewhere between stage 1 and stage 2 or
2. these stages are expected to come about within the next 2 decades

as summarised in WMO [2007] and confirmed by follow-on studies. For example:

1. As pointed out in Section 2.4.1, the upper stratosphere is expected to reflect signs for stage 1 and stage 2 first. Indeed, a tendency towards increases of upper stratospheric O_3 was evidenced in the trend studies of Jones et al. [2009] and Steinbrecht et al. [2006]. This is discussed further in Section 10.1.
2. The Antarctic O_3 hole occurs since the 1980s. Variations in the extent of the O_3 hole are driven by interannual variability in dynamical factors rather than declining halogens [WMO, 2007]. This arises from the amount of halogen released to the lower stratosphere in polar winter being more than sufficient for a complete

depletion of its O_3. Model runs reported in WMO [2007] predicted a reduction in the area of the O_3 hole being not statistically detectable before the 2020s.

Similar to the decline of halogens to pre 1980 levels described in Section 2.4.1, stage 3 is not expected to be completed before the middle of the 21st century. Moreover, pre 1980 values of O_3 are likely not be reproduced exactly [e.g. Weber et al., 2011]. The latter arises from potential changes in other atmospheric parameters like the stratospheric temperature and Brewer-Dobson circulation. Due to enhanced greenhouse gases during the 21st century, a cooling of stratospheric temperature and an intensification of the Brewer-Dobson circulation are potential scenarios. With other parameters held fixed, they may result in an acceleration of the O_3 recovery. At the end of the 21st century, O_3 is predicted to exceed pre 1980 values. However, other changes in the stratosphere throughout the 21st century, like an increase in NO_X, may have converse effects on O_3 [Ravishankara et al., 2009]. Note that values of global O_3 at end of the 21st century as suggested by Figure 2.4 are not clearly higher or lower than pre 1980 values within the range of model projections (red shading). In addition, the possibility of the O_3 recovery being delayed by a large volcanic eruption, which is not predictable in advance, is pointed out in WMO [2007].

3 Stratospheric bromine

3.1 Stratospheric bromine and its sources

Compliant with Section 2.4.1, stratospheric bromine originates from tropospheric source gases whose main sink is the photolysis by intense UV radiation. A distinction between 3 major groups of brominated source gases is made [Dorf et al., 2006; WMO, 2011, and references therein]: CH_3Br (methyl bromide), halons, and VSLS (very short lived substances). CH_3Br is both of natural and anthropogenic origin whereas halons are entirely of anthropogenic origin. A major anthropogenic source of CH_3Br is fumigation (quarantine and pre-shipment use) and large natural sources are the ocean, freshwater wetlands, and coastal salt marshes [WMO, 2011, and references therein]. The industrial production of halons began in the 1950s and a large bank of halons is given by fire extinguishing agents. As the sum of CH_3Br and halons is not completely sufficient to account for the entire stratospheric bromine, further sources must exist. These are classified as VSLS (very short lived substances). They include different forms of bromomethane such as CH_2Br_2 and $CHBr_3$ and also larger bromocarbons. Brominated VSLS mainly originate from natural sources. Effective transport pathways into the stratosphere are reported particularly for the longer-lived VSLS, [Aschmann et al., 2009; WMO, 2011].

Anthropogenic contributions are estimated to amount of around 50% of stratospheric bromine at the time of its peak in the late 1990s [Montzka and Fraser, 2003; WMO, 2007, 2011]. The global annual mean surface mixing ratio of CH_3Br reached peak values of around 9.2 pptv in the years 1996-1998. Halons peaked in the years 2005-2008 at values of 8.2-8.5 pptv. The sum of bromine from CH_3Br and halons peaked around 1998 at values of 16.5-17 pptv. The range

of estimates of the VSLS contribution to stratospheric bromine varies between 3 and 8 pptv [WMO, 2011]. An overview of the different contributions to stratospheric bromine, which all originate from the troposphere, is provided in Figure 3.1.

In the lower stratosphere, organic brominated source gases are entirely converted into inorganic bromine. The mechanisms responsible are photolysis and possibly also oxidation by excited atomic oxygen. The total stratospheric inorganic bromine is collectively referred to as Br_y. In the lower stratosphere, the most abundant Br_y species are BrO, BrONO_2, and OHBr [Lary, 1996]. In Section, 3.2 their role in stratospheric bromine chemistry is described in detail.

3.2 Bromine chemistry

The relevance of bromine for stratospheric O_3 chemistry has already been pointed out. It plays a key role in the formation of the (Ant-)arctic O_3 hole as discussed in Section 2.3.3. It is also a contributor to gas phase catalytic O_3 depletion in the non-polar lower stratosphere as pointed out in Section 2.3.2.

The interconversion between radicals and reservoir species is responsible for the diurnal variation of stratospheric bromine. At sunrise, bromine radicals are quickly released as a result of the photolysis of reservoir species like BrONO_2 [Deters et al., 1998; Lary, 1996]. This is accompanied by the renewed formation of BrONO_2 by the following termolecular reaction:

$$BrO + NO_2 + M \rightarrow BrONO_2 + M, \tag{3.1}$$

so that a steady-state occurs during daytime. The steady-state concentrations of BrO and BrONO_2 mainly depend on factors like air density, the NO_2 concentration, and the actinic flux. At daytime, the fraction of BrO to Br_y is on the order of 50 %. Therefore, BrO may be considered as representative for Br_y. After sunset, practically all BrO is converted back to BrONO_2. Over the night, heterogeneous hydrolysis on sulphate aerosols may be responsible for the conversion of BrONO_2 into another reservoir species, namely OHBr [Lary, 1996].

In the polar winter stratosphere, the formation of $\mathrm{BrONO_2}$ is prevented by the uptake of $\mathrm{NO_2}$ by PSC (Polar Stratospheric Cloud) particles [Wayne, 2000]. At polar night, bromine is, thus, mainly present as $\mathrm{Br_2}$ (so far, it is still chemically inactive). With the return of sunlight in polar spring or the polar vortex extending beyond the area of polar night, chemically active bromine radicals are released due to photodissociation. This gives rise to the above mentioned contribution of bromine to the formation of the $\mathrm{O_3}$ hole. The latter arises from combined effects of chlorine and bromine radicals as described in Section 2.3.3.

Both brominated and chlorinated species of anthropogenic origin are understood as the stratospheric halogen load. While chlorine is more abundant in the stratosphere, bromine is more effective at $\mathrm{O_3}$ depletion by a factor of around 60 on a per atom basis [WMO, 2003]. The latter is because brominated reservoir species are less stable with respect to photolysis than their chlorinated counterparts, like $\mathrm{BrONO_2}$ compared to $\mathrm{ClONO_2}$ [Wayne, 2000]. Furthermore, a relatively photostable chlorinated reservoir species is given by HCl, which is formed by the reaction between chlorine and methane [Wayne, 2000]:

$$CH_4 + Cl \rightarrow CH_3 + HCl. \tag{3.2}$$

Contrastingly, the analogous formation of HBr does not take place as the reaction is endothermic. Taken as a whole, stratospheric bromine is, similar to chlorine, of utmost importance with respect to the stratospheric $\mathrm{O_3}$ depletion.

3.3 Temporal evolution of stratospheric bromine

Surface measurements of brominated species, including $\mathrm{CH_3Br}$ and halons, showed maximum values around 1998 and a decline thereafter. In Figure 3.1, the thick blue curve represents bromine from $\mathrm{CH_3Br}$ and the purple curve the sum of bromine from $\mathrm{CH_3Br}$ and halons. Their turnaround close to 1998 is generally accepted to be a direct consequence of the Montreal Protocol and its amendments. Their decrease is quantified as 3-5 % in the years from 1998-2004 in WMO [2007]. This corresponds with roughly 5 % per decade.

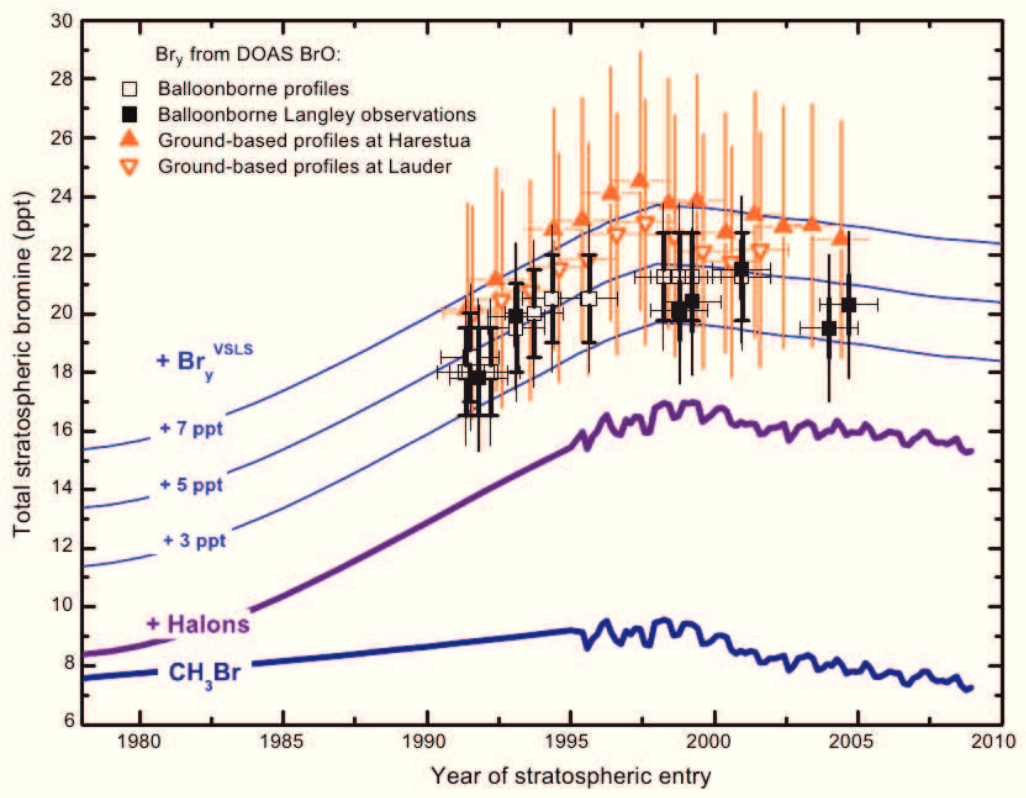

Figure 3.1: Temporal evolution of stratospheric Br_y (units of vmr) from the early 1990s through the mid 2000s [by WMO [2011]]. Triangles represent values based on ground-based measurements from the sites of Harestua (60.2°N, 10.8°E) and Lauder (45.0°S, 169.7°E) [Hendrick et al., 2008]. These are provided as annual means. Squares represent balloon-borne measurements [Dorf et al., 2006]. The global evolution of tropospheric source gases of Br_y is shown as well. The thick blue curve shows $\mathrm{CH_3Br}$ only and the purple curve the sum of $\mathrm{CH_3Br}$ and halons [Butler et al., 1999; Montzka et al., 2003]. The thin blue lines include, in addition to $\mathrm{CH_3Br}$ and halons, constant terms of 3, 5, and 7 pptv, respectively. The latter is in accordance with the range of recent estimates of the VSLS contribution to stratospheric Br_y reported in WMO [2011].

With $\mathrm{CH_3Br}$ and halons being main source gases as described in Section 3.1, stratospheric Br_y is expected to respond to their temporal evolution. Observational evidence for this has been provided by different measurements techniques of stratospheric BrO [Dorf et al., 2006; Hendrick et al., 2008; WMO, 2011]. The ground-based record of Hendrick et al. [2008] shows a turnaround in 2001 and significant negative trends thereafter. While these ground-based data are bound to the geolocations of Harestua (Norway) and Lauder (New Zealand), the balloon-borne record of Dorf et al. [2006] comprises composite data from balloon campaigns at various geolocations. It, thus, represents a wide range of geoconditions, but has a less regular temporal sampling as only few balloon campaigns were conducted per year. The

balloon-borne record of Dorf et al. [2006] indicates a slowdown in the increase of BrO after the early 2000s (a quantification was not made).

The main argument for the attribution of the observed changes in stratospheric BrO to tropospheric changes is that their onset coincides well with the peak of the tropospheric bromine burden around 1998 [Dorf et al., 2006; Hendrick et al., 2008; WMO, 2011]. For this, stratospheric BrO has been converted into Br_y by photochemical modelling and stratospheric air has been dated back to the time of their last residence in the troposphere using age of air estimates.

4 SCIAMACHY limb measurements

4.1 The SCIAMACHY mission from 2002-2012

The SCanning Imaging Absorption spectroMeter for Atmospheric CHartographY, briefly SCIAMACHY, performed measurements in 3 viewing geometries, namely the limb, nadir, and occultation geometry. In the limb and nadir geometry, SCIAMACHY detected solar radiation scattered by the atmosphere and reflected by the surface. In the occultation geometry, it observed either the Sun or the Moon and recorded the radiation transmitted through the atmosphere. The measurements covered the spectral range between around 200 and 2400 nm including ultraviolet, visible, and near infrared light.

SCIAMACHY was an eight-channel spectrometer. The full spectral range was divided into eight science channels with spectral resolutions between 0.2 and 1.5 nm. An overview of the science channels, their spectral ranges, and spectral resolutions is provided in table 4.1. Detailed information on the instrumental design of SCIAMACHY and its orbital sequence of measurements can be found in Gottwald and Bovensmann [2011].

channel	spectral range in nm	spectral resolution in nm
1	214-334	0.24
2	300-412	0.26
3	383-628	0.44
4	595-812	0.48
5	773-1063	0.54
6	971-1773	1.48
7	1934-2044	0.22
8	2259-2386	0.26

Table 4.1: Science channels of SCIAMACHY, their spectral ranges, and spectral resolutions [Gottwald and Bovensmann, 2011].

SCIAMACHY was hosted by the European environmental research satellite ENVISAT launched at March, 1st 2002. Following a sun-synchronous orbit with an inclination of 98°, ENVISAT crossed the equator in descending node at 10 AM local time. Accordingly, the limb measurements of SCIAMACHY at the dayside of the orbit, which are the basis for this thesis, extended deeply into both hemispheres. SCIAMACHY went into routine operation in August 2002. It remained in operation without major interruption for almost one decade until the abrupt loss of ENVISAT due to a fatal spacecraft failure on April, 8th 2012.

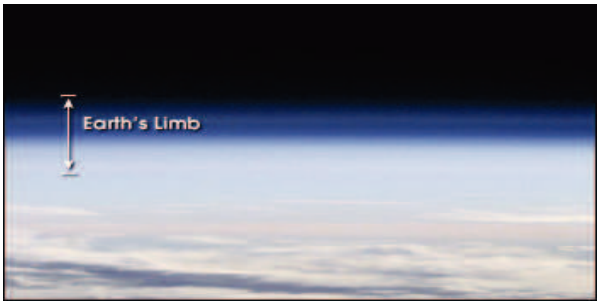

Figure 4.1: The Earth's limb [source: http://earthobservatory.nasa.gov/Features/SOLSE/].

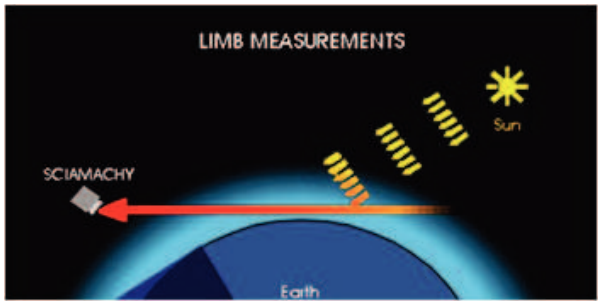

Figure 4.2: Limb viewing geometry of SCIAMACHY [by IUP Bremen, http://www.iup.uni-bremen.de/sciamachy/instrument/modes/index.html].

The instantaneous field of view of SCIAMACHY was approximately 103×2.6 km (across track $\times$ height) at the tangent point area. In limb viewing geometry, the line of sight pointed towards the Earth's limb (see Figures 4.1 and 4.2) and performed a series of horizontal scans with the tangent height increasing in steps of 3.3 km. At the dayside of the orbit, a scan sequence ranged from -3 to 92 km (0 to 92 km since October 2010). The probed volume of air was around 3280 km ahead of the spacecraft. Limb measurements were accomplished by the synchronised movement of two mirrors, referred to as the azimuthal and elevation scan mirrors (ASM and ESM). The ASM scanned in horizontal direction and the detected light was reflected via the ESM into the spectrometer. After each single scan, the ESM switched to the next tangent height and the movement of the limb mirror was repeated in the opposite direction. The vertical extent of a probed pixel was largely defined by the instantaneous field of view

and the tangent height step. The horizontal extent depended largely on the time after which a readout of the measurement data was made (so called integration time). The resolution of SCIAMACHY limb measurements was thus typically between 3 and 4 km in vertical direction and 240 km across track, i.e. in horizontal direction.

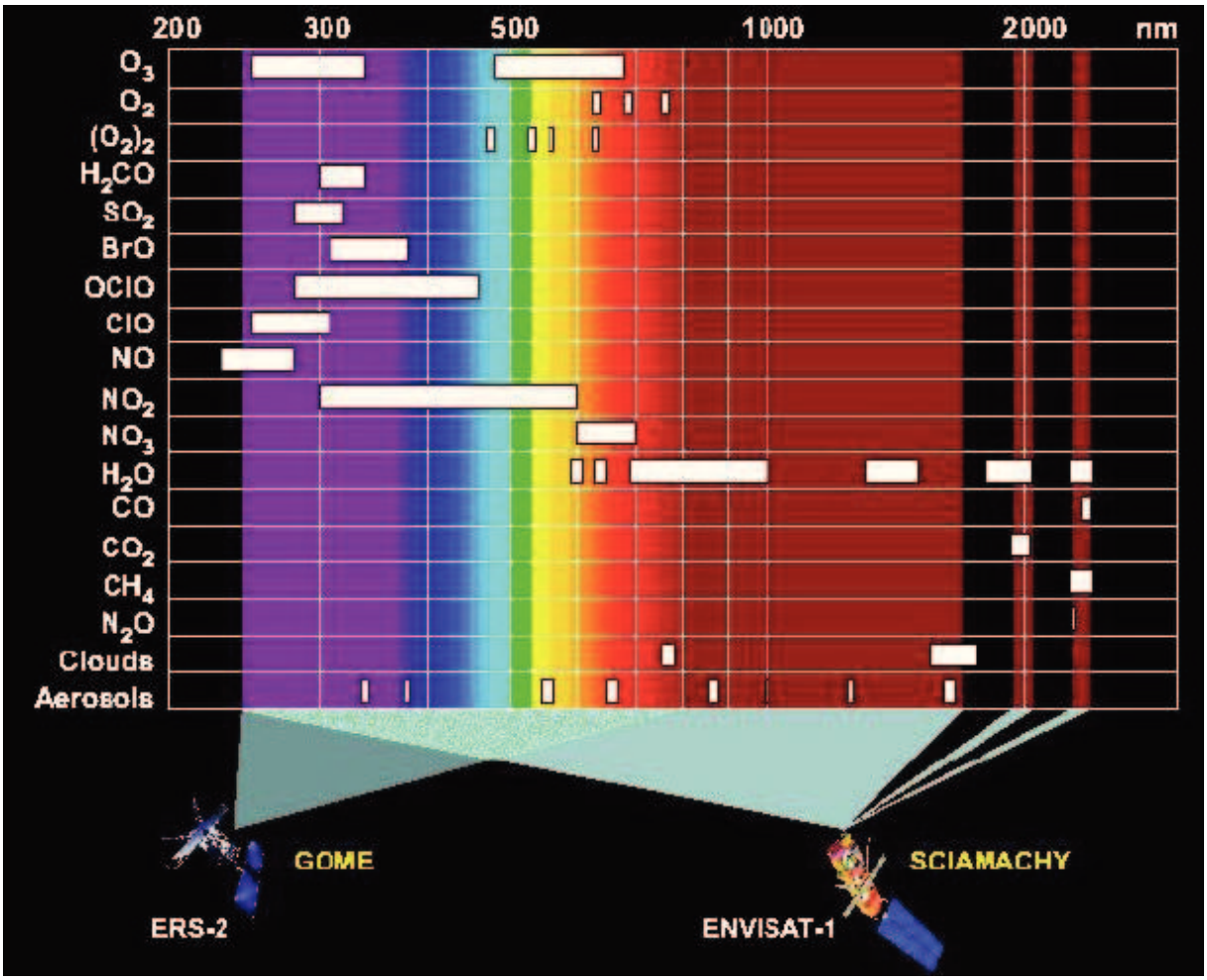

Figure 4.3: The spectral range of SCIAMACHY [by IUP Bremen, `http://www.iup.uni-bremen.de/sciamachy/`]. Wavelengths between around 200 and 2400 nm were covered. For each atmospheric constituent targeted, a typical retrieval wavelength range is highlighted. With GOME [Burrows et al., 1999] (launched in 1995), a smaller scale version of SCIAMACHY had already been operated successfully. The spectral range covered by GOME was around 240-800 nm as also included in the Figure.

4.2 Scientific objectives of SCIAMACHY

The mission objective of SCIAMACHY was the global exploration of trace gases, clouds, and aerosols. This aimed at improving our understanding of chemical and physical processes in the atmosphere and

assess natural and anthropogenically induced changes. The following goals were formulated in Bovensmann et al. [1999]:

- tropospheric pollution arising from industrial activity and biomass burning,
- troposphere-stratosphere exchange processes,
- stratospheric ozone chemistry with focus on the understanding of the ozone depletion in polar regions as well as at midlatitudes, and
- solar variability and special events such as volcanic eruptions, and related regional and global phenomena.

The atmospheric constituents targeted by SCIAMACHY include O_3, O_2, O_4, BrO, OClO, ClO, SO_2, H_2CO, NO, NO_2, NO_3, CO, CO_2, CH_4, H_2O, N_2O, clouds, and aerosols (see also Figure 4.3).

4.3 O_3 retrieval from SCIAMACHY limb

In this thesis, O_3 data from SCIAMACHY limb measurements are based on the scientific retrieval version 2.9 of IUP Bremen. This version is a reprocessing of the earlier version 2.5 using the most recent Level 1 data (V7.04W). With this thesis focusing on stratospheric O_3, version 2.9 may be considered as practically identical to version 2.5. The SCIAMACHY limb O_3 retrieval of version 2.5 employs a non-linear inversion scheme with Tikhonov regularisation [Rahpoe et al., 2013]. Forward modelling is performed by the radiative transfer model version SCIATRAN 3.1 [Rozanov et al., 2014]. In order to account for the non-linearity of the inverse problem, a Gauss-Newton iterative scheme is applied. The native unit of O_3 retrieval is the number density.

For retrieval version 2.5, operational ECMWF data are used as auxiliary data on pressure and temperature. A geographical database [Matthews, 1983] is used to parametrise the surface albedo and ECSTRA (=Extinction Coefficient for STRatospheric Aerosol) climatological profiles [Fussen and Bingen, 1999] as aerosol parametrisation. The absorption cross sections used are from the SCIAMACHY

absorption cross section database, measured by the SCIAMACHY instrument prior to its launch [Bogumil et al., 2003]. The temperature dependence of absorption cross section is accounted for.

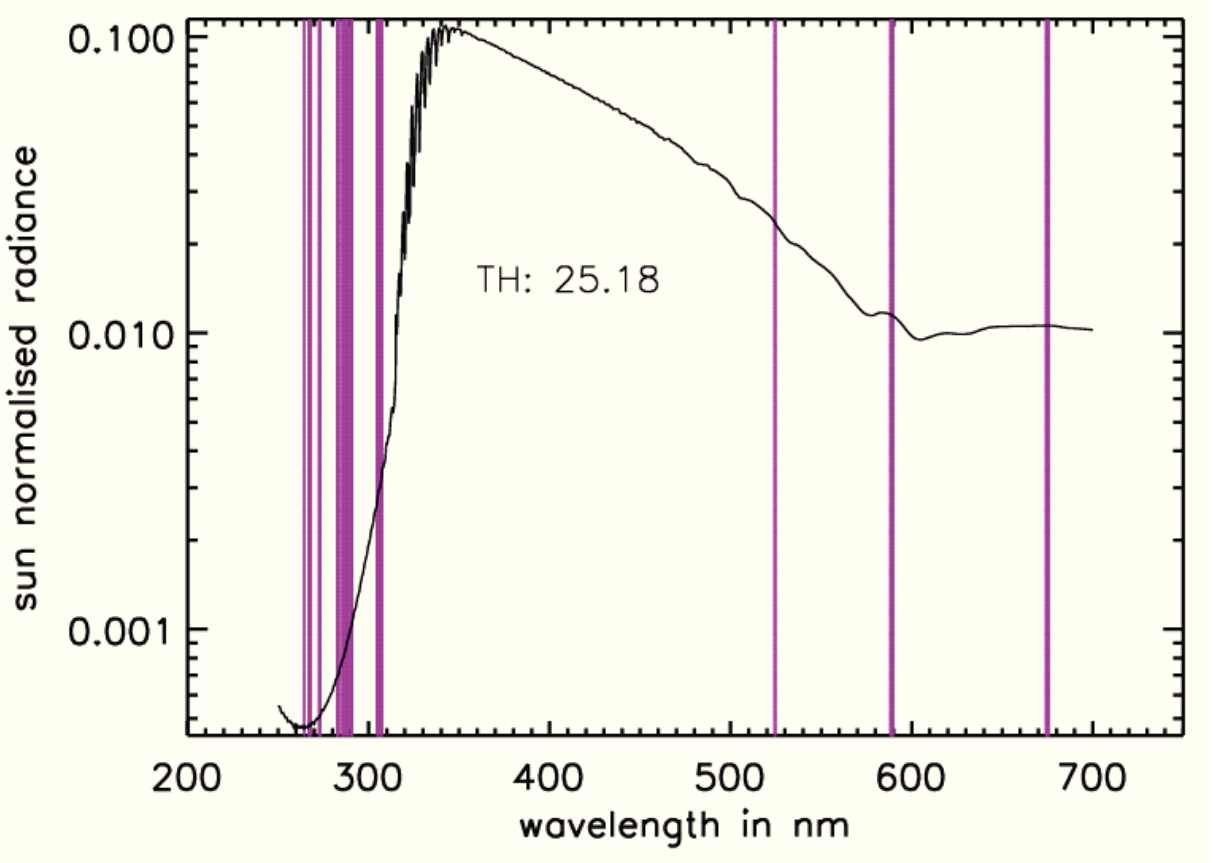

Figure 4.4: Typical spectrum from SCIAMACHY limb measurements. The sun normalised radiance is shown as a function of wavelength for the tangent height of 25.18 km. This is a simulation by the radiative transfer model SCIATRAN (courtesy of A. Rozanov, IUP Bremen). The magenta shaded areas highlight the wavelengths used at O_3 retrieval. They separate into 8 UV and 3 visible wavelengths: 264, 267.5, 273, 283, 286, 288, 290.5, 305, 525, 589, and 675 nm.

Figure 4.4 shows a sun-normalised intensity spectrum typical for SCIAMACHY limb observations: using SCIATRAN, a radiation spectrum for the tangent height of 25.18 km has been simulated. The wavelengths used in O_3 retrieval are $\sim$2 nm wide intervals centred around 264, 267.5, 273, 283, 286, 288, 290.5, 305, 525, 589, and 675 nm. Detailed information on the handling of these wavelengths can be found in Rahpoe et al. [2013]. The visible wavelengths are normalised and combined following the triplet method described in Flittner et al. [2000]. The retrieval information from visible wavelength covers the lower part of the altitude range of the retrieval. The upper altitude limit of previous SCIAMACHY limb O_3 retrieval

versions using visible wavelength only was 35-40 km [Rozanov et al., 2007]. As a result of the combined use of visible and UV wavelengths, O_3 is retrieved up to more than 60 km.

4.4 BrO retrieval from SCIAMACHY limb

BrO is retrieved from SCIAMACHY limb observations in the spectral range of 338-356.2 nm [Rozanov et al., 2011] which is located within the science channel 2 of SCIAMACHY (cf. table 4.1). The measured spectra are normalised with respect to the reference tangent height at around 35 km. The normalisation mainly reduces spectral features related to solar Fraunhofer lines and instrument calibration issues.

Compared to the O_3 retrieval from SCIAMACHY limb measurements described in Section 4.3, the absorption signature of BrO is much weaker. In order to increase the signal to noise ratio, measured spectra are averaged over 4 consecutive azimuthal measurements with each of them having a resolution of around 240 km across track.

The SCIAMACHY limb BrO retrieval consists of 2 major steps such as the preprocessing step and the main inversion step. At the preprocessing step, several spectral corrections are applied to the input spectra accounting for instrumental effects as well as natural phenomena. The instrumental effects include the tilt, I_0-correction, the shift- and squeeze-correction, and polarisation effects. The natural phenomena are related to the Ring effect and broadband atmospheric features like albedo and aerosol.

At the main inversion step, the measurement vector comprises logarithms of normalised limb radiances at all spectral points and tangent heights selected. The method is a global fit approach, i.e. all logarithmic and normalised limb radiances are fitted simultaneously. The fit procedure implies Tikhonov regularisation with a statistical and smoothing constraint. The radiative transfer model SCIATRAN is used to perform forward calculations. Non-linearities are accounted for by a Gauss-Newton iterative scheme. Detailed information can be found in Rozanov et al. [2011].

BrO absorption cross sections following Fleischmann et al. [2004] are used. Their temperature dependence is accounted for. Besides, O_3 and NO_2 absorption cross sections following Bogumil et al. [2003] are included. Operational ECMWF data are used as auxiliary data on pressure and temperature. SCIATRAN is parametrised with aerosol values representing background aerosol conditions.

Part II

Ozone

5 Ozone time series from SCIAMACHY

5.1 Overview of the time series and their periodic variability

The scientific retrieval version 2.9 of IUP Bremen, described in Section 4.3, provides vertically resolved O_3 data from SCIAMACHY limb measurements at the altitudes from 10 to more than 60 km at 1 km vertical steps. As an intermediate retrieval result, the monthly mean O_3 data are binned horizontally into a grid of 15° longitude $\times$ 5° latitude. The grid points comprise single data centred around the longitudes from 0° to 345° and latitudes from -90° to 90°. For the time span 08/2002-04/2012, zonal monthly means are calculated by zonally averaging over the latitude bands of 60°N-50°N, 50°S-60°S, and 20°N-20°S representing the northern/southern midlatitudes and the tropics, respectively.

For zonally and monthly averaged data from SCIAMACHY, each bin typically contains several hundreds of single measurements. The net random error resulting from single profile random errors is negligible. Systematic errors do not follow directly from the data retrieval due to the lack of information on systematic errors. In the following, any time series are presented without specifying any error.

Several periodic variabilities are empirically known to be exhibited by monthly mean time series of stratospheric O_3 including the annual oscillation, the semi-annual oscillation, and the quasi-biennial oscillation (QBO). The QBO is a quasi-periodic signal with its period varying between 2-3 years. Another variability arises from stratospheric O_3 reflecting the 11-year solar cycle. The El Niño Southern Oscillation (ENSO) and volcanic forcing are variabilities potentially showing up

in time series of stratospheric O_3. Focusing here on the time from 2002-2012, ENSO is potentially relevant because of the major ENSO event in 2009/10. Volcanic forcing is, however, considered to be overall of minor relevance as no major eruption occurred during the time span under study.

5.2 The (semi-)annual oscillation in O_3

Detailed information on annual and semi-annual oscillation signatures in stratospheric O_3 can be found in Perliski et al. [1989] and WMO [1999]. These periodic oscillation patterns are governed by transport effects, photochemical O_3 production, and catalytic O_3 depletion. The latter two drivers reflect the temperature dependence of chemical reactions. With temperatures being warmest, both the rates of photochemical O_3 production and catalytic O_3 depletion peak in summer WMO [1999]. As described in the following, photochemical O_3 production gains control over catalytic O_3 depletion in the middle stratosphere.

The findings of Perliski et al. [1989] can be summarised as follows for the midlatitudes: the periodic O_3 variability in the lower stratosphere, roughly limited by pressure levels of 10 hPa (i.e. at altitudes below $\sim$27-28 km), is governed by transport effects in winter leading to an accumulation of O_3 and by catalytic O_3 depletion in summer. This results in an annual oscillation in O_3 with the maximum occurring in late winter/early spring, the descending branch of the annual cycle throughout summer, and the minimum in late summer/early autumn. In the middle stratosphere, roughly limited by pressure levels of 10 hPa (i.e. at altitudes above $\sim$27-28 km), the maximum of the annual oscillation occurs in summer as a result of enhanced photochemical production of O_3. Besides, a semi-annual pattern may result from overlaid catalytic O_3 depletion and transport effects. In the middle to upper stratosphere, the catalytic depletion may lead to a secondary O_3 minimum in summer. In the lower to middle stratosphere, the transport effects may lead to a secondary O_3 maximum in winter. In the upper stratosphere, the effects related to the catalytic O_3 depletion gain control so that the annual minimum occurs

in summer. A semi-annual pattern results from the photochemical O_3 production still being overlaid and responsible for secondary maxima and minima.

In the tropics, a semi-annual oscillation occurs in the middle stratosphere. It is driven by enhanced photochemical O_3 production reflecting two overhead passages of the Sun per year.

In the lowermost tropical stratosphere, O_3 is known to show an annual oscillation. This variability is driven by the tropical upwelling undergoing an annual oscillation and acting on the large vertical gradient of O_3 above the tropical tropopause. The annual oscillation of O_3 is most pronounced in the tropical UTLS (=Upper Troposphere Lower Stratosphere) region between around 16-19 km [Randel et al., 2007]. The annual maximum of the tropical lowermost stratospheric O_3 occurs at the time of the boreal summer.

5.3 The quasi-biennial oscillation in O_3

In the tropical stratosphere, a quasi-periodic variability of the zonal wind speed known as the quasi-biennial oscillation (QBO) is observed [see review in Baldwin et al., 2001]. The zonal wind alternates between east and west phase. The period varies between 2 to 3 years and has an average value of around 28 month. The QBO easterly and westerly wind regimes propagate downwards at an approximate speed of 1 km per month. As described by the thermal wind relation, a temperature oscillation which follows the vertical shear in the zonal wind is induced. Hence, the QBO influences the vertical advection in the equatorial stratosphere, and thus meridional circulation, as well.

The QBO induced meridional circulation modulates the tropical upwelling branch of the Brewer-Dobson circulation. Regimes of easterly wind shear (i.e. easterly winds increase with altitude) are connected with vertical ascent of air and regimes of westerly shear with vertical descent. Thus, easterly shear enhances the tropical upwelling and westerly shear reduces the tropical upwelling. This results in a lofting, i.e. vertical stretching, of the vertical profile of O_3 at easterly shear and in a compacting, i.e. vertical squeezing, at westerly shear

[Butchart et al., 2003]. The largest QBO signatures in tropical stratospheric O_3 occur in the regions of strongest gradients of the O_3 profile, i.e. below and above the O_3 maximum.

The study of Butchart et al. [2003] employed a chemistry climate model which generated the QBO of O_3 on the basis of the vertical advection. With the latter being a key driver, the characteristics of the QBO response of O_3 known from observations were well reproduced. Other drivers potentially relevant are the chemical coupling of O_3 with QBO signatures in NO_Y [Tian et al., 2006] and the radiative feedback of O_3 [Tanii and Hasebe, 2002].

Originating from the modulation of the Brewer-Dobson circulation, the extratropical QBO of O_3 extends into the mid- and high latitudes. In principle, O_3 accumulation in the tropics corresponds with O_3 reduction in the extratropics and vice versa by continuity. Accordingly, a phase change between the tropical and extratropical QBO of O_3 takes place at their transition. With the Brewer-Dobson circulation being stronger in the winter hemisphere, the extratropical QBO response in O_3 is most pronounced in each hemisphere in late winter/early spring [Baldwin et al., 2001].

In the inner tropics, maxima of the QBO response of O_3 are observed in the altitude ranges 20-27 km and 30-37 km [Chipperfield et al., 1994; Baldwin et al., 2001, and references therein]. The Singapore winds are a proxy widely used for QBO signatures in O_3, both in the tropics and extratropics. The Singapore winds are time series of the radiosonde measured stratospheric winds over Singapore [Naujokat, 1986]. They are available from `http://www.geo.fu-berlin.de/en/met/ag/strat/produkte/qbo/`.

5.4 Signatures of the (semi-)annual and quasi-biennial oscillation in O_3 time series from SCIAMACHY limb

Figures 5.1 to 5.8 show the O_3 time series from SCIAMACHY at mid-latitudes (60°N-50°N and 50°S-60°S) and in the tropics (20°N-20°S)

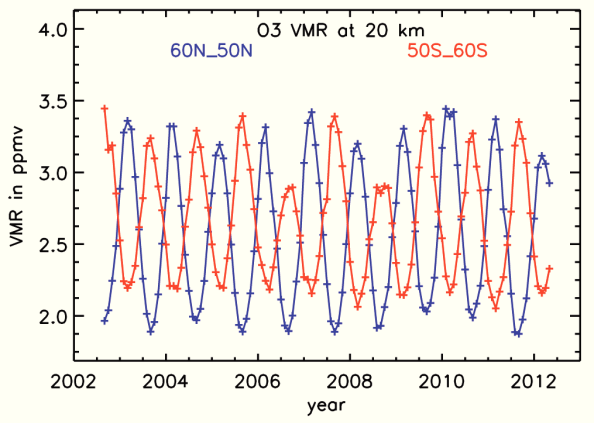

Figure 5.1: SCIAMACHY limb O_3 at 20 km: Time series for 60°N-50°N and 50°S-60°S and the period 08/2002 to 04/2012.

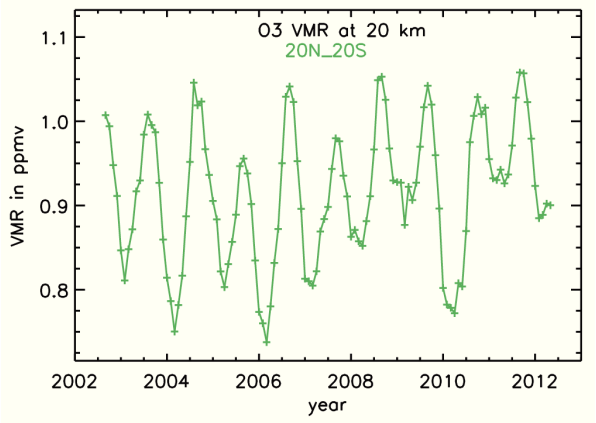

Figure 5.2: Same as figure 5.1 but for 20°N-20°S.

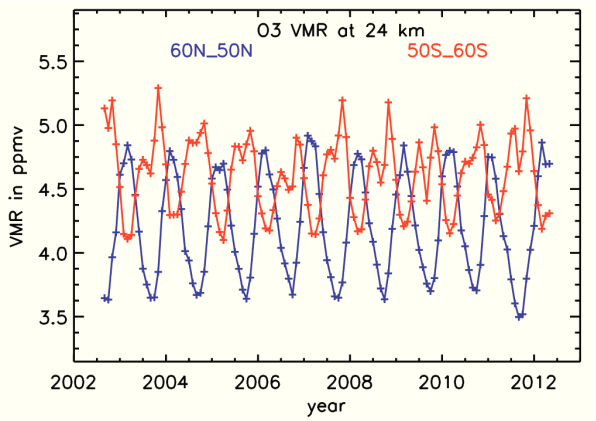

Figure 5.3: Same as figure 5.1 but at 24 km.

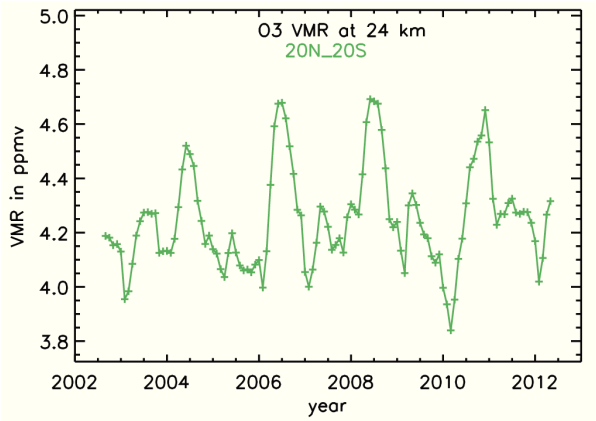

Figure 5.4: Same as figure 5.2 but at 24 km.

at the altitudes of 20, 24, 34, and 44 km. At 20 and 24 km at midlatitudes, the periodic variability of O_3 is dominated by the annual oscillation. As described in Section 5.2, the annual maximum occurs in late winter/early spring as a result of transport effects and the annual minimum in late summer/early autumn as a result of catalytic O_3 depletion. As described in Section 2.2, these transport effects are driven by enhanced wave activity in the winter hemisphere. In the northern hemisphere, the wave activity is stronger than in the southern hemisphere because of larger orographic forcing and thermal land sea contrast. Thus, the annual oscillation observed at northern midlatitudes is of higher amplitude than at southern midlatitudes at 20 and 24 km. In addition, the weaker annual cycle in the south at 24 km

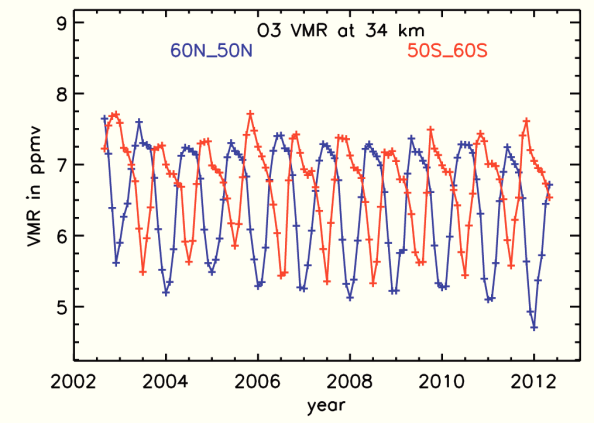

Figure 5.5: Same as figure 5.1 but at 34 km.

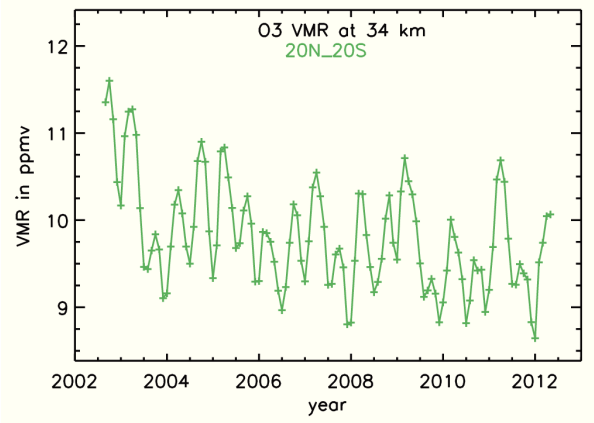

Figure 5.6: Same as figure 5.2 but at 34 km.

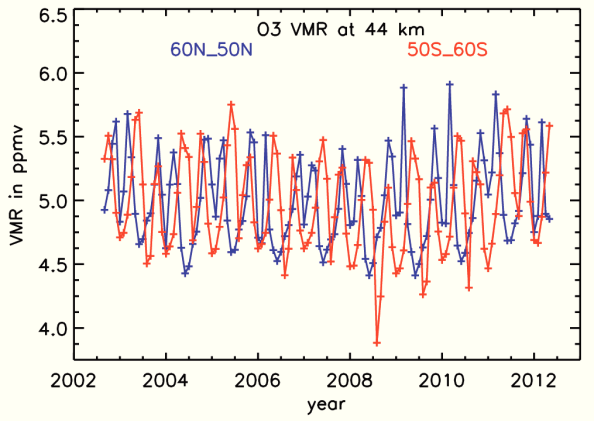

Figure 5.7: Same as figure 5.1 but at 44 km.

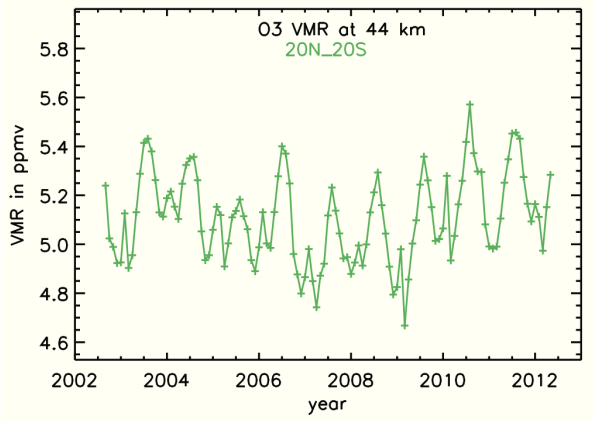

Figure 5.8: Same as figure 5.2 but at 44 km.

is overlaid by photochemical O_3 production leading to secondary O_3 minima in winter. Both at northern and southern midlatitudes, the annual maxima in late winter/early spring exhibit interannual variability. As pointed out in Section 2.2, the latter arises from the fact that the driving wave activity varies from year to year. Thus, the descending branch of the annual cycle of O_3, which extends throughout summer, starts from different initial conditions.

At 34 km at midlatitudes, the photochemical O_3 production has gained control in both hemispheres leading to the maximum of the annual oscillation occurring in late spring/early summer, see Figure 5.5. In both hemispheres, the maxima are flattened by overlaid catalytic O_3 depletion which inhibits further build-up of O_3 during summer. At 44 km, minima of O_3 are observed in winter and also in summer.

At northern midlatitudes, the minima in summer are slightly more pronounced than in winter. This reflects the effects of catalytic O_3 depletion exceeding the effects of photochemical O_3 production at 44 km.

In the tropics at 20 km, an annual oscillation is identified as peaks having their maximum at the time of boreal summer. The amplitude of these peaks varying from year to year is evidence for an overlaid QBO signature. At 24 and 34 km in the tropics, QBO signatures which peak every 2 to 3 years are identified. Both altitudes are within the altitude ranges of the maximum QBO response of tropical O_3 as described in Section 5.3. At 34 km in the tropics, the QBO pattern is modulated by the semi-annual oscillation with peaks of half a year duration.

6 O_3 trends from SCIAMACHY: methods

6.1 Concept of decadal linear changes/trends

A slow-down of the O_3 depletion in response to the onset of a decline of the stratospheric halogen load since the late 1990s has been evidenced by different studies (see also Section 2.4.3 and 10.1). This corresponds with the EESC (equivalent effective stratospheric chlorine, WMO [2007]) proxy undergoing a turnaround. Before and after the turnaround phase in the late 1990s, the EESC proxy is approximately linear (so are its projections into the future) and the associated temporal evolution of stratospheric O_3 may be approximated by linear terms as well.

Statistical models of O_3 time series comprise a range of explanatory variables accounting for both natural and anthropogenically induced variabilities of O_3. During the phase of SCIAMACHY from 2002-2012, relevant explanatory variables approximating natural periodic O_3 variabilities are seasonal variations, the quasi-biennial oscillation (QBO), the solar cycle (SC), and the El Niño Southern Oscillation (ENSO) [WMO, 2007]. As no major volcanic eruptions occurred, volcanic forcing is of minor importance. For the years 2002-2012, long-term changes in O_3 driven by anthropogenically released halogens are appropriately approximated by linear terms as discussed before. In this thesis, a statistical model of O_3 time series including linear terms is employed using the method of multivariate linear regression described in Section 6.3. Analysing time series which are practically of decadal length, the "trends" resulting from the linear terms are synonymously referred to as "decadal linear changes" or briefly "linear changes" in this thesis.

Modelling the long-term changes exhibited by time series of environmental variables as linear is discussed in Weatherhead et al. [1998]. Particular emphasis is given to detecting trends at the 5% significance level. The significance criterion is that the absolute ratio of trend and its uncertainty (1 σ deviation) is larger than 2 [Tiao et al., 1990]. For satellite datasets of total O_3, statistically significant positive trends since the second half of the nineties are reported in WMO [2011] even though statistical significance was predicted by methodological studies not before 2015-2020.

6.2 Statistical trend model used for O_3 time series

6.2.1 Overview of terms

Let Y_t be a general term for any O_3 time series which is under investigation in the following. Only monthly mean time series, i.e. having time steps of 1 month, are considered. The index t denotes the month. O_3 time series from SCIAMACHY from 08/2002 to 04/2012 span 117 months in total, i.e. $t = 0, \ldots, 116$. $t = 0$ represents August 2002 and $t = 116$ represents April 2012. The time series Y_t is approximated by a statistic trend model. In addition to the linear terms, $Lin(t)$, the model has to account for periodic variations such as the annual and semi-annual oscillation, $Seas(t)$, the quasi-biennial oscillation, $QBO(t)$, solar cycle signatures, $SC(t)$, and signatures of the El Niño Southern Oscillation, $ENSO(t)$:

$$Y_t = Lin(t) + \underbrace{Seas(t) + QBO(t) + SC(t) + ENSO(t)}_{periodic} + \underbrace{N_t}_{noise}. \quad (6.1)$$

The remaining portion of the time series Y_t, not approximated by the explanatory variables included into the trend model, is the noise N_t. The noise mainly arises from natural fluctuation.

6.2.2 Linear terms

The linear part of the trend model is given by:

$$Lin(t) = \mu + \omega t, \quad (6.2)$$

with the intercept μ and gradient ω as fit coefficients. The gradient provides the trend. With monthly time series being under analysis, ω represents the slope per month. Here, the slope per decade ($120 \times \omega$) is scaled relative to the mean value of the analysed time series. Thus, any resulting trend is provided in the relative units of % per decade in the following.

6.2.3 Seasonal terms

With exception of the lower stratosphere in the 60°N-50°N latitude band, the seasonal terms $Seas(t)$ accounting for the annual and semi-annual oscillation are harmonics. Beside 6 and 12 months, the periods of 3 and 4 months are included, a sine and cosine term each:

$$Seas(t) = \sum_{j=1}^{4} \left(\alpha_{1j} \sin(\frac{2\pi jt}{12}) + \alpha_{2j} \cos(\frac{2\pi jt}{12}) \right), \tag{6.3}$$

with α_{1j} and α_{2j}, $j = 1, \ldots, 4$, being their fit coefficients. The combination of sine and cosine terms for any period facilitates a flexible adjustment to any phase to be fitted. As the oscillation patterns exhibited by time series are possibly stretched or compressed with respect to a purely harmonic shape, the overtones of 3 and 4 month period improve the overlap between time series and fit curves. This approach allowing for sufficient fit quality is proven is Section 6.4.

In the lower stratosphere of the 60°N-50°N latitude band, a fit proxy is used instead of harmonics in order to account for the interannual variability of the annual cycle of O_3. With the lower stratospheric annual cycle of O_3 having larger amplitude at northern midlatitudes than at southern midlatitudes (see Section 5.4), interannual variability has a larger potential of being modelled insufficiently by a trend model employing harmonics. The cumulative eddy heat flux is a popular proxy for effects which are controlled by variations of the Brewer-Dobson circulation in response to wave forcing [Dhomse et al., 2006; Weber et al., 2011]. Each cumulation comprises 12 months and runs from October until September. Its largest contributions arise from the late winter/early spring months where the wave forcing has its maximum. Thus, the amount of lower stratospheric O_3 accumulation

is proxied individually for each year. Here, the proxy used is based on 50 hPa eddy heat flux values (from ERA-Interim data, area weighted and averaged between 45°N and 70°N). In the following, the cumulative eddy heat flux (CEHF) is fitted instead of harmonic terms in the 60°N-50°N band at altitudes from 15 to 26 km. It is fitted at a time lag of 2 months:

$$Seas(t) = \alpha CEHF(t-2), \tag{6.4}$$

with α being the fit coefficient. The time lag of the proxy and the selected altitude range are based on correlation tests.

6.2.4 QBO terms

As described in Section 5.3, the Singapore winds are extensively used as QBO proxy. Here, two methods of utilising the Singapore winds were taken into account. Either one or two Singapore winds are needed. The Singapore winds are available for different pressure levels up to 10 hPa, which corresponds with altitudes of around 30-31 km in the tropics. At around these altitudes, the 10 hPa Singapore wind is favoured as QBO proxy for modelling QBO signatures in tropical O_3. QBO regimes of wind, which are linked with QBO signatures in O_3 as described in Section 5.3, propagate downwards without any apparent loss of amplitude at speeds of around 1 km per month [Baldwin et al., 2001]. Accordingly, the 10 hPa Singapore wind is expected to be still appropriate as fit proxy at lower altitudes when being time lagged by an appropriate number of months. The optimal time lag may be determined by correlation tests at any altitude. In principle, any Singapore wind may be used like this, e.g. the 30 hPa Singapore wind at altitudes at 23-24 km and below (30 hPa correspond with altitudes of around 23-24 km in the tropics). However, this has limitations at altitudes above 30 km as Singapore winds at pressures of less than 10 hPa are not available.

Alternatively, a combination of the non-time-lagged 10 and 30 hPa Singapore winds may serve as QBO proxy. At the 10 and 30 hPa pressure level, the winds are phase shifted by approximately a quarter of a period. Similar to the combination of sine and cosine described in Section 6.2.3, they are expected to be able to adjust any phase of QBO

signatures of O_3 to be fitted. In principle, this applies in the tropics and extratropics. Also in the extratropics, the Singapore winds are relevant as QBO proxy. For instance, the seasonality of the strength of QBO signatures in extratropical total O_3 has been inferred in [Baldwin et al., 2001] using the 30 hPa Singapore wind.

Comparing both methods for SCIAMACHY limb O_3 in the 20°N-20°S band, they were proven to achieve similar fit quality (not shown) at altitudes below 28 km, where the QBO response of tropical O_3 has one maximum (see Section 5.3). The method of combining the 10 and 30 hPa Singapore winds was tested to be effective at altitudes above 30 km as well, where the QBO response of tropical O_3 has another maximum.

Here, the method of combining the 10 and 30 hPa Singapore winds, $QBO_{10}(t)$ and $QBO_{30}(t)$, as QBO proxy is selected for fitting QBO signatures. In the following, these QBO proxies are included into the trend model (at any altitude and latitude analysed):

$$QBO(t) = \beta_1 QBO_{10}(t) + \beta_2 QBO_{30}(t), \tag{6.5}$$

with β_1 and β_2 being the fit coefficients.

6.2.5 Solar cycle terms

The 11-year solar cycle is a periodic variation in the solar irradiance which is quite pronounced in the UV spectral range with maximum to minimum differences of up to 6% [Gray et al., 2010]. With UV radiation being responsible for the production and loss of O_3, a solar cycle response is shown by stratospheric O_3. Besides, the solar cycle is reflected by stratospheric temperature as well. Based on satellite measurements, it is widely accepted that the solar cycle response of stratospheric O_3 occurs at positive correlation and without time lag [Soukharev and Hood, 2006; Remsberg and Lingenfelser, 2010]. This is consistent to the O_3 solar cycle response shown by a range of chemistry climate models (CCMs) included into SPARC CCMVal [2010]. Similar to the maximum to minimum difference in the solar UV irradiance which has an upper limit of around 6%, the solar cycle response of O_3 amounts for not more than few percent (expressed

as relative difference in O_3 between solar maximum and minimum). Thus, the solar cycle signal is generally of smaller strength than the periodic variabilities of O_3 identified in Section 5.4.

The length of the data record is critical to the identification of the 11 year solar cycle signatures from time series of O_3. Sub-periods of one full solar cycle may capture its descending or ascending branch only which may confound with linear changes/trends. In the time span from 08/2002 to 04/2012, practically one decade, SCIAMACHY has indeed covered almost one full solar cycle: the descending branch of solar cycle 23 which had its maximum in 2001/2002 and the ascending branch of solar cycle 24 which is expected to have reached its maximum in 2012/2013. The study of Soukharev and Hood [2006] suggests further that a time series length close to one full solar cycle is sufficient to obtain realistic estimates of the solar cycle influence exhibited by vertically resolved O_3 datasets: the vertical profile of the solar cycle response of tropical stratospheric O_3 has been inferred from a 25 year SBUV(/2) record covering more than two full 11 year solar cycles. These results were well reproduced when considering two 11 year sub time spans only.

The solar cycle response of O_3 has various proxies including the solar UV flux at 205 nm, Mg II index (Mg II), composite solar Lyman alpha, and 10.7 cm solar flux (F10.7). Their adequacy is proven in Fioletov [2009]. With respect to the 11 year solar cycle response of O_3, no clear preference between the Mg II, F10.7, and composite Lyman alpha could be identified. Generally, these proxies are known to be highly correlated among each other. Here, a monthly mean time series of a multi-instrument Mg II index is used as fit proxy for the 11 year solar cycle signal in SCIAMACHY limb O_3:

$$SC(t) = \gamma Mg\ II(t), \tag{6.6}$$

with γ being the fit coefficient. During the time span under study, it is mainly based on GOME, SCIAMACHY, and GOME2 data, available from `http://www.iup.uni-bremen.de/gome` [Weber et al., 2013].

The data record of satellites indicates the 11 year solar cycle response of O_3 extending from the tropics well into the midlatitudes [Soukharev and Hood, 2006]. In addition, modelling studies resulted

in a rather flat latitudinal structure of the 11 year solar cycle response from the tropics to the midlatitudes and possibly high latitudes [SPARC CCMVal, 2010]. In this thesis, the solar cycle is accounted for in the multivariate linear regression for any time series of O_3 analysed.

6.2.6 ENSO terms

The El Niño Southern Oscillation (ENSO) has its origins in atmosphere ocean coupling in the tropical Pacific region. ENSO warm events are associated with enhanced sea surface temperatures and associated heat release to the atmosphere. Enhancing the upwelling branch of the Brewer Dobson circulation in the tropics, their effects range deeply into the stratosphere [Randel et al., 2009b]. In combination with its positive vertical gradient, lower stratospheric tropical O_3 shows a negative response to enhanced tropical upwelling. Compliant with its large vertical gradient near and above the tropical tropopause, the maximum of the ENSO response of tropical O_3 has been located around 18 km in Randel et al. [2009b]. These findings are consistent with Randel and Thompson [2011] where the largest ENSO signal in tropical O_3 was found in the 17-21 km range.

A plenty of ENSO proxies which is based on measurements of various quantities, ranging from sea surface temperature to total ozone, is in use [Ziemke et al., 2010]. In the following, the Niño 3.4 Index (N34) serves as ENSO proxy at regression. N34 is based on the sea surface temperature anomaly in the Niño 3.4 region (5°N-5°S, 120°W-170°W). During the time span under study, one moderate to strong ENSO warm event occurred in 2009/2010. With El Niño conditions being contrasted by La Niña conditions, N34 has a negative trend as net effect during 2002-2012 (the proxy is not detrended in the following). When including N34 the resulting O_3 trends shift towards smaller positive values in the lower tropical stratosphere as shown in Figure 6.11 (note that the negative behaviour of the proxy translates into a positive behaviour of O_3 as a result the negative ENSO response of lower stratospheric O_3).

Previously, Oman et al. [2013] proved the applicability of N34 to approximate ENSO signatures in vertically resolved satellite datasets

of O_3. Their study used O_3 data from EOS MLS, another limb sounder which has a high temporal overlap with SCIAMACHY and a similar vertical resolution (see Section 7.3). EOS MLS data up to altitudes of roughly 20 km were analysed. In the inner tropics, the O_3 sensitivity to ENSO was found be uniform in longitude at the stratospheric altitudes included. This zonal invariance suggests the N34 index similarly applying to zonally averaged stratospheric O_3. Following Oman et al. [2013], N34 (N34 available from `http://www.cpc.ncep.noaa.gov/data/indices/`, version OISST.v2, anomalies) is employed as ENSO proxy in our regression model.

With increasing altitude, time lags of typically 1-3 months between ENSO proxies and ENSO signatures in O_3 are expected. For instance, the studies of Randel et al. [2009b] and Randel and Thompson [2011] used ENSO proxies time-lagged by 2 months. Here, possible time lags are accounted for by the combined fit of the N34 index and its time derivative:

$$ENSO(t) = c\left[N_{34}(t) + \frac{dN_{34}(t)}{dt}\Delta(t)\right]. \tag{6.7}$$

The results are obtained using an iterative approach. Regression starts with N_{34} and $\frac{dN_{34}(t)}{dt}$ time-lagged by 2 months and is repeated until $\Delta(t)$ approaches a fraction of a month, i.e. a value smaller than 1. The overall time lag approaching a value between 0 and 5 is used as a quality criterion for the regression results. In practice, this does not hold at extratropical latitudes and altitudes above 25 km. Hence, ENSO terms are included at regression at latitudes within 20°N and 20°S and altitudes up to 25 km in the following. Within these ranges, the quality criterion is only very sporadically not given (hence, few gaps are present in vertical trend profiles and latitude altitude plots presented later).

6.3 Multivariate linear regression

From a mathematical point of view, the statistical trend model introduced in Section 6.2 (cf. Eq. 6.1) is a multivariate linear regression model. Here, multivariate linear regression is performed by a general least squares technique which is an iterative use of an ordinary

least squares (OLS) technique. At first, OLS is performed in order to estimate the autocorrelation of noise. This is required for a transformation from correlated to white, i.e. uncorrelated, noise. After this transformation, the final results are inferred by reexecuting OLS. This approach follows Tiao et al. [1990] and Weatherhead et al. [1998].

In matrix notation, Eq. 6.1 is given by

$$\boldsymbol{Y} = \mathbf{X}\boldsymbol{\beta} + \boldsymbol{N}. \tag{6.8}$$

$\boldsymbol{Y}$ is the vector notation of the time series to be modelled and $\boldsymbol{N}$ that of the noise. Both vectors have T elements, which is the time series length (here given as number of months). The t-th line of the matrix $\mathbf{X}$ contains the fit terms for $t \in T$. The vector $\boldsymbol{\beta}$ comprises the fit parameters including the trend ω (cf. Equation 6.2). The ordinary least squares estimator of $\boldsymbol{\beta}$ is determined as follows:

$$\boldsymbol{\beta} = \left(\mathbf{X}^T \cdot \mathbf{X}\right)^{-1} \cdot \mathbf{X}^T \cdot \boldsymbol{Y} \tag{6.9}$$

[Stahel, 2000]. Its covariance matrix is given by

$$\mathbf{Cov}(\boldsymbol{\beta}) = \sigma_N^2 (\mathbf{X}^T \cdot \mathbf{X})^{-1} \,, \tag{6.10}$$

where σ_N^2 represents the variance of the noise. The square root of its i-th diagonal element is the 1σ uncertainty of the i-th component of $\boldsymbol{\beta}$. The criterion for the trend being significantly different from 0 at the 5% significance level (or 95 % confidence level) is the absolute ratio of the trend ω and its 1σ uncertainty σ_ω being larger than 2:

$$\left| \frac{\omega}{\sigma_\omega} \right| > 2 \,. \tag{6.11}$$

For time series of environmental data, it is common practice to assume the noise $\boldsymbol{N}$ an autoregressive process of first order [Tiao et al., 1990; Weatherhead et al., 1998]. The white noise ϵ_t, i.e. the pure random part of the noise, is overlaid by the previous total noise-value N_{t-1} weighted by the autocorrelation coefficient ϕ:

$$N_t = \phi N_{t-1} + \epsilon_t \,, \; |\phi| < 1 \,. \tag{6.12}$$

In general, this approach models various factors influencing the noise which may not all be known to us. The autocorrelation coefficient is

estimated following Edelson and Krolik [1988]. The unbinned discrete correlations at a time lag of 1 are given by:

$$U_{t,t-1} = \frac{N_t N_{t-1}}{\sigma_N^2}. \tag{6.13}$$

The estimator of the autocorrelation ϕ is the average over all $U_{t,t-1}$ available. This applies to time series with and without gaps. For a monthly time series without any gaps, this yields:

$$\phi = \frac{1}{\sigma_N^2} \frac{\sum_{t=2}^{T} N_t N_{t-1}}{T-1}. \tag{6.14}$$

In order to estimate ϕ, Eq. 6.9 is applied to the time series to be analysed. The residuals, which are determined by subtracting the overall regression curve from the time series, give the noise $\boldsymbol{N}$.

Having estimated the autocorrelation ϕ from Eq. 6.14, the transformation from correlated to white noise is performed by the following transformation:

$$\epsilon_t = N_t - \phi N_{t-1} \text{ , } t = 2, 3, \ldots, T. \tag{6.15}$$

This is compliant with Tiao et al. [1990]. For N_1, the transformation is based on the following approximation:

$$\frac{\sigma_\epsilon}{\sigma_N} = \frac{\epsilon_1}{N_1}, \tag{6.16}$$

with σ_ϵ being the standard deviation of the white noise $\boldsymbol{\epsilon}$ and σ_N the standard deviation of the correlated noise $\boldsymbol{N}$. Forming the variance on both sides of (6.12) yields:

$$\sigma_N^2 = \phi^2 \sigma_N^2 + \sigma_\epsilon^2. \tag{6.17}$$

Substituting in (6.16) gives:

$$\epsilon_1 = N_1 \sqrt{1 - \phi^2} \text{ ,} \tag{6.18}$$

compliant with Weatherhead et al. [1998]. In matrix notation, the transformation is:

$$\boldsymbol{\epsilon} = \mathbf{P} \cdot \boldsymbol{N}, \tag{6.19}$$

with

$$\mathbf{P} = \begin{pmatrix} \sqrt{1-\phi^2} & & & & & \\ -\phi & 1 & & & & \\ & -\phi & 1 & & & \\ & & \cdot & \cdot & & \\ & & & \cdot & \cdot & \\ & & & & \cdot & \cdot \\ & & & & -\phi & 1 \end{pmatrix} . \tag{6.20}$$

Multiplying both sides of Eq. (6.8) by $\mathbf{P}$ yields:

$$\boldsymbol{Y}^* = \mathbf{X}^* \boldsymbol{\beta} + \boldsymbol{\epsilon} \, , \tag{6.21}$$

with

$$\boldsymbol{Y}^* = \mathbf{P}\boldsymbol{Y} \, , \tag{6.22}$$

$$\mathbf{X}^* = \mathbf{P}\mathbf{X} \, , \tag{6.23}$$

where the vector $\boldsymbol{\epsilon}$ represents the white noise, which is a requirement for the OLS technique. Repeated use of OLS, following Eq. 6.9 and 6.10, provides the final regression result for β and **Cov**(β) including the trend and its 1σ uncertainty.

With the trend determination performed by the general least squares technique described above, different factors have the potential to influence the detectability of trends. The uncertainty and, thus, also the significance of trend estimates may be sensitive to the autocorrelation and variance of the noise and the length of the data record available [Weatherhead et al., 1998; Tiao et al., 1990].

6.4 Regression results for O_3 time series from SCIAMACHY

6.4.1 Regression results for selected time series

In Figs. 6.1 to 6.8, the SCIAMACHY limb O_3 time series at 20, 24, 34, and 44 km for 60°N-50°N (northern midlatitudes) and 20°N-20°S (tropics) are shown in combination with their regression models. In the top panel, the time series (blue) are provided overlaid by their

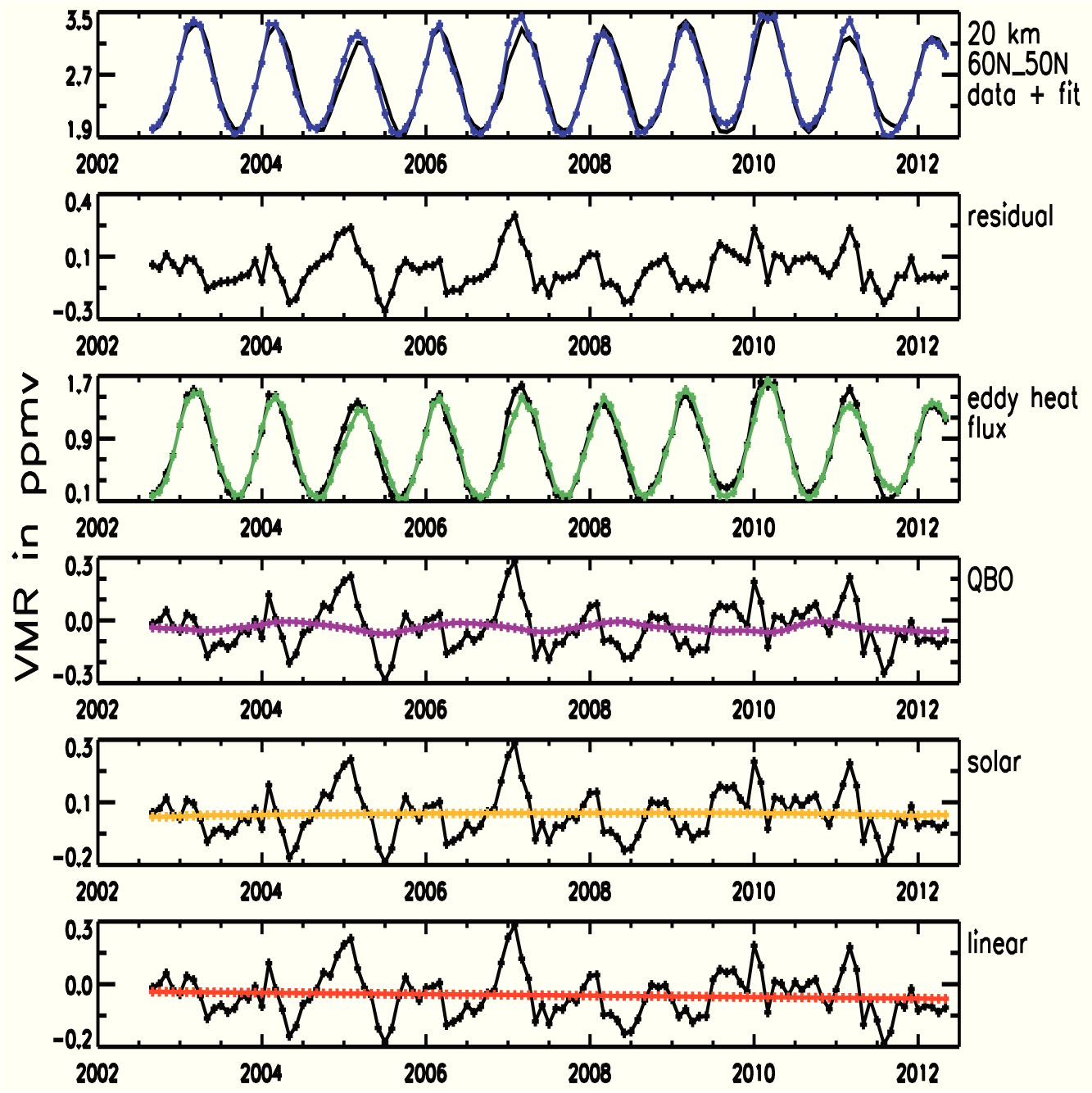

Figure 6.1: Regression model of SCIAMACHY limb O_3 at 20 km and for 60°N-50°N. In the upper panel, the time series (blue) is overlaid by the fit curve (black). Below, the fit residuals are shown. From 3rd panel to bottom, different components of the regression model are shown such as eddy heat flux terms (green), QBO terms (magenta), solar cycle terms (orange), and linear terms (red). Each component of the fit curve is overlaid by the time series with all other components removed.

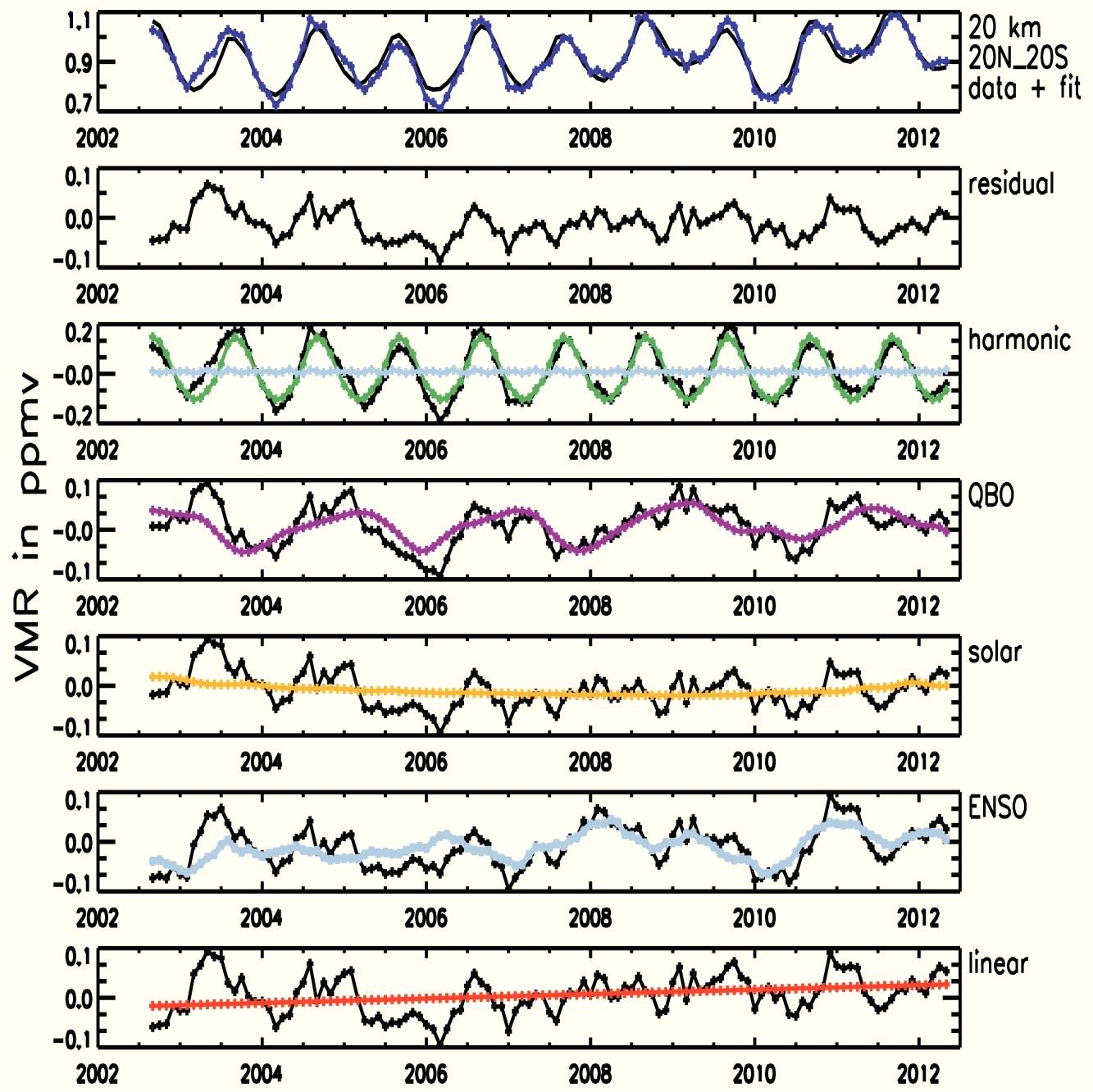

Figure 6.2: Same as Fig. 6.1, but for 20°N-20°S and with harmonic terms instead of eddy heat flux terms. The harmonic terms are provided as combination of all periods included, i.e. 12, 6, 4, and 3 months (green), and as combination of 4 and 3 months only (light blue). In addition, ENSO terms are shown in the last but one panel.

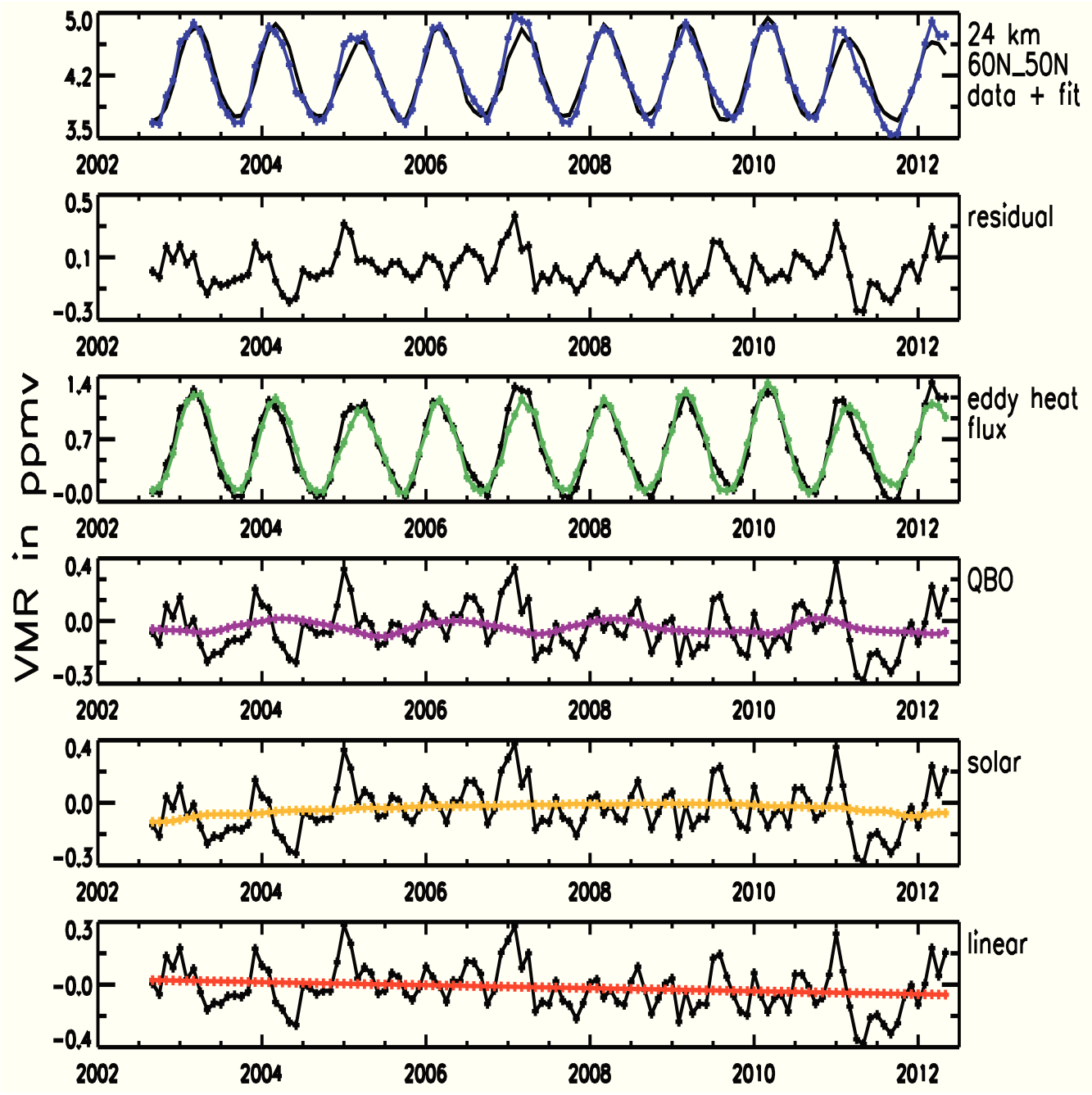

Figure 6.3: Same as Fig. 6.1 but for 24 km.

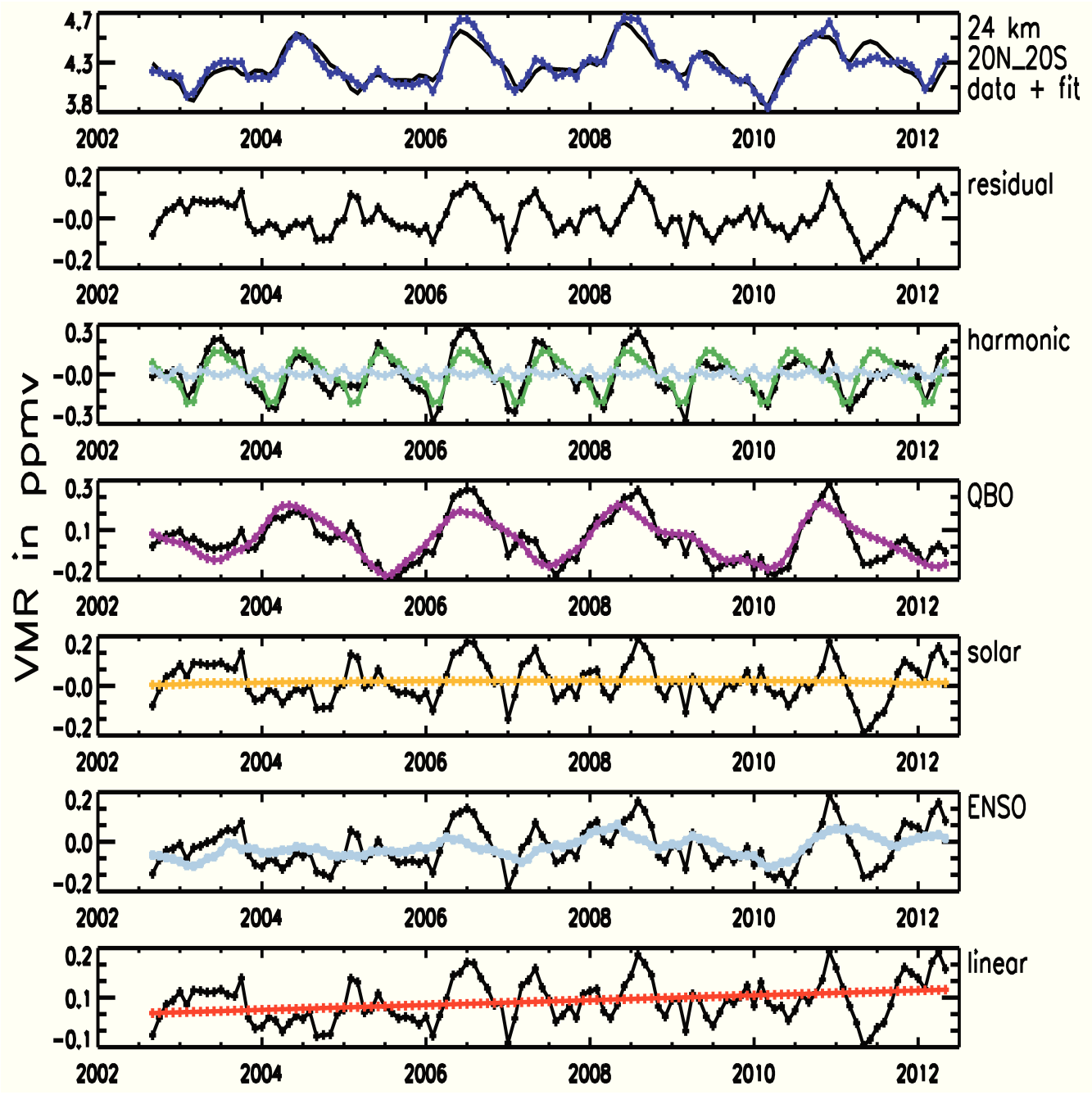

Figure 6.4: Same as Fig. 6.2 but for 24 km.

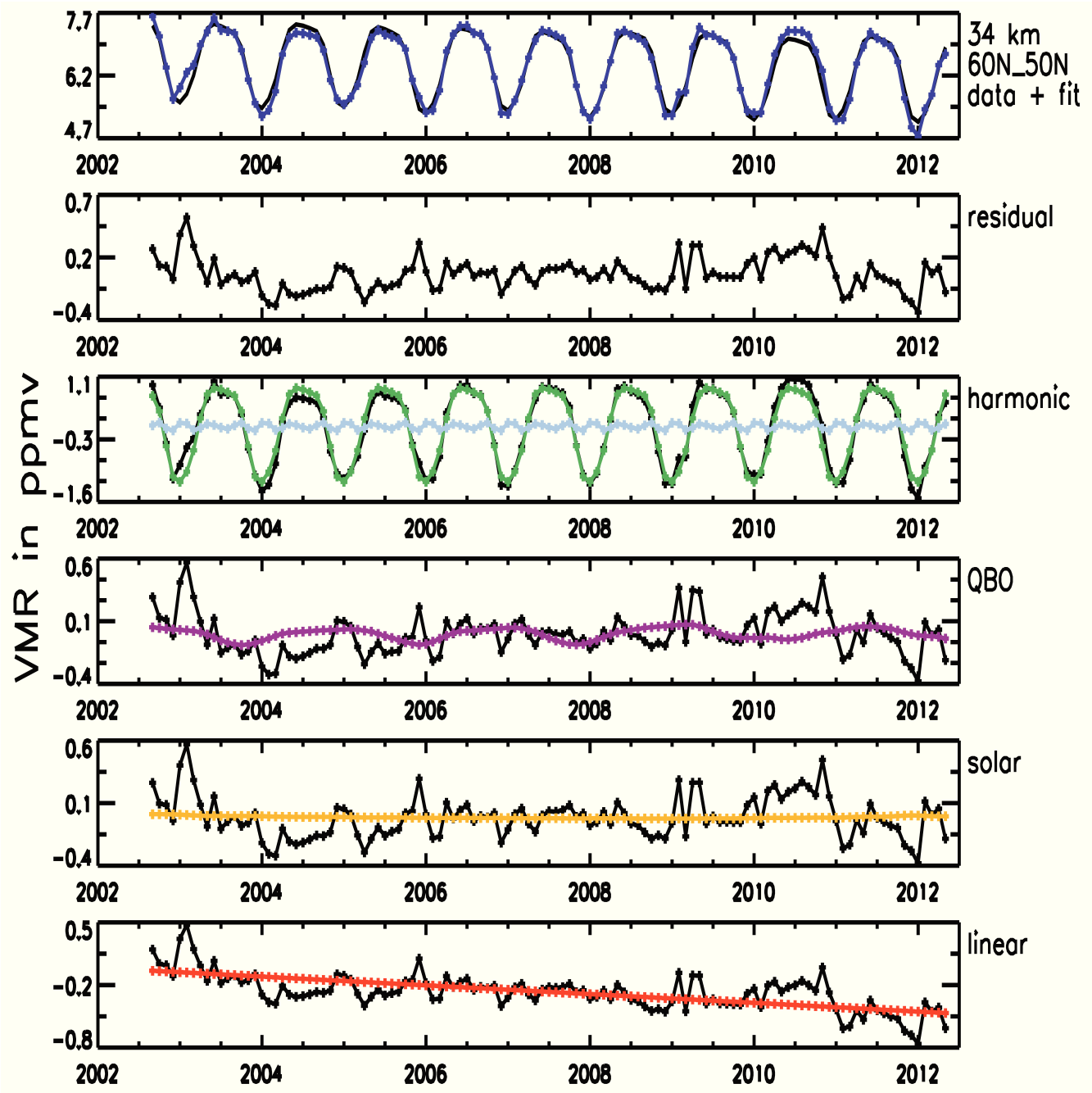

Figure 6.5: Same as Fig. 6.1 but for 34 km and with harmonic terms instead of eddy heat flux terms. The harmonic terms are provided as combination of all periods included, i.e. 12, 6, 4, and 3 months (green), and as combination of 4 and 3 months only (light blue).

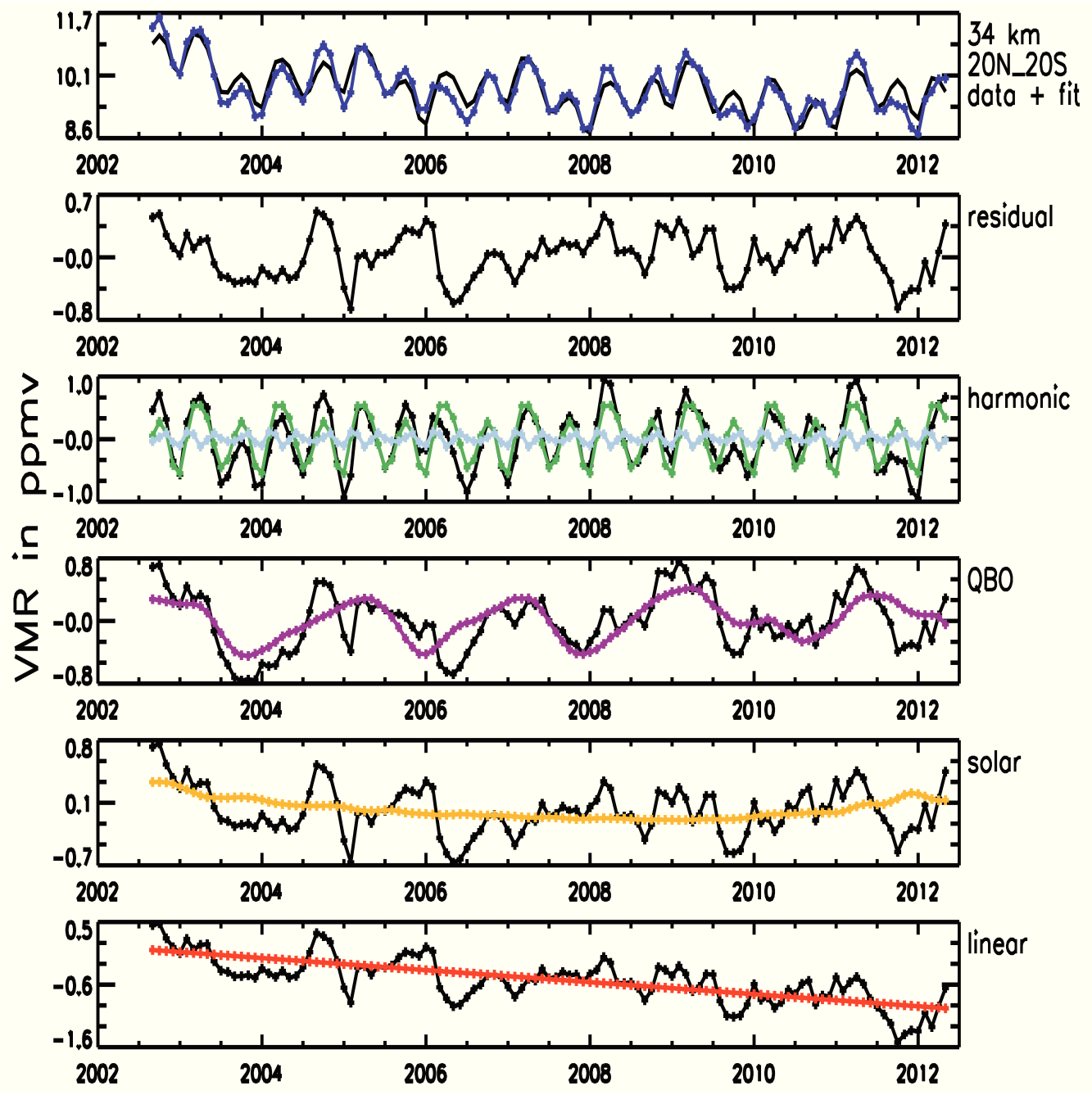

Figure 6.6: Same as Fig. 6.2 but for 34 km (and without ENSO terms).

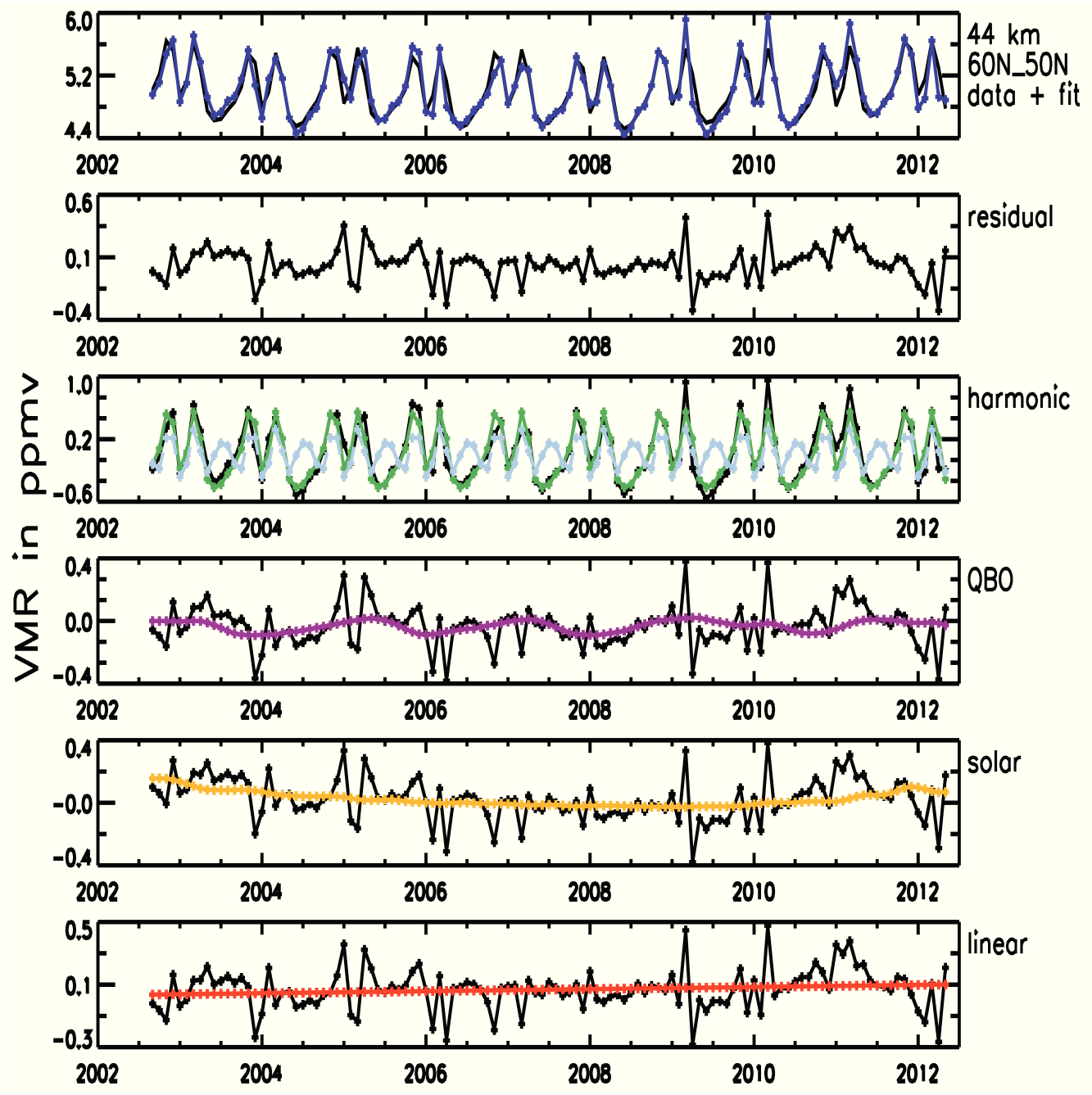

Figure 6.7: Same as Fig. 6.5 but for 44 km.

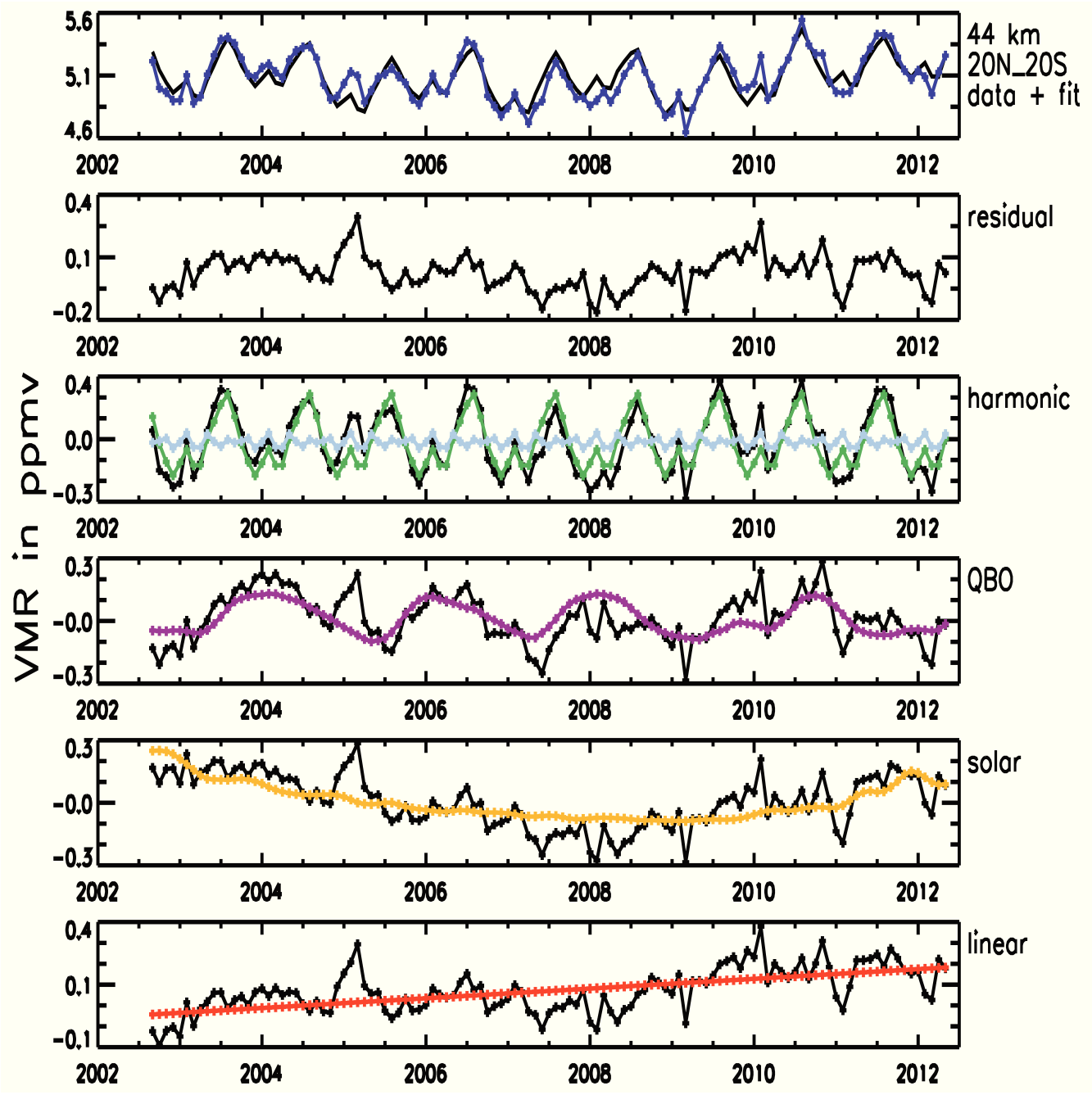

Figure 6.8: Same as Fig. 6.6 but for 44 km.

overall regression models (black). These are the fit curves. The fit residuals, i.e. the difference between time series and fit curve, can be seen in the 2nd panel. They represent the portion of the time series which is not approximated by the regression model, arising mainly from natural fluctuation. From the 3rd panel to the bottom, different components of the overall fit curve are shown such as the seasonal terms (green/light blue), QBO terms (magenta), solar cycle terms (orange), ENSO terms if included (light blue), and linear terms (red). Any component of the regression model shown is overlaid by the time series with all other terms removed.

The time series and regression models shown here are typical examples for the altitude range from 15-50 km, in the tropics and at midlatitudes (for reasons of symmetry between 60°N-50°N and 50°S-60°S, only the former band is shown here). For any of the figures, the fit residuals are within $\pm(5-10)\%$ of the corresponding time series. This is considered as criterion for presuming the fit quality to be sufficiently good throughout the altitude range of 15-50 km, at all latitudes within 60°N to 60°S.

In Figs. 6.2 and 6.4 to 6.8, the harmonic fit, i.e. the sum of the terms of 12, 6, 4, and 3 month period (green), is shown in combination with the subset including the terms of 4 and 3 month period only (light blue). As described in Section 6.2.3, the latter terms optimise the shape of the harmonic fit and, hence, improve the closure between regression models and time series. As expected, the amplitude of the harmonic fit is governed by the terms of 12 and 6 month period and not changed substantially when including the terms of 4 and 3 month period. Only at northern midlatitudes at 44 km, the terms of 4 and 3 month period contribute notably to the amplitude of the harmonic fit.

The seasonal terms dominate other periodic terms at northern midlatitudes at 20, 24, and 34 km and their sum results in an annual pattern. In the tropics at 20, 24, and 34 km, the QBO and harmonic terms are dominant. At 20 km, the QBO signatures are overlaid by an annual cycle which has its maximum in boreal summer. At 34 km, the QBO signatures are overlaid by a semi-annual oscillation pattern. At 44 km at midlatitudes, the harmonic terms dominate resulting in

an annual oscillation pattern modulated by a semi-annual oscillation pattern. These findings are consistent with Section 5.4 where obvious signatures of (semi-)annual and QBO variability were described for the time series at 20, 24, 34, and 44 km for 60°N-50°N and 20°N-20°S.

In the tropics at 20 and 24 km, the ENSO terms improve the fit quality. At 44 km, the solar cycle terms contribute notably to the fit curve both in the tropics and at midlatitudes. The solar cycle and ENSO variability in O_3 as seen by SCIAMACHY limb are discussed comprehensively in Section 9.6. At 20 and 24 km in the tropics, the linear terms indicate an increase. At 34 km, the linear terms show a decrease both at midlatitudes and in the tropics. At 44 km in the tropics, an increase is indicated by the linear terms.

6.4.2 Resulting trend profiles in the tropics and at midlatitudes

Throughout this thesis, trends are presented as vertical profiles showing their values at any altitude under study. The 1σ uncertainty (determined from the covariance matrix of regression, cf. Eq. 6.10) is used as trend uncertainty, in the following indicated by error bars. The trends and uncertainties are scaled in relative units of % per decade (relative with respect to the mean value of the underlying time series, cf. Section 6.2.2). For any trend profile, the corresponding latitude band and altitude range is specified.

Figure 6.9 shows the O_3 trend profiles derived from SCIAMACHY limb measurements for the latitude bands of 60°N-50°N (north), 20°N-20°S (tropics), and 50°S-60°S (south) in the altitude range from 15-50 km. In the tropics, positive trends are observed in the 20-30 km and 39-48 km ranges. This is contrasted by negative trends in the 30-38 km range. At northern midlatitudes, negative trends are obtained in the 25-35 km range, positive trends in the 40-45 km range, and trends from zero to positive below 25 km. At southern midlatitudes, the trends are mostly close to zero, either slightly positive or slightly negative, with exception of some negative trends above 45 km.

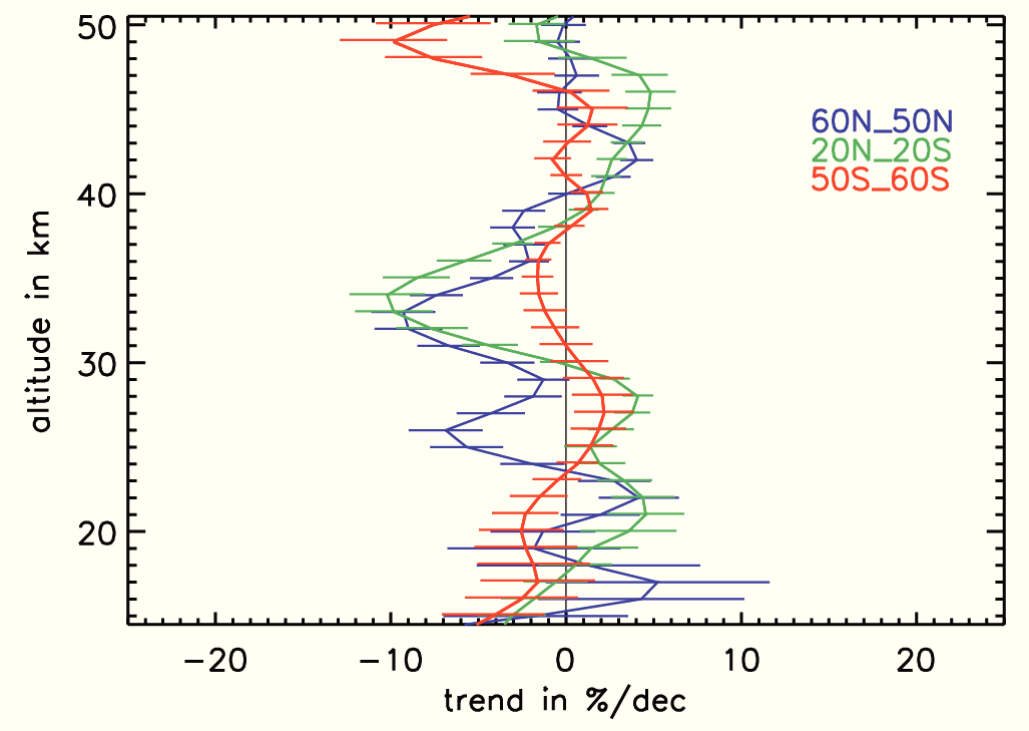

Figure 6.9: Vertical profiles of O_3 trends derived from SCIAMACHY limb measurements for the 60°N-50°N, 20°N-20°S, and 50°S-60°S latitude bands. The considered time span is 08/2002-04/2012. The trend uncertainties are 1σ, indicated by error bars.

A range of trends significant at the 2σ level (i.e. the 95 % confidence level, cf. Equation 6.11) is obtained: significant negative trends in the tropics between 30 and 38 km, positive trends close to significance in the tropics between 20 and 30 km and 39 to 48 km, significant negative trends at northern midlatitudes between 25 and 35 km, significant positive trends at northern midlatitudes between 40 and 45 km, just to name some examples.

To summarise, the trend profiles in Figure 6.9 are characterised by the following features:

- a double peak structure of positive trends in the tropics at altitudes below 30 km (with maxima between 25 and 30 km and at around 21 km at values of around $5\%dec^{-1}$),
- a single peak structure of negative trends in the tropics at altitudes between 30 and 38 km (maximum of negative trends at 33 to 34 km at values of around $-10\%dec^{-1}$),
- positive trends in the upper stratosphere of around $5\%dec^{-1}$ at maximum (in the tropics in the 38-48 km range and at northern

midlatitudes in the 40-45 km range), and

- a hemispheric asymmetry, i.e. negative trends at northern midlatitudes between 25 and 35 km of close to $-10\% dec^{-1}$ at maximum and slightly positive trends at southern midlatitudes between 25 and 30 km of around $3\% dec^{-1}$ at maximum.

In order to demonstrate that the components of the regression model introduced in Section 6.2.4 to 6.2.6, don't interfere with other components (e.g. the solar cycle terms with the linear terms as discussed in Section 6.2.5), the tropical trend profile is determined with several intermediate steps. First, no QBO, solar cycle, and ENSO terms are included into the regression model (i.e. linear and harmonic terms are used only). Second, QBO is included. Third, QBO and solar cycle are taken into account. Fourth, the full regression model with QBO, solar cycle and ENSO terms included is applied. The evolution of the tropical trend profile is shown in Figures 6.10 and 6.11. Without QBO, solar cycle, and ENSO terms, significant negative trends are evident in the middle tropical stratosphere and (mostly insignificant) positive trends in the lower and upper tropical stratosphere. The inclusion of the QBO terms clearly decreases error bars at altitudes of around 20-27 km and 30-38 km (the latter is identical to the altitude range of the maximum QBO response of tropical O_3; see Section 5.3). At altitudes between 20 and 30 km, this reduction of trend uncertainties results in significant positive trends. Extending the regression model by the solar cycle leads to notable effects above 35 km by shifting the trends into positive direction at similar or reduced uncertainties. Between 40 and 50 km, positive trends close to significance are obtained. As a result of completing the regression model by ENSO terms at altitudes below 25 km, trends are somewhat mitigated but remain positive at most altitudes. The uncertainties are reduced or similar.

As another check, the starting point of the analysed time series of O_3 has been shifted forward in 6 month steps, namely from August 2002 to February 2003, ..., February 2004 to August 2004. The shape of tropical and midlatitude trend profiles proved to hold well under these shifts. Still, it was also proven that the time series extending at least until 2011 is necessary. Otherwise, mainly the descending

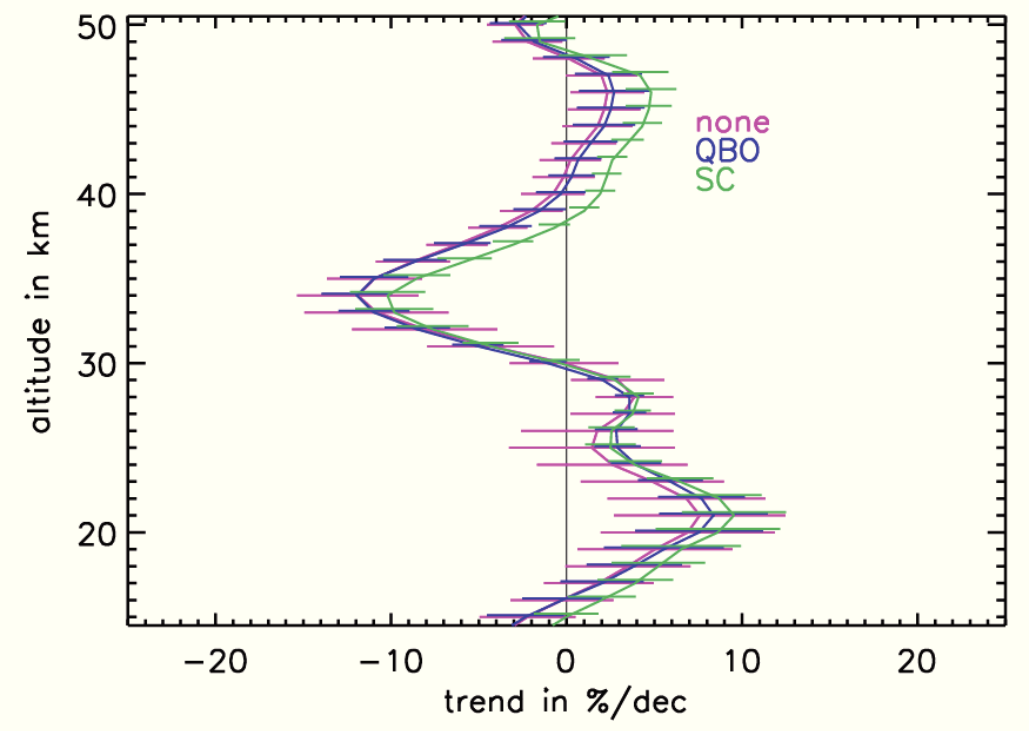

Figure 6.10: The O_3 trend profile for 20°N-20°S derived from SCIAMACHY limb measurements including sequentially the QBO and solar cycle terms into the regression model. First, neither QBO nor the solar cycle are included, i.e. linear and harmonic terms only (none; magenta coloured). Second, the QBO is added (QBO; blue coloured). Third, the QBO and SC are taken into account (SC; green coloured).

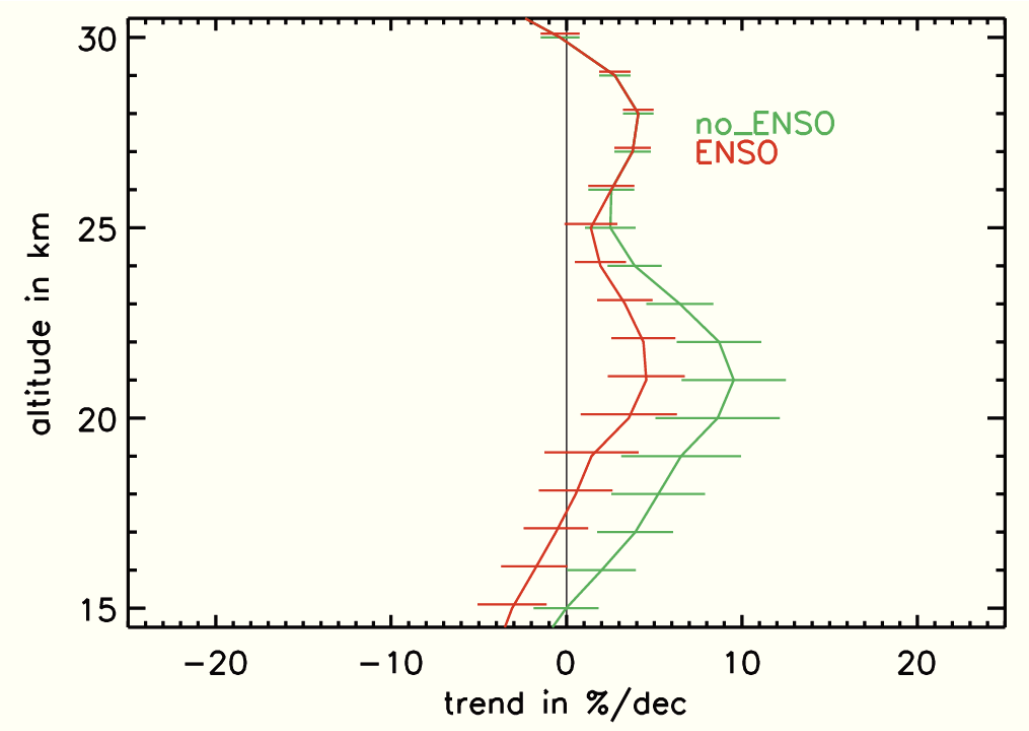

Figure 6.11: The O_3 trend profile for 20°N-20°S derived from SCIAMACHY limb measurements without ENSO terms and with ENSO terms included at altitudes up to 25 km (accordingly, no effect is seen above 25 km).

branch of the solar cycle is exhibited by the solar cycle terms used at regression. If so, they interfere with the linear terms which may end up in enhanced trend uncertainties.

7 Comparison of O_3 trends between SCIAMACHY and other instruments

7.1 Overview of the comparisons

Being other limb sounders with a high spatio-temporal overlap, EOS MLS and OSIRIS/Odin are selected for comparisons of O_3 trends to those from SCIAMACHY limb in this thesis. The results are described in Sections 7.2 to 7.4. The comparisons with OSIRIS/Odin cover the tropics and those with EOS MLS the tropics and midlatitudes. SHADOZ ozonesondes are included by a trend comparison to SCIAMACHY in the inner tropics as described in Section 7.5.

The trend comparisons between SCIAMACHY and other satellite instruments are based on zonal monthly means of gridded data. In Mieruch et al. [2012], the results of O_3 trend comparisons between different satellite instruments were not significantly changed using either pairs of data collocated between instruments or analysing directly zonal monthly means of gridded data.

7.2 Trend comparison between SCIAMACHY and OSIRIS/Odin

7.2.1 OSIRIS/Odin: Instrumentation and data preparation

OSIRIS (Optical Spectrograph and Infrared Imaging System; [Llewellyn et al., 2004; McLinden et al., 2012]) is hosted by the Odin satellite which was launched in February 2001. The OSIRIS instru-

ment went into routine operation shortly thereafter. The Odin satellite follows a sun-synchronous orbit close to the solar terminator. The equatorial crossing of Odin is at around 6:30 AM at the descending node and 6:30 PM at the ascending node. Thus, the observations of OSIRIS are always made at twilight conditions, either at dawn or at dusk. Due to the seasonal variations of day and nighttime, measurements of OSIRIS, which require sunlight, are interrupted in the winter hemisphere, i.e. in the northern hemisphere in northern winter and vice versa. Only in the tropics, data are available through all months of the year. This is why only the tropical latitude band of 20°N-20°S is covered when comparing SCIAMACHY to OSIRIS in the following. With SCIAMACHY passing the equator in the descending node at 10 AM local time, the O_3 data from OSIRIS measured at dawn, i.e. the AM data, are closer in local time. Only these data are used in the following.

OSIRIS comprises two optical modules, the optical spectrograph (OS) and the infrared imager (IRI) [McLinden et al., 2012]. The OS performs limb measurements of sunlight scattered by the atmosphere which is the basis for the retrieval of the O_3 data used in the following. The overlap of spectra of second order with those of first order is prevented by an order sorting filter suppressing the wavelength range from 480 to 530 nm. Apart from this gap, the OS is sensitive to the 280-800 nm wavelength range. As a result of a smaller instantaneous field of view and tangent height step, the OS achieves a vertical resolution between 1-2 km, which is somewhat higher than for SCIAMACHY.

Performing limb measurements with the OSIRIS optical spectrograph, the line of sight scans the limb from 7 to 70 km. O_3 is retrieved within the 10-60 km range [Degenstein et al., 2009]. In the following, OSIRIS O_3 data of the retrieval version 5.07 of the University of Saskatchewan are used. In this version, a modified filtering of outliers with respect to earlier versions is implemented. In order to prepare the OSIRIS O_3 data for instrument comparisons, their horizontal binning and vertical gridding undergo an adjustment to the SCIAMACHY limb O_3 data. First, OSIRIS O_3 is binned horizontally in 5° latitude $\times$ 15° longitude matching the horizontal binning of SCIAMACHY which

is an intermediate retrieval result as described in Section 5.1. The vertical step of the OSIRIS O_3 retrieval is 1 km like for the SCIAMACHY retrieval, but the altitudes of both retrievals are between one another. Hence, adjacent altitudes of the OSIRIS retrieval are interpolated at the altitudes of the SCIAMACHY retrieval.

Around the northern and southern solstice, the data from OSIRIS are unequally distributed within the 20°N-20°S band, i.e. mainly north of the equator in northern summer and vice versa, reflecting the seasonal variation of its spatial coverage. Throughout the selected latitude band of 20°N-20°S, the sampling of SCIAMACHY and OSIRIS is matched by excluding the data of both in any horizontal bin if one instrument has no data for a certain month. Subsequently, zonal monthly means are calculated. The resulting time series span the period from 08/2002-04/2012. Trend analysis is performed by multivariate linear regression as described in Section 6.3. Vertical profiles of O_3 trends in the 15-50 km altitude range, at 1 km vertical steps, obtained from SCIAMACHY and OSIRIS are compared.

7.2.2 Comparison results

Figure 7.1 shows the vertical profiles of tropical O_3 trends from SCIAMACHY and OSIRIS. For SCIAMACHY, the characteristics of the tropical O_3 trends, identified before for 20°N-20°S in Section 6.4.2, hold for altitudes above 20 km. The trend profile from SCIAMACHY shows a double peak structure of positive trends between 20 and 30 km and a single peak structure of negative trends between 30 and 38 km. In the upper stratosphere, positive trends are observed between 40 and 48 km. Below 20 km, the trends from SCIAMACHY, which are in good agreement to OSIRIS, become clearly negative. This is different from Section 6.4.2, where the tropical trends from SCIAMACHY were positive above 17 km, which arises from the sampling adjusted between both instruments. The matched sampling is largely determined by the sampling of OSIRIS which is inhomogeneous during northern and southern hemisphere winter as described before. With the zonal symmetry of tropical O_3 not holding throughout the 15-20 km range [e.g. Randel and Thompson, 2011] some gradient in longitude might

be reflected.

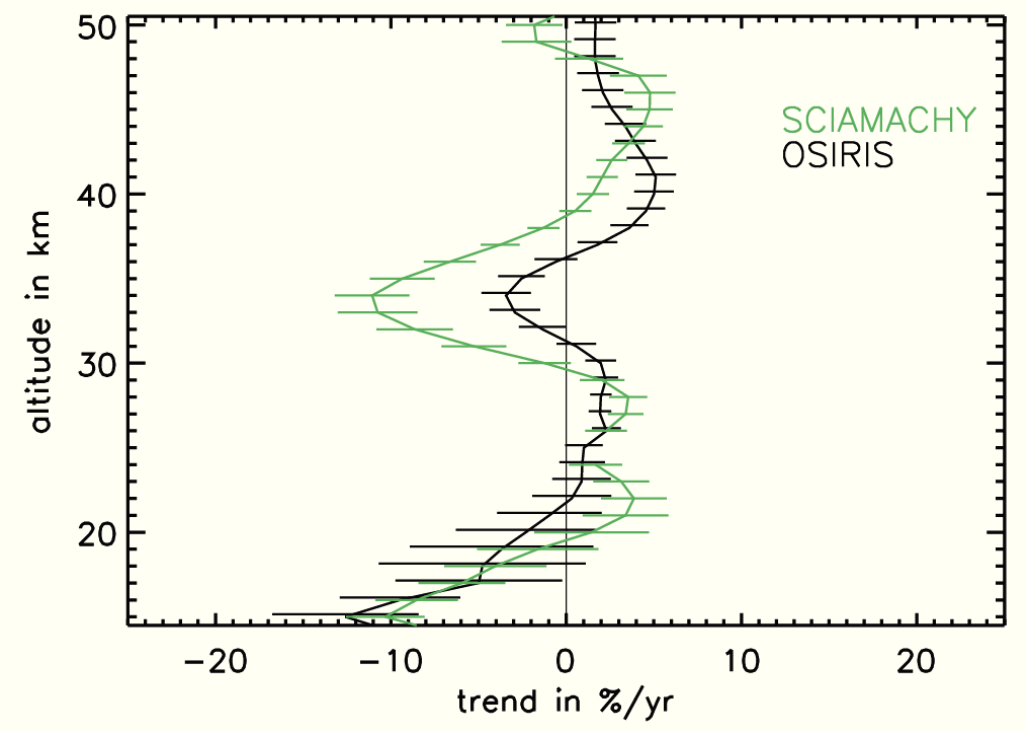

Figure 7.1: Comparison of vertical profiles of O_3 trends between SCIAMACHY and OSIRIS for the 20°N-20°S band. The covered time span is 08/2002-04/2012. Error bars: 1σ.

The O_3 trend profile for 20°N-20°S from OSIRIS shows overall good agreement with SCIAMACHY results. Below 30 km, the trends from OSIRIS and SCIAMACHY agree within their uncertainties. Between 25 and 30 km, positive trends from OSIRIS are close to significance. Between 31 and 37 km, OSIRIS shows a single peak structure of negative trends maximising at 34 km at values of around $4\% dec^{-1}$. Albeit SCIAMACHY maximises at negative O_3 trends of slightly more than $-10\% dec^{-1}$, the single peak structures of negative trends seen by both instruments agree qualitatively with one another. OSIRIS is at significance at least around the maximum of negative trends. In the upper stratosphere, OSIRIS and SCIAMACHY show positive trends in the 40-48 km range maximising at values around $5\% dec^{-1}$. These maximum is seen by SCIAMACHY around 46 km and by OSIRIS around 41 km.

7.3 Trend comparison between SCIAMACHY and EOS MLS

7.3.1 EOS MLS: Instrumentation and data preparation

EOS MLS (Earth Observing System Microwave Limb Sounder) senses thermal radiation in the microwave spectral range from the Earth's atmosphere limb both on the day and night side of its orbit. The MLS instrument uses microwave radiometers in spectral regions centred around 118 GHz, 190 GHz, 240 GHz, 640 GHz, and 2.5 THz. The standard O_3 data product from MLS is retrieved from 240 GHz measurements [Froidevaux et al., 2008].

Aboard the EOS/Aura satellite, MLS was launched in July 2004. Its scientific operation began in mid of August 2004. The EOS/Aura satellite flies in a sun-synchronous near polar orbit with its ascending node at 1:45 PM. Being made in local time closer to SCIAMACHY, daytime O_3 data from MLS are used to make comparisons. The considered latitude bands are 60°N-50°N, 20°N-20°S, and 50°S-60°S, analogous to Section 5.1. The time span covered by the comparison is 08/2004-04/2012.

The MLS O_3 dataset used in the comparisons is of the retrieval version 2.2 [Froidevaux et al., 2008] with pressure as the vertical coordinate. Pressures between 242 and 0.02 hPa are recommended for scientific use. These pressures include well the 15-50 km altitude range which is under analysis here. After converting from pressures to geometric heights, the MLS O_3 profiles are interpolated at the altitudes from 15 to 50 km in steps of 1 km, which are altitudes of the SCIAMACHY O_3 retrieval. Subsequently, zonal monthly means are calculated for the selected latitude bands and altitudes. The resulting time series undergo trend analysis.

7.3.2 Comparison results

Figures 7.2 to 7.4 show the O_3 trend profiles from SCIAMACHY and MLS for the latitude bands of 20°N-20°S (tropics), 60°N-50°N (north-

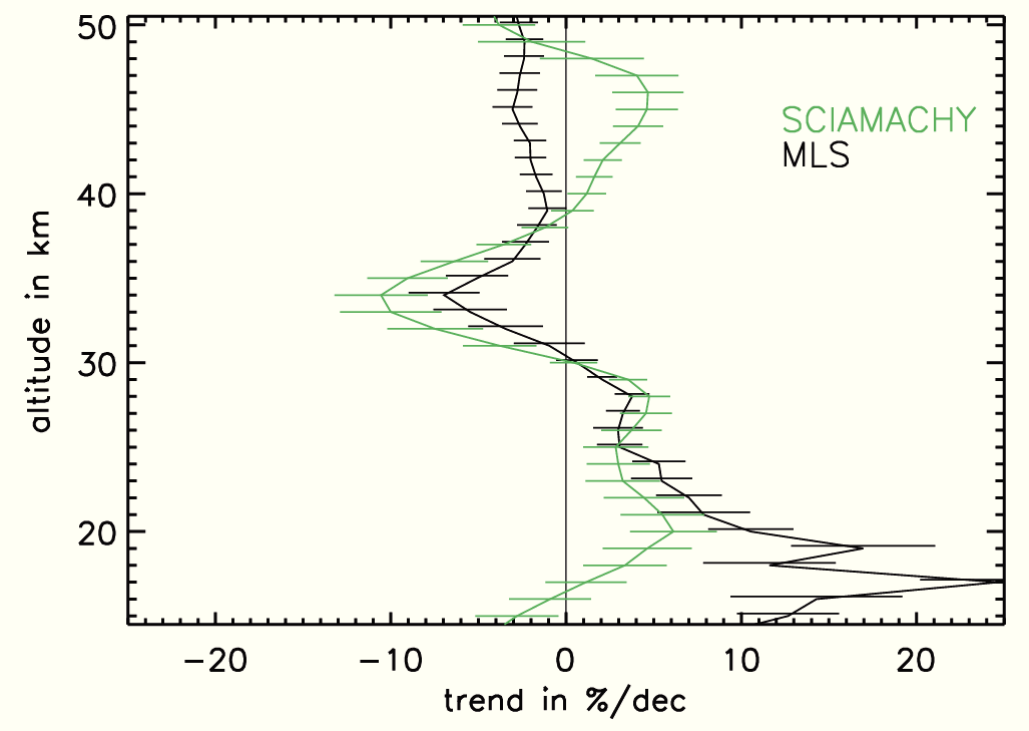

Figure 7.2: Comparison of vertical profiles of O_3 trends between SCIAMACHY and MLS for the 20°N-20°S band. The covered time span is 08/2004-04/2012. Error bars: 1σ.

ern midlatitudes), and 50°S-60°S (southern midlatitudes) for the time span 08/2004-04/2012. Although the first two years of SCIAMACHY are excluded with the trend comparison starting in 08/2004, the overall shape of the vertical profiles of O_3 trends is similar to that in Section 6.4.2.

In the tropics, MLS confirms the single peak structure of negative O_3 trends seen by SCIAMACHY between 30 and 38 km. Around the maximum of negative trends at 34 km, SCIAMACHY is at around $-10\%dec^{-1}$ while MLS is at around $-7\%dec^{-1}$. Between 20 and 30 km, MLS sees significant positive O_3 trends which are in good agreement with SCIAMACHY results. Below, the agreement of MLS and SCIAMACHY decays. While SCIAMACHY sees a trend maximum at values of around $5\%dec^{-1}$ at 20 km decreasing to zero at 17 km, the trends from MLS climb further. In the 15-20 km range, MLS shows a maximum of positive trends of roughly $10\%dec^{-1}$. In the upper stratosphere, a discrepancy between SCIAMACHY and MLS is observed between 40 and 48 km. While SCIAMACHY sees positive O_3 trends up to around $5\%dec^{-1}$, MLS shows zero to negative O_3 trends. From 48 to 50 km, zero to negative trends are shown by SCIAMACHY as well and both

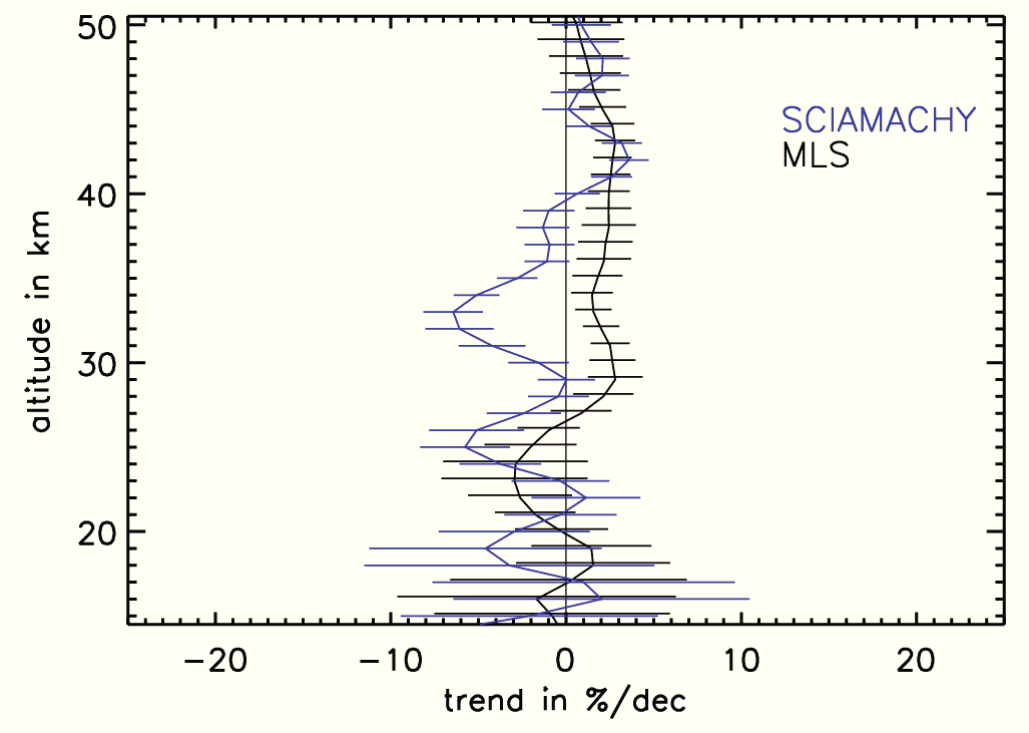

Figure 7.3: Same as Figure 7.2, but for 60°N-50°N.

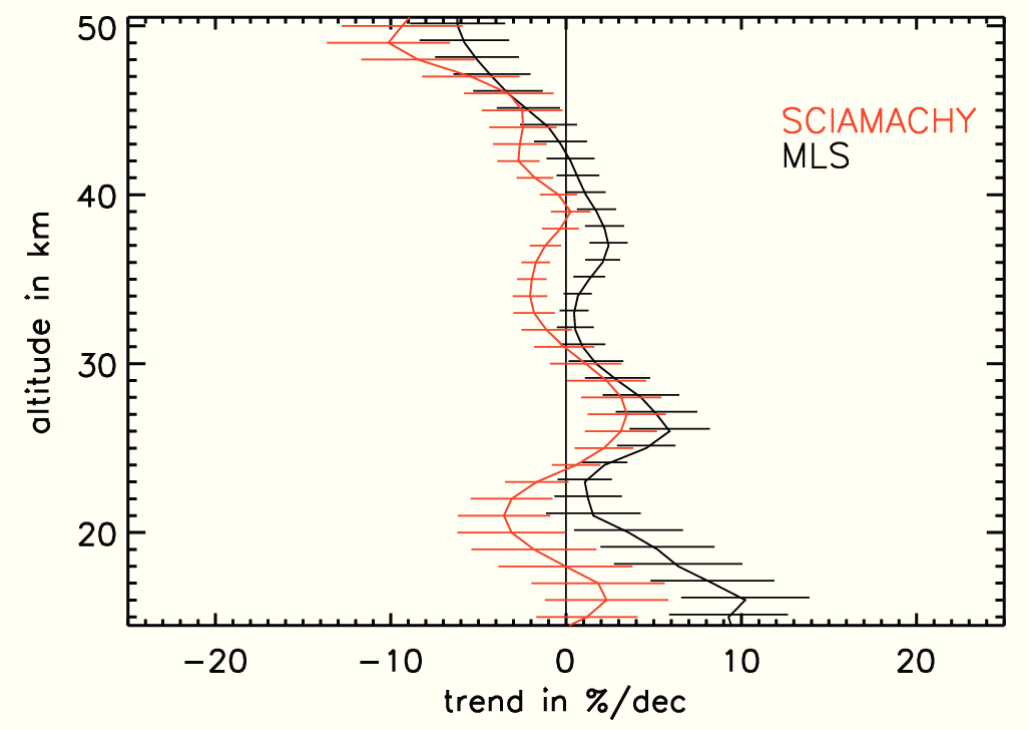

Figure 7.4: Same as Figure 7.2, but for 50°S-60°S.

instruments are in agreement.

At northern midlatitudes, an inconsistency is observed between 30 and 35 km with SCIAMACHY showing significant negative O_3 trends and MLS positive O_3 trends which are close to significance around 30 km. Apart from this, the O_3 trend profiles from SCIAMACHY and MLS are in reasonable agreement in the 25-50 km range. Below 25 km, both instruments agree within their uncertainties, but are both mostly not different from zero within their uncertainties. In the upper stratosphere, SCIAMACHY and MLS agree in the 40-50 km range within their uncertainties. Positive O_3 trends up to around $5\% dec^{-1}$ seen by SCIAMACHY in the 40-45 km range are consistent with the trends from MLS.

At southern midlatitudes, the O_3 trend profiles from SCIAMACHY and MLS are in agreement. They follow each other closely at similar uncertainties. Between 25 and 30 km, both instruments see consistently positive O_3 trends. In the upper stratosphere above 40 km, SCIAMACHY and MLS show increasingly negative O_3 trends.

7.4 Trend comparison between 3 instruments: SCIAMACHY, EOS MLS, and OSIRIS/Odin

In previous sections, O_3 trends from SCIAMACHY were compared separately to OSIRIS/Odin and EOS MLS. Here, all three instruments are compared. The latitude band of 20°N-20°S (conform with Section 7.2) and the time span from 08/2004-04/2012 (conform with Section 7.3) are selected. As before, the O_3 data from OSIRIS measured at AM local times and the O_3 data from MLS measured at daytime are used. The data are binned and subsequently averaged zonally with their sampling matched according to the principle described Section 7.2.1.

The vertical profiles of O_3 trends from SCIAMACHY, MLS, and OSIRIS are shown in Figure 7.5. Between 17 and 30 km, all three instruments see positive O_3 trends. Good agreement between all instruments is obtained between 25 and 30 km. Below, SCIAMACHY shows a maximum of positive trends around 21 km at values close to

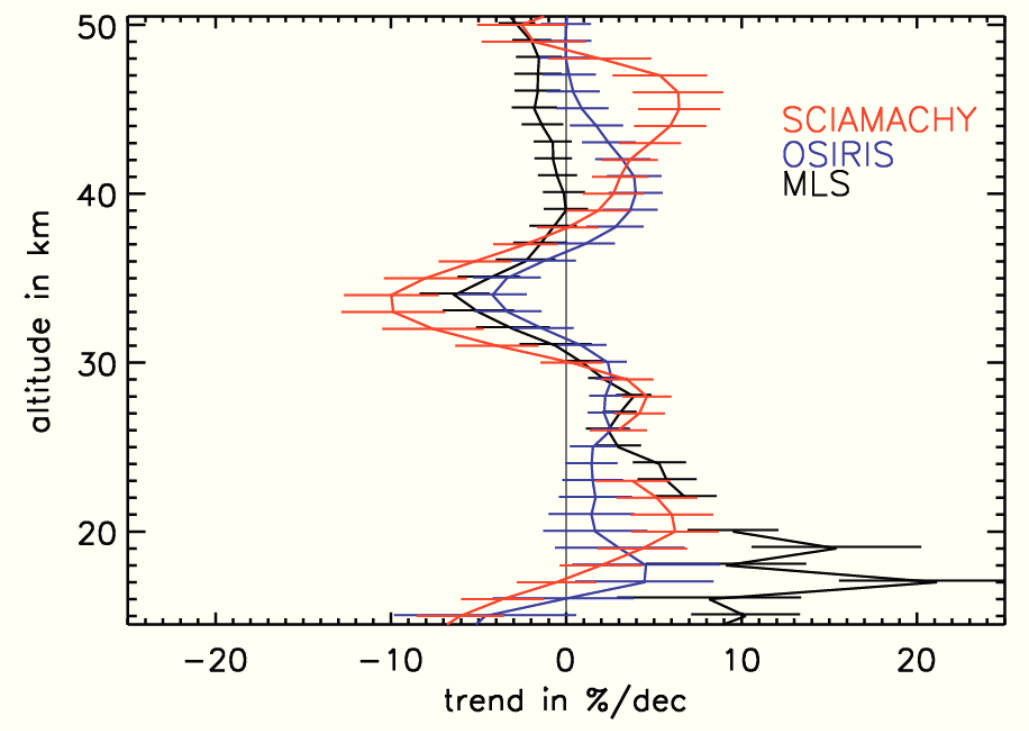

Figure 7.5: Comparison of vertical profiles of O_3 trends between SCIAMACHY, MLS, and OSIRIS for the 20°N-20°S band. The covered time span is 08/2004-04/2012. Error bars: 1σ. Note a few gaps in the vertical trend profiles below 25 km. These arise from omitting the regression results because of ENSO signatures being not captured precisely by regression (cf. Section 6.2.6).

$7\%dec^{-1}$ decreasing to zero at 17 km. Similarly, OSIRIS sees a trend maximum at around 17-18 km at values close to $5\%dec^{-1}$ decreasing to zero below. Differently, MLS shows a maximum of trends somewhere in the 15-20 km range at values of roughly $10\%dec^{-1}$.

Within the 30-38 km range, all three instruments see negative O_3 trends maximising at 33-34 km: at maximum, SCIAMACHY is around $-10\%dec^{-1}$, MLS around $-7\%dec^{-1}$, and OSIRIS around $-4\%dec^{-1}$. In the 38-48 km range, SCIAMACHY and OSIRIS show positive trends similar to Section 7.2. The trend from SCIAMACHY maximises around 46 km at values of around $6\%dec^{-1}$ and that from OSIRIS at around 40 km at values of around $4\%dec^{-1}$. Similar to Section 7.3, MLS sees zero to negative trends between 40 and 50 km. Zero to negative trends are shown by all 3 instruments from 48 to 50 km.

7.5 Trend comparison between SCIAMACHY and ozonesondes

7.5.1 Ozonesondes: instrumentation and data preparation

With ozonesondes, balloon-borne in-situ measurements are included into the comparisons of O_3 trends. Only the inner tropics are covered by these comparisons. A systematic intensification of measurements of tropical ozonesonde stations since 1998 has been achieved by the SHADOZ (Southern Hemisphere Additional Ozonesondes) project [Thompson et al., 2003]. The following SHADOZ ozonesonde stations in the inner tropics are selected:

- Ascension (8.0S, 14.4W),
- Kuala Lumpur (2.7N, 101.7E),
- Nairobi (1.3S, 36.8E),
- Natal (5.4S, 35.4W),
- and Paramaribo (5.8N, 55.2W).

The sites of these stations are more or less equidistant in latitude (their longitudes are considered to be of secondary importance since tropical stratospheric O_3 is known to be generally highly zonally symmetric). Furthermore, these stations have been operational for the entire (or most of the) lifetime of SCIAMACHY. The time span covered by the comparison is 08/2002-04/2012.

The SHADOZ O_3 data considered here were measured by the combination of an ozonesonde and a standard radiosonde flown by a weather balloon [Thompson et al., 2004]. The ozonesonde measurements employ electrochemical concentration cells (ECC). At balloon ascent, air from outside is pumped through the cells producing an electric current proportional to the partial pressure of O_3. The accompanying radiosonde provides measurements of the air temperature and pressure.

Ozonesonde measurements are limited by altitudes of 30 to 35 km for factors like balloon burst and evaporation/freezing of the chemical

sensing solution used in the cells. Thus, O_3 trends from sondes are shown up to the altitude of 30 km in the following. The comparison of O_3 trends between SCIAMACHY and the ozonesondes is performed at altitudes from 15 to 30 km at vertical steps of 1 km. Ozonesondes have a vertical resolution on the order of 100 m which is clearly finer than that of the SCIAMACHY limb sounder. As described in Section 4.1, the resolution of SCIAMACHY is between 3-4 km. The vertical resolutions are accounted for: at the altitudes from 15-30 km, the vertical profiles of O_3 from the sondes are smoothed over intervals of $\pm$2 km.

Several sonde launches per month and per ozonesonde station are typical. First, monthly mean vertical profiles of O_3 are calculated for any station selected here. This leads to time series of monthly mean O_3 from individual stations at the altitudes of 15-30 km in vertical steps of 1 km. Secondly, these time series are averaged over all stations selected. Accounting for possible offsets between individual stations, the mean values of their monthly O_3 time series are adjusted before averaging. This is done by forcing the mean values of all stations to be equal to one of the stations, in this case Paramaribo (arbitrarily selected).

O_3 data from SCIAMACHY are selected at latitudes and longitudes of the binning described in Section 5.1 which match the sites of the ozonesonde stations. The sampling is adjusted further by excluding the data of any station and SCIAMACHY if only one of both has no data for a certain month and altitude. The averaging of the O_3 data from SCIAMACHY follows the same principle as for the ozonesonde stations.

7.5.2 Comparison results

Figures 7.6 shows the O_3 trend profiles from SCIAMACHY and the ozonesondes. Though derived from latitudes and longitudes matching the sites of the ozonesonde stations, the trend profile from SCIAMACHY resembles well the pattern of O_3 trends derived from zonally averaged data at latitudes from around 5°N to 5°S, shown in Figure 9.1.

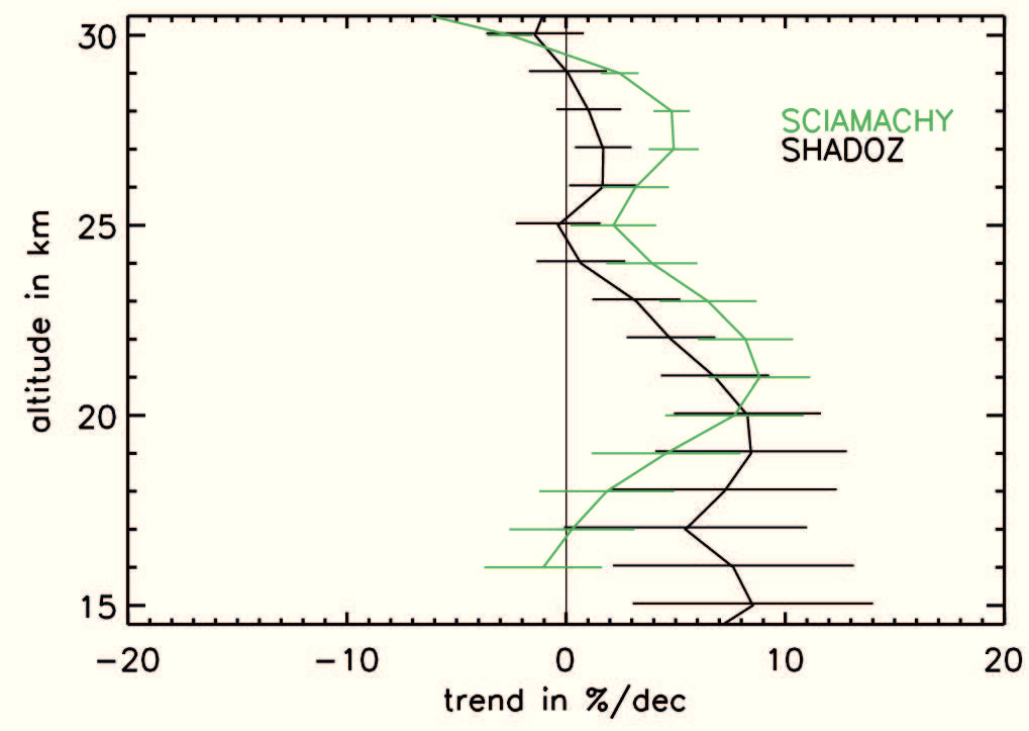

Figure 7.6: Comparison of vertical profiles of O_3 trends between SCIAMACHY and tropical SHADOZ ozonesondes. The ozonesonde stations of Ascension (8.0°S, 14.4°W), Kuala Lumpur (2.7°N, 101.7°E), Nairobi (1.3°S, 36.8°E), Natal (5.4°S, 35.4°W), and Paramaribo (5.8°N, 55.2°W) are selected. The covered time span is 08/2002-04/2012. Error bars: 1σ.

The O_3 trend profiles from SCIAMACHY and the SHADOZ ozonesondes are in reasonable agreement. Below 25 km, positive O_3 trends are seen by the sondes which mostly agree with SCIAMACHY within their uncertainties. Above 25 km, the trends from the sondes are zero to positive at values smaller than those from SCIAMACHY. The positive trends from SCIAMACHY maximise at around 21 km and decrease to values close to zero at around 17 km. Differently, trend values close to $10\%dec^{-1}$ hold down to 15 km for the sondes. Performing trend comparisons between SCIAMACHY and other satellite instruments, MLS similarly showed positive trends between 15 and 20 km at values of roughly $10\%dec^{-1}$ with the tropics represented by the 20°N-20°S latitude band in Section 7.3 and 7.4. This was not seen by SCIAMACHY.

8 Discussion of error sources

8.1 Mispointing of the line of sight

The line of sight pointing accuracy is a source of error common to all limb viewing satellite instruments [v. Savigny et al., 2005]. In limb geometry, the tangent point and, accordingly, the targeted volume of air is typically thousands of kilometres away from the spacecraft (for SCIAMACHY limb measurements, details can be found in Section 4.1). Thus, misalignments of the line of sight of a few hundreds of one degree are sufficient to give rise to vertical offsets in tangent height of a few hundred meters or more [v. Savigny et al., 2005]. In the following, this is investigated as a potential source of error for the O_3 trends from SCIAMACHY limb measurements inferred in this thesis.

For the early years of SCIMACHY, v. Savigny et al. [2005] inferred errors up to 2 km. As a result of improvements of the on-board software of ENVISAT, errors in the tangent height information could be reduced to values of not more than few hundred meters. The improvements in tangent height information extend over the time before the implementation of the software updates as well [Bramstedt et al., 2012].

The remaining tangent height errors have been analysed precisely by Bramstedt et al. [2012] by a method using solar occultation measurements of SCIAMACHY. The full period of SCIAMACHY is covered by their study. The resulting monthly mean tangent height offset is of not more than few hundred meters in total. For the largest part, it has constant and seasonally varying components. During the first four years of the SCIAMACHY mission, a continuous increase of tangent height offset by 50 m was identified. We assume that SCIAMACHY limb measurements are subject to a similar pattern of tangent height

error: related monthly mean time series of data may reflect constant offsets, seasonally varying, and continuously changing patterns as artefacts. Applying our regression model (cf. Equation 6.1), its constant and seasonal terms are expected to absorb the constant offsets and seasonal features. The continuous change in the tangent height error still requires investigation. Although the assumed pattern of tangent height error is adapted from solar occultation measurements, it is considered to be sufficient to indicate whether line of sight mispointing may have a significant impact on trends derived from limb measurements.

As a correction calculation, a pattern of tangent height offset which starts at 50 m and decreases linearly towards zero throughout the first four years of the SCIAMACHY mission is generated artificially. This aims at neutralising the evidenced 50 m increase of tangent height error described before.

The correction utilises reference vertical profiles of O_3, one for each season. These reference profiles are considered to be representative of the total amount of vertical profiles of O_3 resulting from SCIAMACHY limb measurements. The reference profiles were retrieved assuming no mispointing and a shift in the pointing of $\pm$250 m which is an approximate upper limit for typical tangent height offsets reported by Bramstedt et al. [2012].

The correction is based on linear interpolation between the non-shifted and shifted vertical reference profiles. A multiplicative correction is applied to the SCIAMACHY limb O_3 data which are available as gridded monthly mean values.

In Figure 8.1, the SCIAMACHY O_3 trends resulting for the tropical latitude band of 20°N-20°S from corrected and non-corrected data are compared (the non-corrected trends are identical to the tropical trends shown in Figure 6.9). The largest shift of trends occurs above 40 km, at values of maximally $1\%dec^{-1}$. This does, however, not mean substantial changes to the overall shape of the trend profile. With and without the correction, O_3 trends have positive values above 40 km and are close to significance (at the 2σ level; cf. Equation 6.11) around 45 km. A similar robustness of trends was obtained when

performing the same correction for the latitude bands of 60°N-50°N and 50°S-60°S.

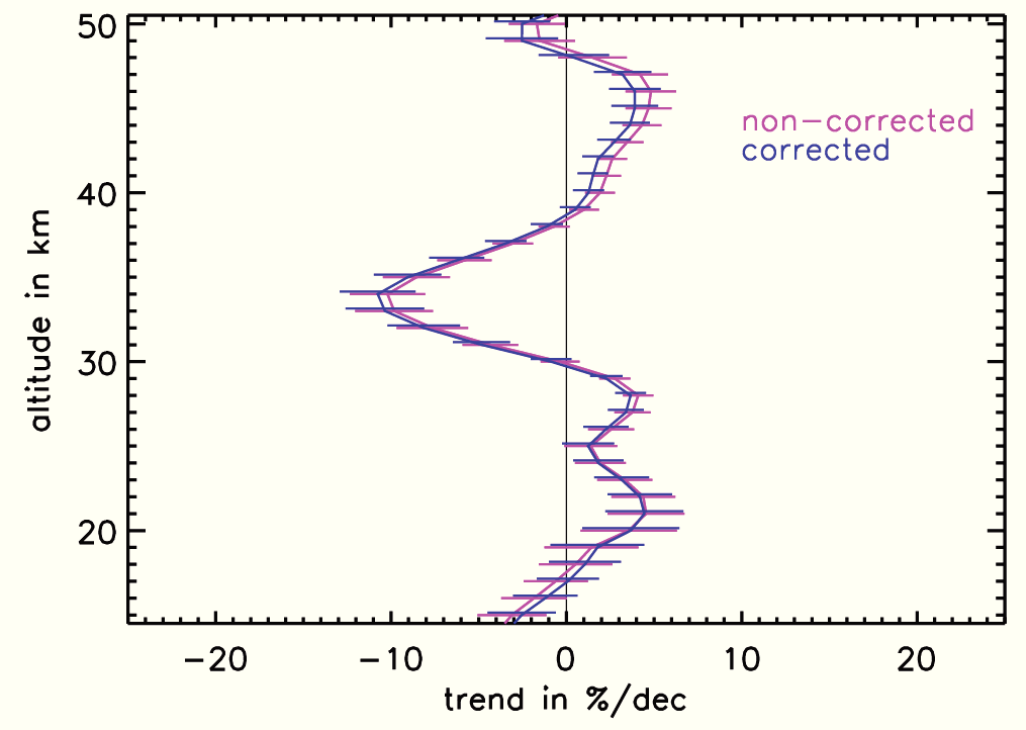

Figure 8.1: Vertical profiles of SCIAMACHY limb O_3 trends for the tropical latitude band of 20°N-20°S from non-corrected data and data corrected for tangent height inaccuracy.

The performed investigation shows that potential inaccuracies of O_3 trends due to tangent height drifts are within $\pm 1\% dec^{-1}$. Hence, tangent height drifts cannot explain discrepancies between SCIAMACHY limb and other instruments identified in Chapter 7.

8.2 Pressure and temperature

8.2.1 Stability of O_3 trends with respect to data unit conversion

As demonstrated by McLinden and Fioletov [2011], O_3 trends from satellite instruments may differ depending on the data units used, volume mixing ratio or number density, in the case of accompanying temperature and/or pressure trends. The latter gives rise to trends in the neutral density of air which act on O_3 trends at unit conversion. Accordingly, it has to be checked whether O_3 trends inferred from

satellite instruments in this thesis are sensitive to using data units of volume mixing ratio or number density.

As a check, the comparison of O_3 trends between SCIAMACHY, OSIRIS/Odin, and EOS MLS in Section 7.4 is redone using units of number density. The corresponding time series are generally similar to those in units of volume mixing ratio used in Section 7.4. The 3-instrument-comparisons in units of volume mixing ratio and number density are presented in Figure 8.2 and 8.3. As expected from the use of the same pressure/temperature database, differences are neither resolved nor produced between SCIAMACHY and OSIRIS by changing units. The trends from SCIAMACHY and OSIRIS are practically unchanged at all altitudes below 41-42 km. Above, the trends from OSIRIS/Odin are shifted into positive direction so that values of around $4\% dec^{-1}$ are obtained throughout the 40-50 km range and those from SCIAMACHY move into positive direction as well. At 45-46 km, the maximum of positive upper stratospheric O_3 trends is seen by SCIAMACHY at values of around $6\% dec^{-1}$ / $9\% dec^{-1}$ for units of volume mixing ratio / number density. Contrastingly, the trends from MLS are shifted somewhat into negative direction for practically all altitudes when changing to number density. As a result, the trends from MLS are still between SCIAMACHY and OSIRIS in the tropical 30-35 km range, but agree somewhat better with SCIAMACHY. Above 38 km, the difference between SCIAMACHY and MLS is enhanced.

By changing the data units from volume mixing ratio to number density, vertical profiles of O_3 trends from different instruments show a non-consistent behaviour (positive shifts are contrasted by negative shifts). By implication, a data unit sensitivity of the O_3 trends does not offer a plausible explanation. The differences rather arise from factors specific to the instruments. Different from SCIAMACHY and OSIRIS, MLS has its own pressure and temperature retrieval. At data unit conversion, ECMWF data serve as pressure/temperature database for SCIAMACHY and OSIRIS while self-retrieved pressure and temperature data are used for MLS. Indeed, inconsistencies between these pressure/temperature databases were suggested by Adams et al. [2014]. Determining drifts in the record of O_3 data between OSIRIS and other instruments, the use of different pressure and temperature

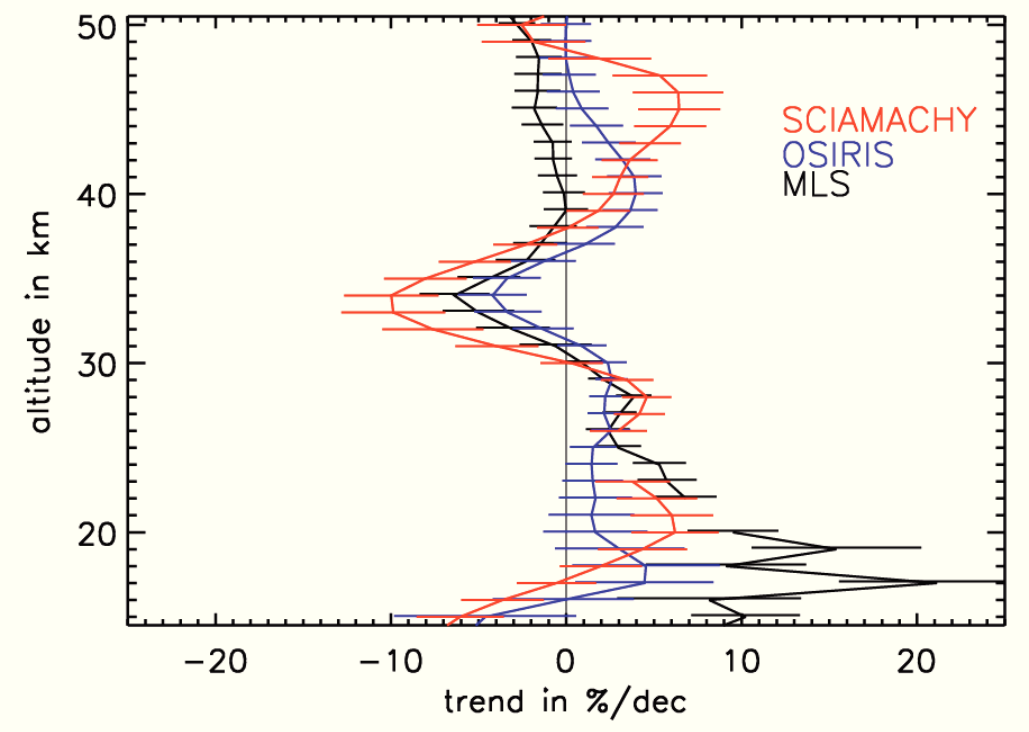

Figure 8.2: Comparison of vertical profiles of O_3 trends between SCIAMACHY, MLS, and OSIRIS for the 20°N-20°S band using units of volume mixing ratio. The covered time span is 08/2004-04/2012. Error bars: 1σ. This Figure is identical to Figure 7.5 (repeated here for demonstration purposes).

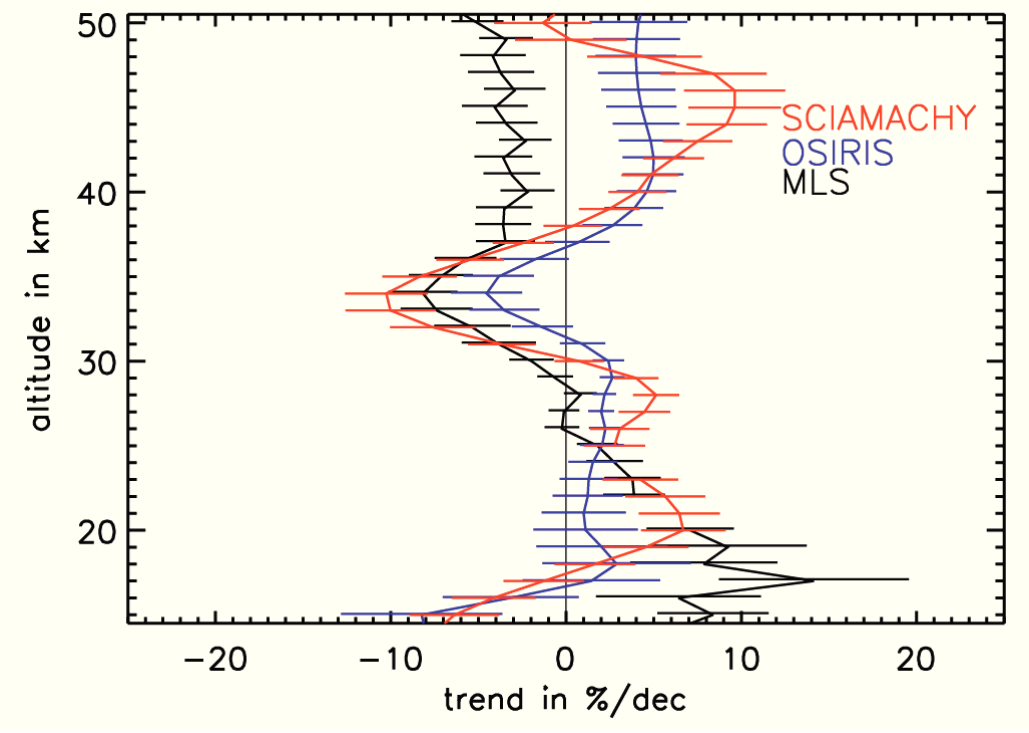

Figure 8.3: Same as Figure 8.2, but for trends in units of number density.

databases led to differences in the results (particularly above 35 km, also notable below).

8.2.2 Auxiliary data on pressure and temperature as a minor source of error

As the native units of O_3 retrieval vary from instrument to instrument, data unit conversions are made to harmonise their datasets. The native unit of O_3 retrieval is number density on an altitude grid for SCIAMACHY and OSIRIS and volume mixing ratio on a pressure grid for EOS MLS [Froidevaux et al., 2008]. The use of volume mixing ratio units on an altitude grid throughout Chapter 7 implies data conversions for all 3 instruments.

In Section 8.2.1, unit conversions to native units of the instruments were already made like the conversion to number density for SCIAMACHY and OSIRIS (not shown here is the conversion to volume mixing ratio on a pressure grid for MLS). However, the resulting changes of O_3 trends cannot resolve the discrepancies found in Chapter 7 at trend comparisons between the instruments.

Besides, the pressure and temperature are forward model parameters in the O_3 retrieval, described for SCIAMACHY in Section 4.3. Hence, inconsistencies between pressure/temperature databases might have effects on the satellite retrieved data even without unit conversion. This cannot explain the discrepancies between the three instruments, summarised in Section 7.4, either as both SCIAMACHY and OSIRIS use the same operational ECMWF data.

8.3 Sensitivity of the O_3 retrieval

The overall altitude range covered by the SCIAMACHY limb O_3 retrieval, which extends from 10 to more than 60 km, includes well the 15-50 km range under study here. For the latter, reduced retrieval sensitivity only needs discussion in the 30-40 km sub-range as a result of the transition between retrieval information coming from visible

and UV wavelengths. This transition has already been described in Section 4.3.

Previously, Mieruch et al. [2012] found number densities of SCIAMACHY limb O_3 having a positive offset with respect to comparison instruments in the tropics around 30 and 40 km. The combined use of different wavelengths in the SCIAMACHY limb O_3 retrieval was considered to be one possible source of error. Comparing time series of the O_3 volume mixing ratio between SCIAMACHY and other instruments, the study of Tegtmeier et al. [2013] found that SCIAMACHY lies 10-20% above the multi-instrument average in the tropics around 10 hPa, which roughly corresponds with an altitude of 30 km. In addition, the SCIAMACHY was found to overestimate the amplitude of QBO signatures of O_3 in the middle tropical stratosphere. This is also consistent with the findings of this thesis in Section 9.5. However, it is not necessarily a source of error for the resulting O_3 trends. As described in Section 6.4.2, the inclusion of QBO terms into our regression model reduced trend uncertainties considerably, but left the trends themselves practically unchanged.

Taken as a whole, the combined use of different wavelengths at the O_3 retrieval is possibly one key for resolving discrepancies at trend comparisons between SCIAMACHY and other instruments. The following inconsistencies are in the altitude range where the transition between UV and visible wavelengths is relevant as a source of error:

- SCIAMACHY sees negative O_3 trends in the 30-35 km range at northern midlatitudes (60°N-50°N) while EOS MLS has moderately positive trends, described in Section 7.3 and
- SCIAMACHY, EOS MLS, and OSIRIS/Odin show in qualitative agreement negative trends in the 30-35 km range in the tropics (20°N-20°S), but trend values differ from one another by a factor up to around 2, described in Section 7.4.

In the future, some modified retrieval version of SCIAMACHY limb O_3 which utilises more wavelengths might be realised. With respect to O_3 trends, it may narrow down the potential of reduced retrieval sensitivity being a source of error.

9 Ozone trends and variabilities from SCIAMACHY in a global view

9.1 Overview

In this Chapter, a comprehensive analysis of time series of zonal monthly mean O_3 from 60°N to 60°S, at steps of 5° latitude, is made. The covered altitude range is 15-50 km. As a function of latitude and altitude, trends, the autocorrelation, and the strength of periodic variabilities of O_3 are presented.

Here, harmonic fit terms are used only. The cumulative eddy heat flux is not used with being of relevance only at the northernmost edge of the latitude range and the lowermost edge of the altitude range considered.

Few results are omitted with being not able to determine the time lag of the ENSO terms precisely (the latter serves as an omission criterion of the results as described in Section 6.2.6). Due to this, few blank spaces in the lower tropical stratosphere are evident in the Figures 9.1 to 9.10.

9.2 Trends and autocorrelation

In Figure 9.1, the resulting O_3 trends are shown as latitude altitude plot. In the proximity of the equator, positive trends maximising near $10\% dec^{-1}$ at altitudes of 20-23 km and 27-28 km are obtained. Another maximum of positive trends is observed at latitudes between 20 and 30°N and altitudes between 20 and 25 km. Around these maxima, the trends are significant at the 2σ level. Limited by altitudes from

30 to 38 km and by latitudes from 15°N and 15°S, significant negative trends are seen. Centred around the equator and altitudes of 33-34 km, an "island" of negative trends touching $-20\%dec^{-1}$ at maximum appears. These maxima of positive and negative trends around the equator are consistent with the double peak structure of positive trends in the lower tropical stratosphere and the single peak structure of negative trends in the middle tropical stratosphere identified for the wider tropical latitude band of 20°N-20°S in Section 6.4.2.

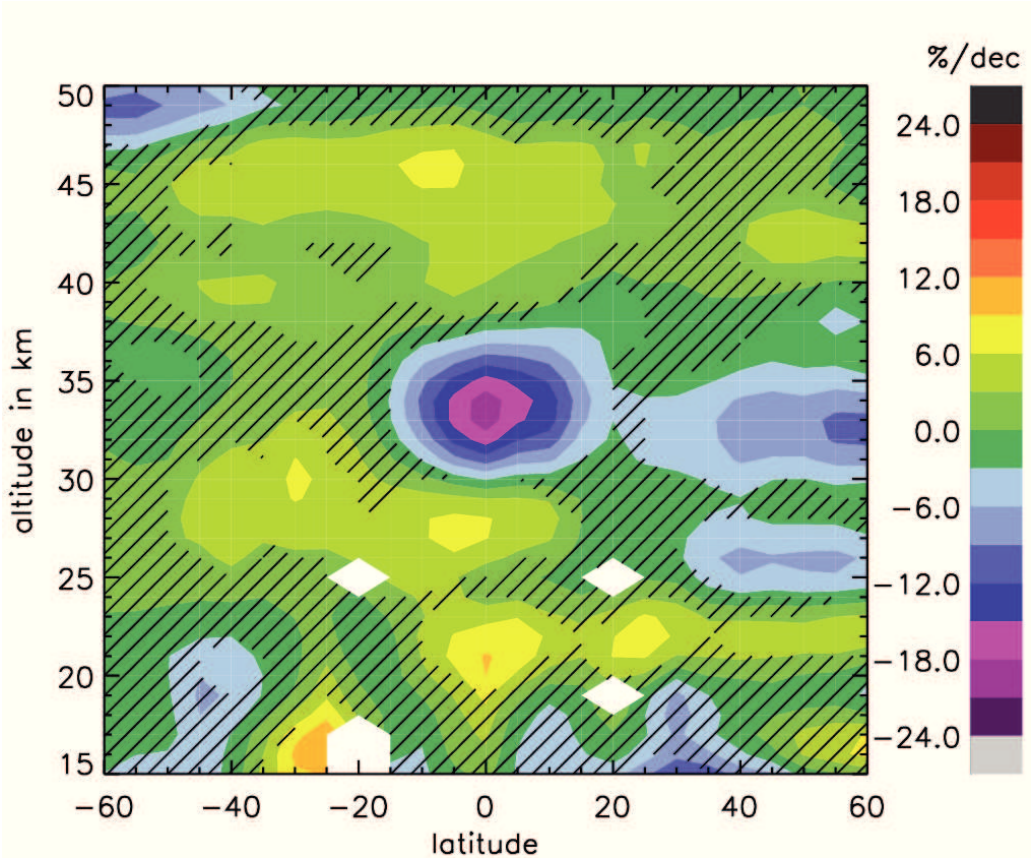

Figure 9.1: O_3 trends from SCIAMACHY from 60°N to 60°S and 15 to 50 km. Legend on the right (in units of $\%dec^{-1}$). Non-hatched areas are significances at the 2σ level.

In the 25-35 km range, positive O_3 trends at values of around $5-10\%dec^{-1}$ at maximum are obtained south of the tropics and negative O_3 trends at values of around $-(5-10)\%dec^{-1}$ at maximum at northern midlatitudes. This pattern of trends is a more complete representation of the hemispheric asymmetry of extratropical O_3 trends evidenced in Section 6.4.2 (where the trends are clearly negative for 60°N-50°N in the 25-35 km range and small positive for 50°S-60°S in the 25-30 km range). Positive trends of about $5\%dec^{-1}$ extend through large parts of the latitude range from 60°N to 60°S at altitudes be-

tween around 38 and 48 km.

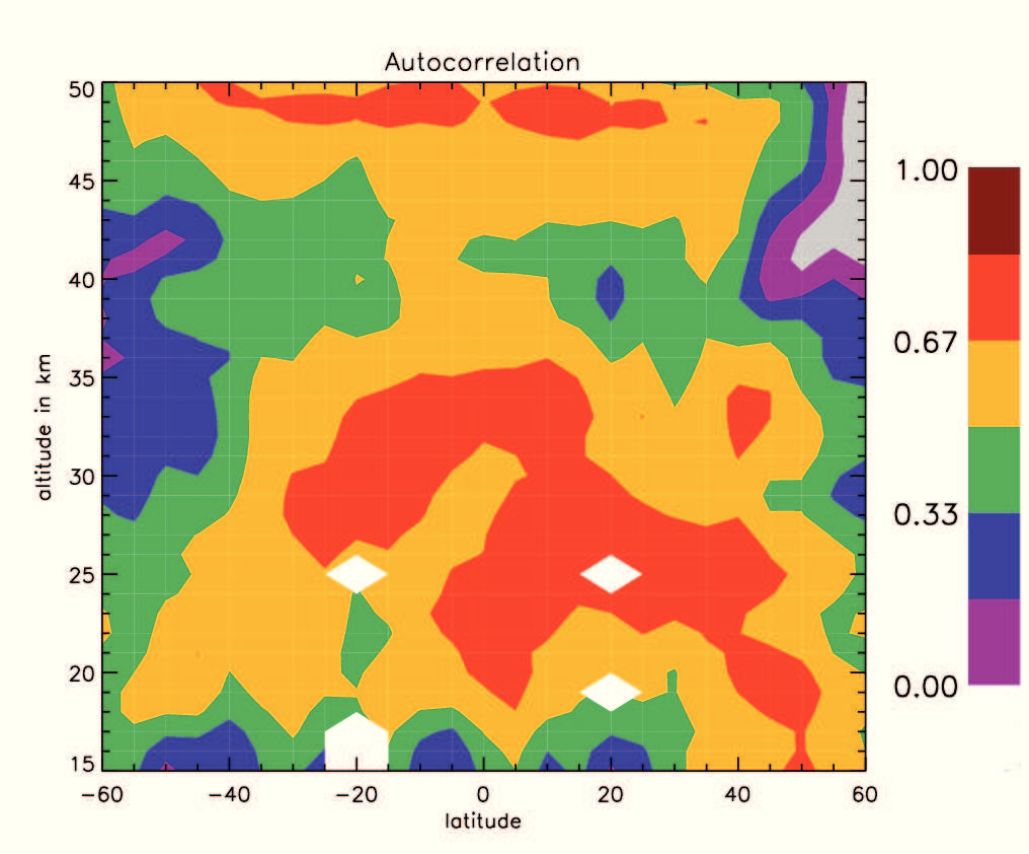

Figure 9.2: Autocorrelation from time series of SCIAMACHY limb O_3 as a function of latitude and altitude. Colours from magenta to dark red represent values between 0 and 1, which are typical for time series of environmental data.

The autocorrelation, estimated from the O_3 time series as described in Section 6.3, is shown in Figure 9.2 as a function of latitude and altitude. Autocorrelations clearly larger than 0 are obtained practically everywhere. The strongest autocorrelation is obtained in the lower to middle tropical stratosphere at values of around 0.8. Values above 0.5 hold well into the midlatitudes. The obtained pattern of autocorrelation is similar to that from SCIAMACHY limb O_3 for the period 2002-2008 shown in Mieruch et al. [2012].

9.3 The amplitude and phase of the annual oscillation

The regression model applied to time series of SCIAMACHY limb O_3 accounts for a range of periodic variabilities. Annual oscillation pat-

terns of any phase are captured by the combination of a sine and cosine term of 12 month period. The amplitude of the entire harmonic fit is, in most cases, not changed substantially by additional terms of 3 and 4 month period as described in Section 6.4.1. In the following, the amplitude of annual oscillation patterns is inferred from the 12 month terms (with a and b being their regression coefficients):

$$\begin{aligned} A\sin(\omega t+\phi) &= A\cos(\omega t)\sin\phi + A\sin(\omega t)\cos\phi = \\ &= a\cos(\omega t) + b\sin(\omega t), \end{aligned} \tag{9.1}$$

where t is time in months and $\omega = \frac{2\pi}{12}$. For t=0, this yields:

$$A\sin\phi = a. \tag{9.2}$$

The phase constant ϕ is given by $\phi = \arctan\left(\frac{a}{b}\right)$ [see e.g. Bergmann-Schäfer, 1998, p. 660] so that

$$A = \frac{a}{\sin\left(\arctan\left(\frac{a}{b}\right)\right)}. \tag{9.3}$$

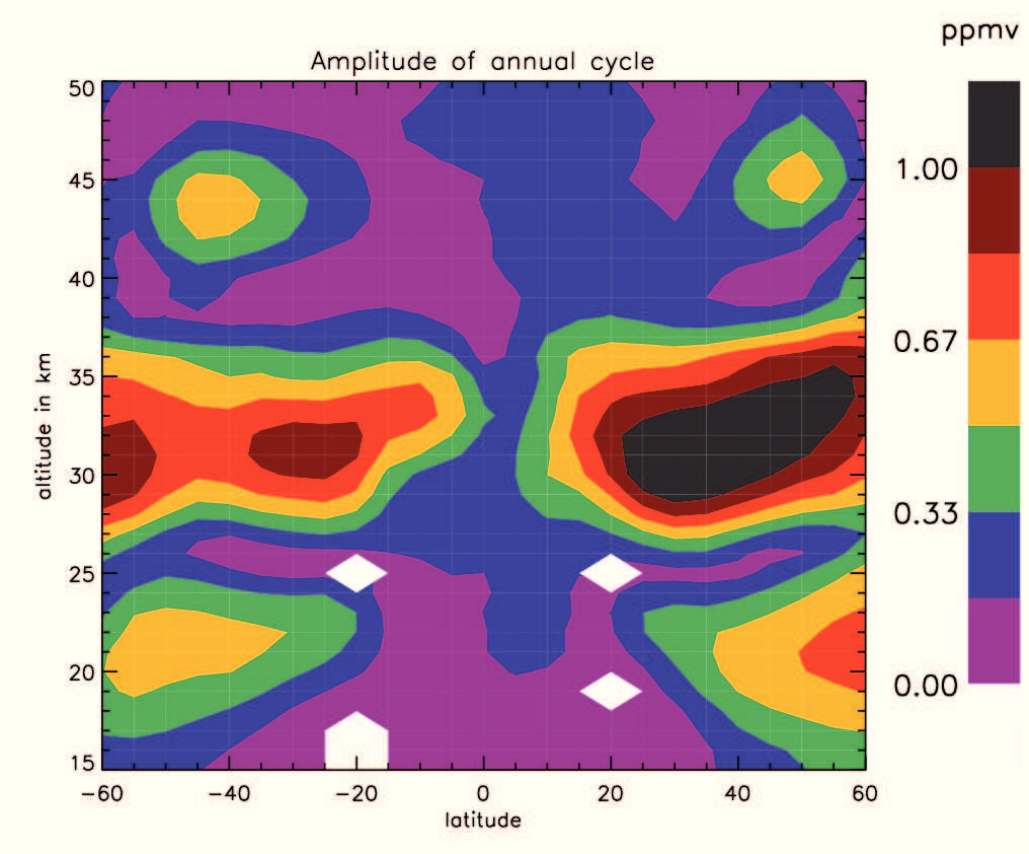

Figure 9.3: Amplitude of the annual oscillation in absolute units as a function of the latitude and altitude. Legend on the right: units of ppmv.

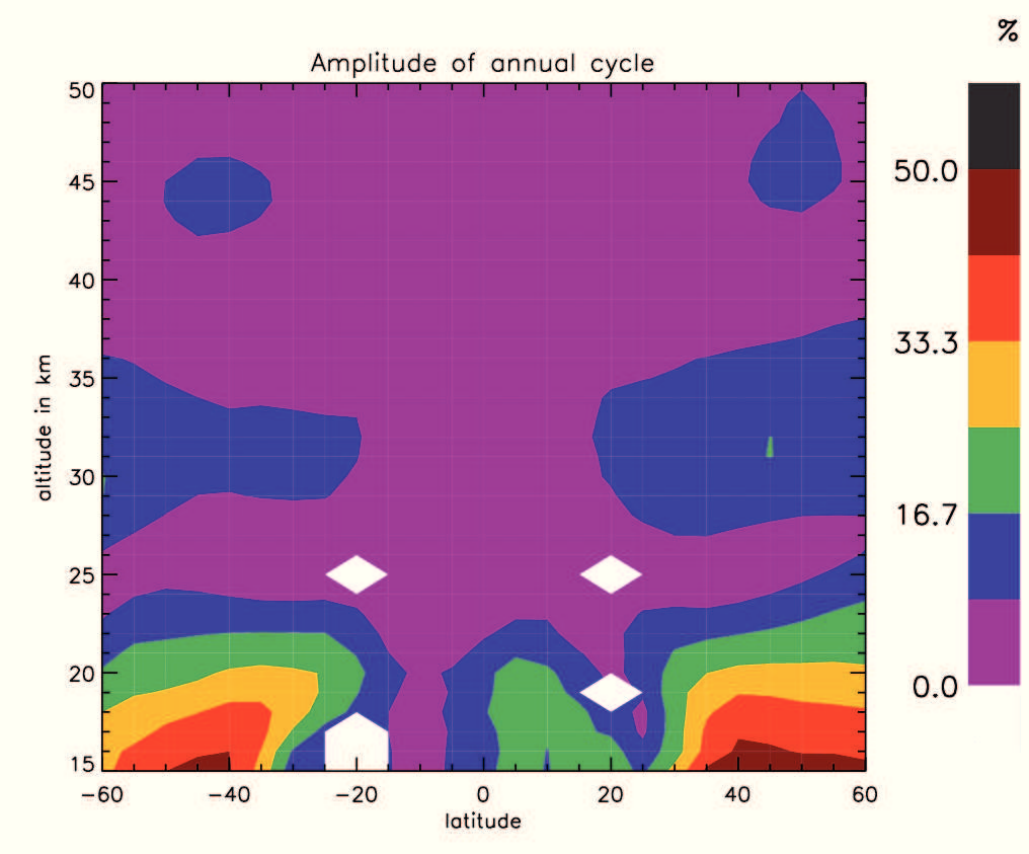

Figure 9.4: Same as Figure 9.3, but in relative units.

The amplitude of the annual oscillation is provided both in absolute and relative units in Figures 9.3 and 9.4. The relative units are obtained by scaling the absolute units by the mean value of the corresponding time series. In absolute units, maxima of amplitude extending throughout the extratropics are centred at altitudes of around 30-33 km. Secondary maxima of amplitude at around 45 km are seen in the latitude ranges of 40°N-50°N and 40°S-50°S. Regions of strong amplitude are observed in the lower stratosphere at northern and southern midlatitudes maximising at altitudes of around 20 km. In relative units, regions of strong amplitude appear at midlatitudes in the lowermost stratosphere maximising at altitudes near 15 km. The latter is similar to the amplitude of the annual oscillation shown in Eckert et al. [2014] for altitudes down to 10 km. Strong amplitude holds down to altitudes below 15 km in the extratropics. In Figure 9.4, a region of strong amplitude appears in the northern tropics at altitudes below around 20 km. Eckert et al. [2014] obtained a region of strong amplitude around 16-18 km at tropical latitudes. It appears to be somewhat more pronounced in the northern tropics than in the

southern tropics.

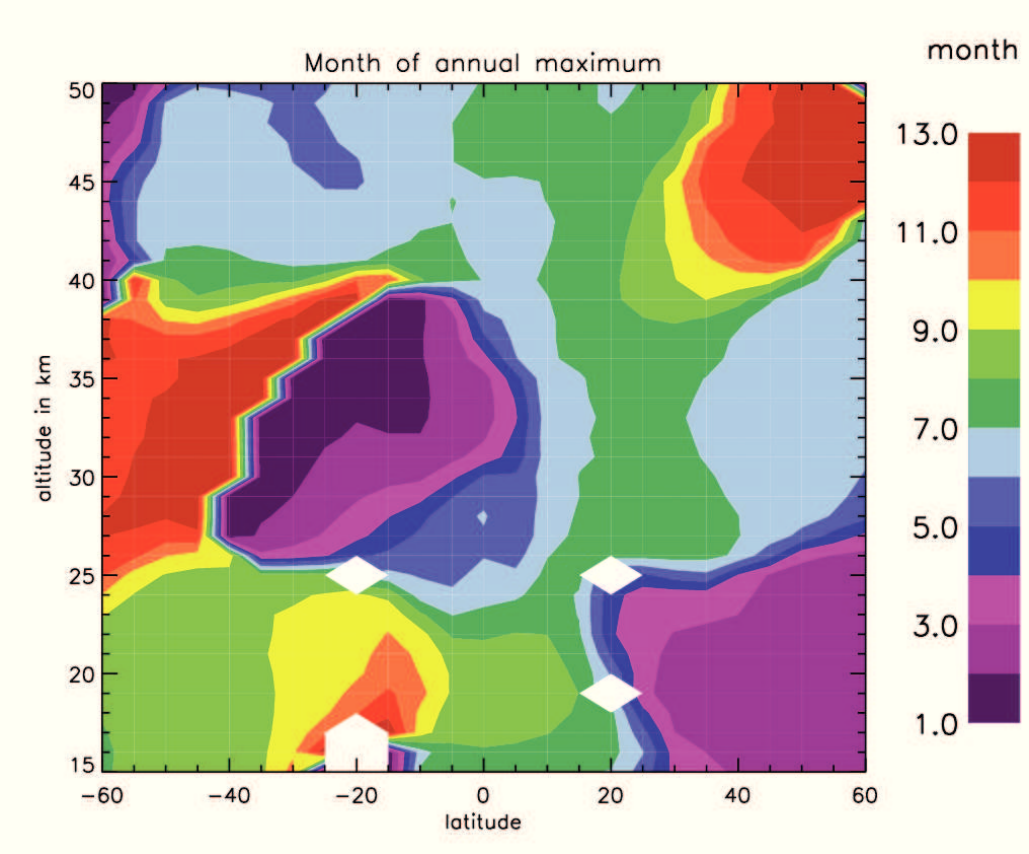

Figure 9.5: Phase of the annual oscillation as a function of the latitude and altitude. Legend on the right: the phase is specified as the number of the month at which the annual maximum occurs. 1-2 means that the annual maximum occurs in January and 12-13 in December.

Figure 9.5 shows the phase of the annual oscillation as a function of the latitude and altitude. The phase is specified as the number of the month in which the annual maximum of O_3 occurs: 1-2 means that it occurs in January (the beginning/end of January is equivalent with 1/2), 12-13 that it occurs in December, and similarly for each month between.

The mechanisms driving annual oscillation patterns of O_3 have already been described in detail in Section 5.2. For the midlatitudes, they can be summarised as follows:

- in the lower stratosphere, the annual cycle of O_3 is governed by transport effects maximising in late winter/early spring,
- in the middle stratosphere by photochemical O_3 production maximising in summer,

- and in the upper stratosphere by catalytic O_3 depletion maximising also in summer.

At midlatitudes of both hemispheres, this leads to the annual maximum of O_3 occurring in

- late winter/early spring in the lower stratosphere,
- in summer in the middle stratosphere, and
- in winter in the upper stratosphere.

Consistently, Figure 9.5 shows hemispheric asymmetries of the phase of the annual oscillation. At midlatitudes below 25 km, the annual oscillation maximum occurs in hemispheric late winter/early spring (around February in the north and August in the south). Between roughly 25 and 40 km in the extratropics, the annual oscillation maximum occurs in hemispheric summer (around June to July in the north and December to January in the south). Above 40 km at midlatitudes, this reverses with the annual maximum occurring in early winter of each hemisphere (around June at southern extratropics and around November to December north of 30-40°N).

As also described in Section 5.2, lowermost tropical stratospheric O_3 exhibits an annual oscillation pattern which has its maximum at the time of the boreal summer. Consistently, the annual maximum occurs around July/August close to the equator at altitudes up to more than 20 km in Figure 9.5.

9.4 The amplitude of the semi-annual oscillation

The amplitude of the semi-annual oscillation is inferred similar to that of the annual oscillation cf. Equation 9.3: 6 month regression terms are used instead of 12 month terms. In Figure 9.6, the amplitude of the semi-annual oscillation is shown as a function of the latitude and altitude. The pattern of amplitude is highly hemispherically symmetric and maximises in the tropical 30-35 km range at values of around 0.6 ppmv. The amplitude decays towards the subtropics and midlatitudes. Values close to zero are obtained in the southern hemisphere at latitudes between around 30 and 40°S. Another increase of amplitude

is observed at latitudes of around 60°S over a broad altitude range. Close to 60°N, an increase of amplitude is centred around altitudes of 40 km. Amplitudes close to zero are obtained in the broad latitude and altitude ranges of around

- 40°N-40°S above 45 km and
- 60°N-60°S below 25 km.

Similar regions of zero amplitude result when scaling the amplitude in relative units, i.e. with respect to the mean value of the corresponding time series. From O_3 time series from MIPAS/ENVISAT, which observed over the same period as SCIAMACHY, Eckert et al. [2014] obtained a similar distribution of amplitude of the semi-annual oscillation in the 60°N-60°S range. Their tropical maximum of amplitude is comparable in altitude and has values of around 0.5 ppmv. Close to 60°N and 60°S, similar increases of amplitude are seen by MIPAS/ENVISAT.

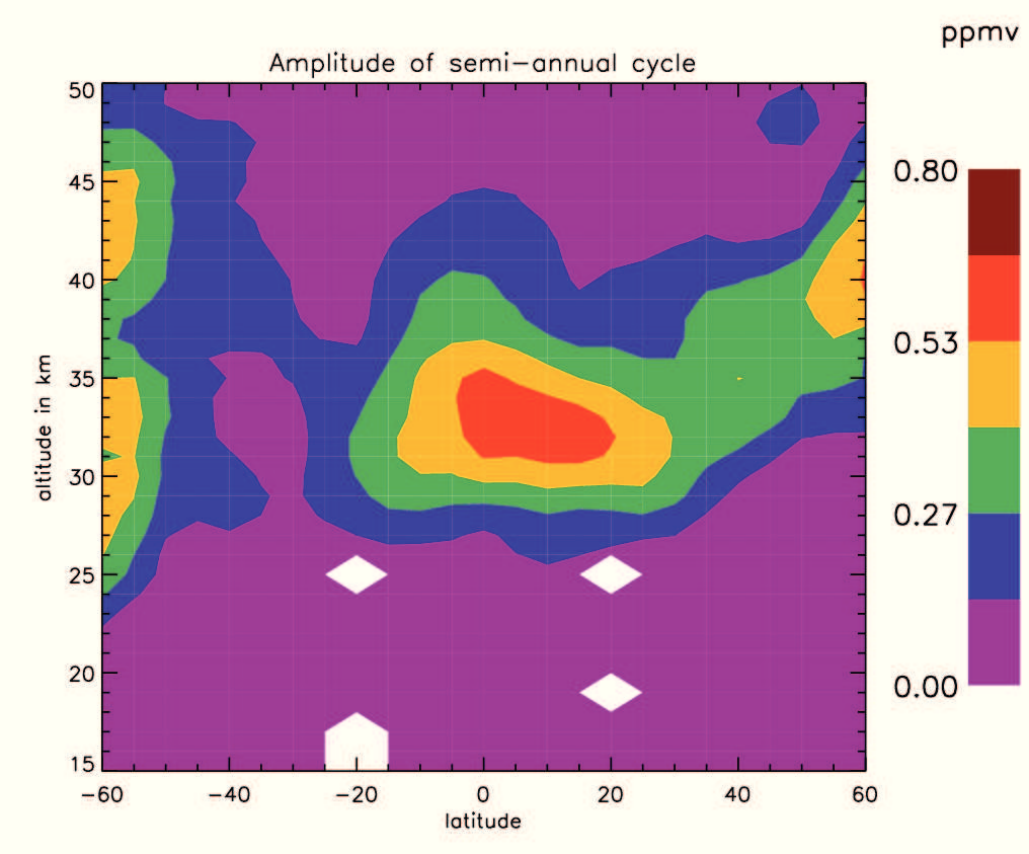

Figure 9.6: Amplitude of the semi-annual oscillation. Legend on the right: units of ppmv.

Seeing pronounced semi-annual oscillation patterns in

- the middle stratosphere (also reaching into the upper stratosphere) in the tropics and
- middle to upper stratosphere at midlatitudes

is consistent with Section 5.2. As described, this a result of

- photochemical O_3 production reflecting two equator passages of the Sun per year and
- the dominant patterns of annual variability being overlaid by out of phase secondary annual cycles,

respectively.

9.5 The QBO amplitude

The QBO amplitude is determined following Eq. 9.3. This approach, based on the superposition of a sine and cosine wave, applies to the combination of the 10 and 30 hPa Singapore winds which serve as QBO proxy (cf. Equation 6.5) as well. They are quasi-periodic and phase-shifted by a quarter of a period and hence behave in good approximation like the combination of sine and cosine.

The QBO amplitude of O_3 seen by SCIAMACHY is shown in Figure 9.7 as a function of the altitude and latitude. In the tropics, maxima of amplitude are seen in the 25-28 km range and the 30-36 km range. The lower maximum is seen at values of around 0.4 ppmv and the upper maximum at values of around 0.6 ppmv. Inferring the QBO amplitude of O_3 from MIPAS/ENVISAT, Eckert et al. [2014] obtained maxima in the tropics at the same altitude. Their upper maximum appears at values lower than ours by a factor of around 1.5. This is similar to the findings of Tegtmeier et al. [2013]. Comparing various satellite instruments within the time range from 1996-2010, SCIAMACHY shows a QBO amplitude above the average of instruments in the middle tropical stratosphere while MIPAS lies below the average.

The pattern of QBO amplitude seen by SCIAMACHY, shown in Figure 9.7, has a branch of notable amplitude extending up to latitudes of

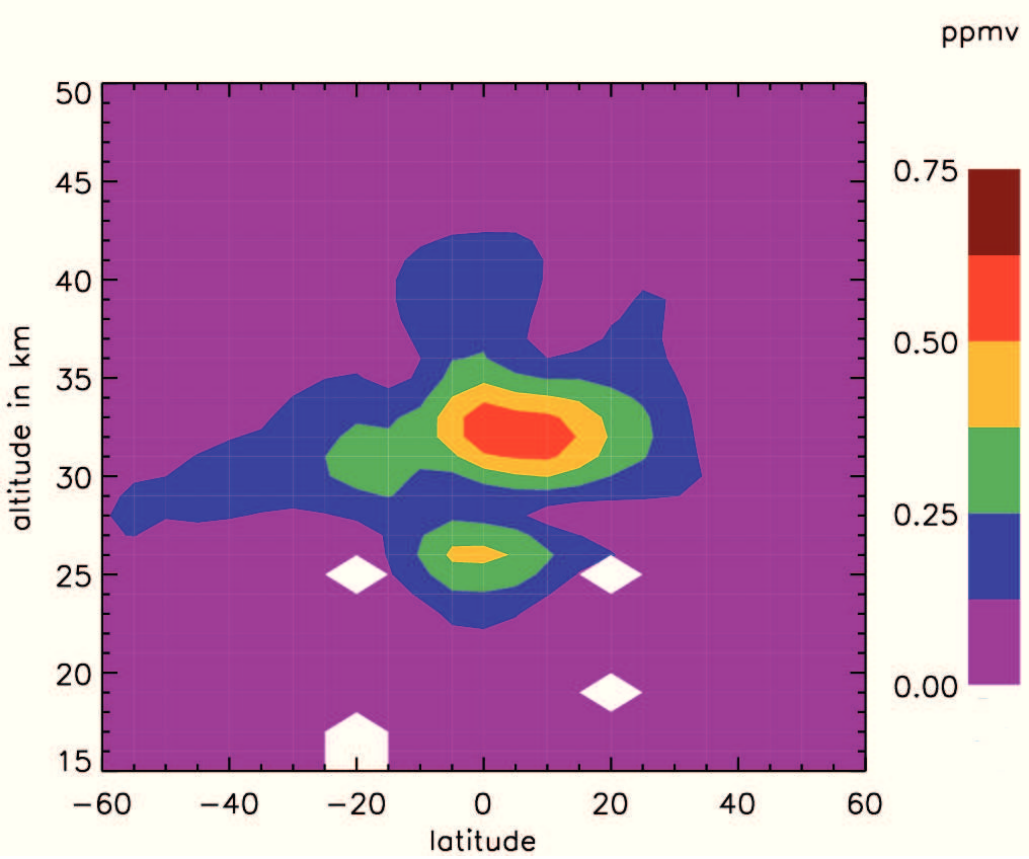

Figure 9.7: Amplitude of the quasi-biennial oscillation (QBO) in units of ppmv as a function of the latitude and altitude.

around 60°S in the 25-30 km range. This is evidence for extratropical QBO signatures in O_3. Both the maxima of QBO amplitude in the lower and middle stratosphere in the tropics and the occurrence of notable extratropical QBO signatures are consistent with the description of the QBO response of O_3 given in Section 5.3.

9.6 The solar cycle and ENSO response of O_3

Solar cycle

For the Mg II index, which serves as the solar cycle proxy in the regression, a maximum minus minimum change of 0.01 is assumed. The corresponding change in O_3 follows from the regression and is scaled in relative units. This scaling is with respect to the mean value of the analysed time series. The resulting solar cycle response of O_3 is shown in Figure 9.8. The values are mostly below 5%. On order

of magnitude, this is consistent with the expectation of a solar cycle response of few % per decade in Section 6.2.5.

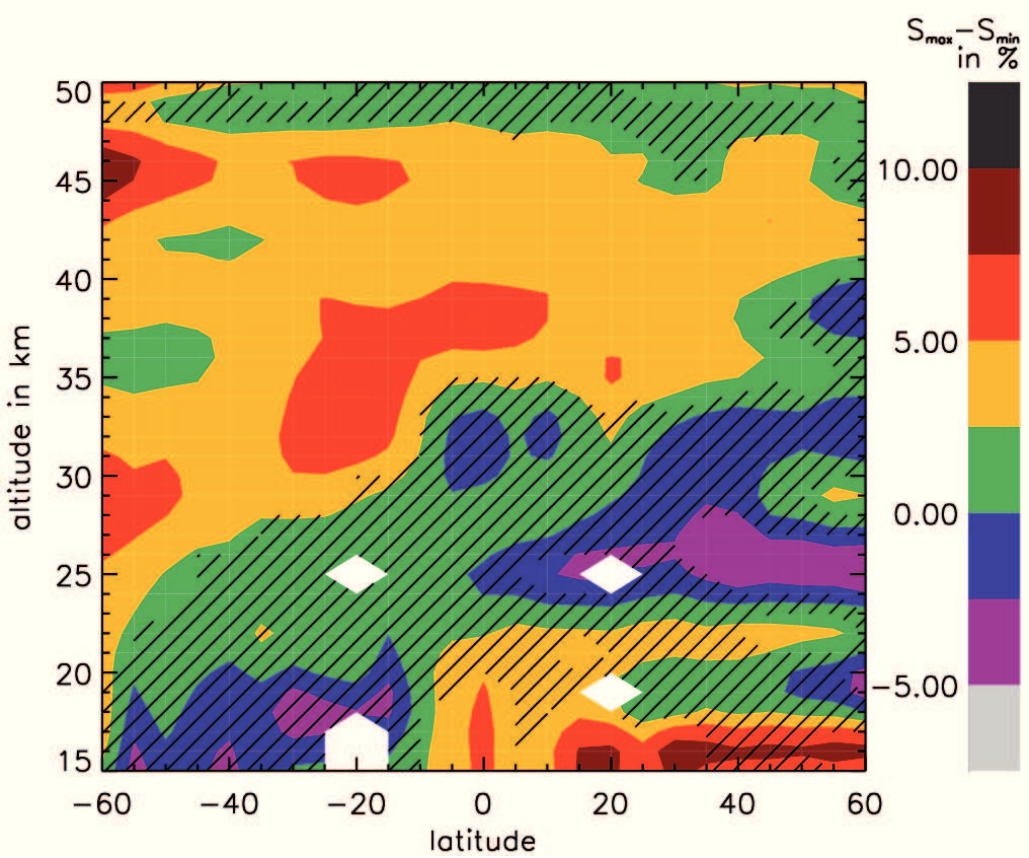

Figure 9.8: The solar cycle response estimated from time series of SCIAMACHY limb O_3 as a function of the latitude and altitude. Non-hatched areas are significances at the 2σ level. Legend on the right (units of %).

Analogous to the significance criterion for trends (Eq. 6.11), the criterion for the solar cycle term being significant at the 2σ level is the absolute ratio of the regression coefficient of the solar cycle and its uncertainty exceeding 2. As for the trend, the uncertainty follows from the covariance matrix of regression. In Figure 9.8, significances are non-hatched. The solar cycle response of O_3 seen by SCIAMACHY is mostly significant between 30-35 km and 45 km and insignificant below and above. This is holds from the tropics to the midlatitudes of both hemispheres.

From a merged satellite dataset spanning the years 1984-2011, Kyrölä et al. [2013] inferred the solar cycle response of O_3 with their pattern of significances being in close similarity to ours. Contrastingly, their values, also determined as the change in O_3 between solar maximum and minimum, tend to be smaller by a factor of up to 2. This

may be partly explained by analysing another time range, which spans more than 2 full solar cycles, and assuming another maximum minus minimum change of the solar cycle proxy accordingly.

ENSO

As described before, the N34 index serves as ENSO proxy with the time lag between the proxy and ENSO signatures in O_3 being accounted for. The regression coefficient of the N34 index is equivalent with the inferred change of O_3 per proxy unit (if the proxy changes from 0 to 1 unit, the associated change in O_3 is equal to the regression coefficient of the proxy). Scaling with respect to the mean value of the analysed time series yields the relative change per proxy unit used in the following. The time lag of ENSO signatures follows from the ENSO fit as described in Section 6.2.6.

The strength and time lag of ENSO signatures derived from time series of SCIAMACHY limb O_3 are provided in Figures 9.9 and 9.10. The latitude range of 20°N-20°S and the altitude range of 15-25 km are shown compliant with the range of use of the N34 index as ENSO proxy. The strength maximises in the 18-21 km range with the corresponding time lag being between 1 and 2 months. These findings are consistent with Randel and Thompson [2011] who inferred a maximum ENSO response of tropical O_3 in the 17-21 km range. As follows from Figure 9.10, the time lag of ENSO increases to typical values of 2-3 months above 21 km.

At the edge of the considered altitude and latitude range, i.e. near 15 and 25 km and near 20°N and 20°S, the ENSO strength decreases in value and/or blank spaces appear. The latter arise from the time lag of ENSO being not precisely determinable (which serves as an omission criterion for the results as described in Section 6.2.6). The range of use of the ENSO proxy, which comprises well the altitudes of the maximum ENSO response of tropical stratospheric O_3, is limited by these practical reasons.

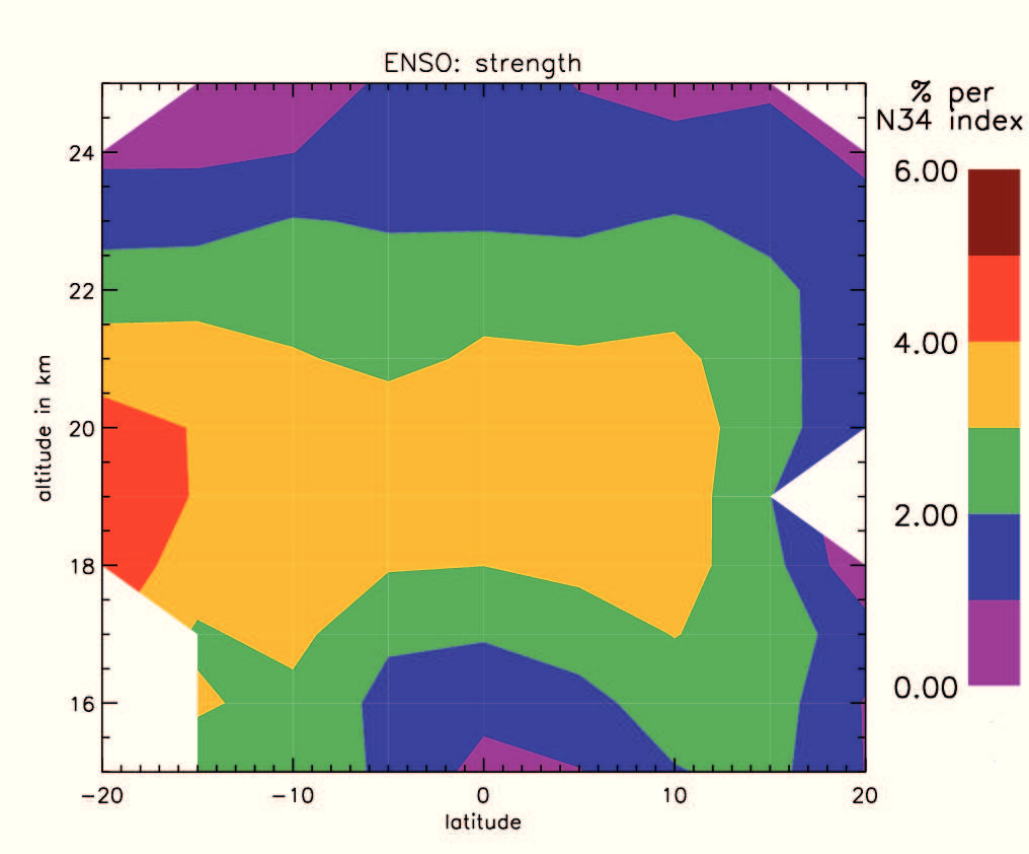

Figure 9.9: Strength of the ENSO response of O_3 resulting from SCIAMACHY limb measurements in the latitude range of 20°N-20°S and altitude range of 15-25 km. Legend on the right (units of % per N34 index).

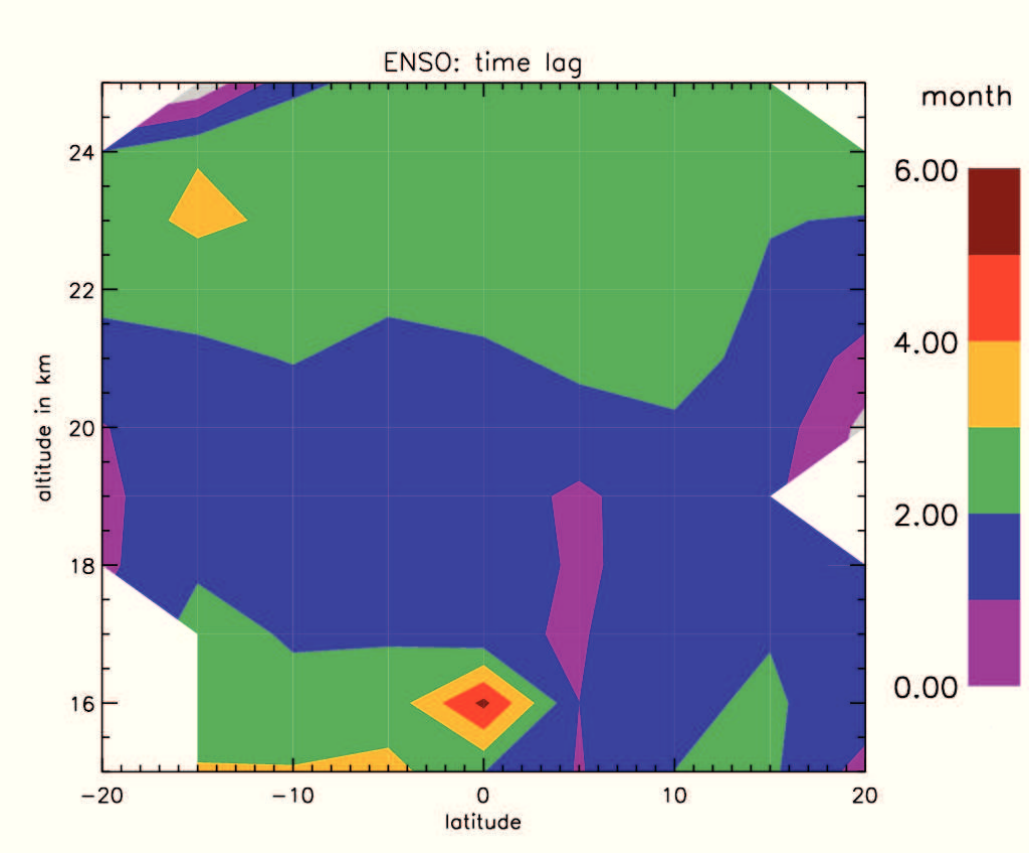

Figure 9.10: Time lag between the ENSO proxy and ENSO signatures in O_3 resulting from SCIAMACHY limb measurements in the latitude range of 20°N-20°S and altitude range of 15-25 km. Legend on the right (time lag in months).

10 Potential drivers of the observed O_3 trends

10.1 Halogen chemistry

As discussed in Section 6.1 , the EESC (equivalent effective stratospheric chlorine) proxy appropriately models long-term changes in O_3 provided that they are driven by halogens. Using the EESC proxy, trend studies on vertically resolved O_3 from SAGE I+II and SBUV(/2) inferred a maximum response of stratospheric O_3 in the midlatitude upper stratosphere roughly between 40 and 45 km [Rosenfield et al., 2005; Randel and Wu, 2007; WMO, 2007]. This suggests declining halogens being as well responsible for the positive O_3 trends from SCIAMACHY in the upper stratosphere between around 38 and 48 km (those trends were described in Section 9.2).

As an alternative to approximating the halogen response of O_3 by the EESC proxy, piecewise linear trends are employed. The transition of the piecewise linear trends is marked by turnaround points assumed in the late nineties similar to the turnaround of the EESC proxy. In Jones et al. [2009], positive post 1997 linear trends on the order of a few % per decade are inferred for the 35-45 km altitude range. Similarly, in Steinbrecht et al. [2006, 2009], increases of post 1997 linear trends with respect to pre 1997 trends of this order are found for the 35-45 km altitude range. With the studies of Jones et al. [2009] and Steinbrecht et al. [2009] covering time spans until 2008, they have considerable temporal overlap with the phase of SCIAMACHY from 2002-2012. Their findings in the 35-45 km altitude range and the positive O_3 trends from SCIAMACHY on the order of $5\% dec^{-1}$ in the 38-48 km range (described in Section 9.2) corroborate one another. To conclude, the positive upper stratospheric O_3 trends inferred in

this thesis from SCIAMACHY may be taken as indicative of declining halogens as the behaviour of upper stratospheric O_3 reported in the aforementioned studies.

Halogens are, by contrast, ineffective at O_3 depletion in the lower tropical stratosphere. As pointed out by Yang et al. [2006], this is explained by chlorofluorocarbons not releasing their halogen radicals immediately after their transition through the tropical tropopause. This favours the patterns of positive O_3 trends seen by SCIAMACHY in the lower tropical stratosphere (described in Section 9.2) being driven by factors different from halogens.

10.2 The tropical upwelling

As a result of a large vertical O_3 gradient above the tropical tropopause layer, O_3 shows a maximum response to the tropical upwelling in the lowermost tropical stratosphere (see also Section 6.2.6). Analysing a dataset merged between SAGE II and SHADOZ ozonesondes over the period 1984-2009, Randel and Thompson [2011] attributed negative tropical O_3 trends in the 17-21 km range to enhanced tropical upwelling. These negative trends are on the order of a few percent per decade at maximum. They are, however, largely determined by the years before the start of SCIAMACHY in 2002.

In Chapter 7, SCIAMACHY and the comparison instruments don't see any negative O_3 trends in the lowermost tropical stratosphere (although not agreeing in detail). Negative O_3 trends in the lowermost tropical stratosphere are not supported by O_3 trends from MIPAS/ENVISAT reported in Eckert et al. [2014] either. In the tropics below 20 km, MIPAS sees positive O_3 trends which are partly significant. Potential contradiction to [Randel and Thompson, 2011] is resolved by the most recent study of Aschmann et al. [2014]. The tropical upwelling is reported to have halted increasing around 2002 and levelled off thereafter. Thus, a long-term change in the tropical upwelling cannot be considered as main driver of the O_3 trends seen by SCIAMACHY.

10.3 Role of the subtropical mixing barriers

As an attempt to explain O_3 trend patterns obtained from MIPAS/ENVISAT (which observed over the same period as SCIAMACHY) a shifting of the subtropical mixing barriers was considered to be a potential driver in Eckert et al. [2014]. A hypothetical shift of the subtropical mixing barriers was suggested to explain trend patterns reasonably well. Among others, this shift was theorised to result in a hemispheric asymmetry in the extratropical stratospheric O_3 trends. This comprises positive trends in the southern hemisphere between 25 and 35 km and negative trends in the northern hemisphere between 25 and 30 km. These trend patterns are similar to the hemispheric asymmetry in extratropical O_3 trends seen by SCIAMACHY in the 25-35 km range, see Section 9.2. Thus, a shift of the subtropical mixing barriers is, similar to Eckert et al. [2014], a feasible explanation.

The patterns of positive and negative O_3 trends in the lower and middle tropical stratosphere seen by SCIAMACHY, see Section 9.2, are partly reproduced in Eckert et al. [2014]. At near-equatorial latitudes, the hypothetic shift of subtropical mixing barriers was theorised to result in clearly negative trends around the 30-35 km range and clearly positive trends at around 20 km. Around the near-equatorial 30-35 km range, the negative trends are, however, less pronounced than those seen by SCIAMACHY. A shift of the subtropical mixing barriers is, accordingly, not sufficient to be the only driver of the vertical shape of tropical O_3 trends seen by SCIAMACHY. Above 30 km, a 5° widening of the subtropical mixing barriers in northern as well as southern direction may, however, also give rise to an increase of the age of air in the middle tropical stratosphere [Stiller et al., 2012; Eckert et al., 2014]. In combination with effects of the NO_X chemistry, this offers an explanation for the negative O_3 trends seen by SCIAMACHY in the middle tropical stratosphere as described in Section 10.4.

10.4 Combined effects of the NO_X chemistry and age of air

Another explanation of the tropical O_3 trends seen by SCIAMACHY, positive trends in the lower tropical stratosphere and negative trends in the middle tropical stratosphere as described in Section 6.4.2 and 9.2, arises from the NO_X chemistry.

The effects of a long-term increase of NO_X, expected as a result of anthropogenic emissions throughout the 21 century, on the abundance of stratospheric O_3 have been investigated by diverse modelling studies. Performing model runs with perturbed nitrogen species but other forcings held fixed, the effects of the NO_X chemistry on O_3 were identified in Nevison et al. [1999]; Fleming et al. [2011]; Portmann and Solomon [2007]. These studies concur that enhanced NO_X results in an O_3 decrease in the middle stratosphere. This decrease maximises in the tropics between 30-40 km and is on the order of 1 % per decade [Fleming et al., 2011] or, in on centennial time scale, 10 % when scaled with respect to starting values of O_3 around the year 2000 [Nevison et al., 1999; Portmann and Solomon, 2007]. In the lower stratosphere, most studies predict smaller, but notable, increases of O_3 in response to increased NO_X. In the tropics, these increases are found to extend up to altitudes of 30 km in Nevison et al. [1999]; Portmann and Solomon [2007].

Performing model runs with different forcings acting together, another approach was made by Oman et al. [2013]. For each forcing, the impact on O_3 was identified by multivariate linear regression. For reasons of applicability of their method, the focus was on the upper stratosphere. In the tropics, their study consistently showed the largest O_3 decreases in response to increasing nitrogen species between pressure levels of 10 and 3 hPa which roughly corresponds with the 30-40 km range. In that, Oman et al. [2013] is consistent with the modelling studies mentioned before.

Clearly, the decreases of O_3 in response to increasing NO_X in the middle stratosphere arise from catalytic O_3 depletion by NO_X, described in Section 2.3.2. The O_3 increase in the lower stratosphere

is driven by photochemical buffering effects between NO_X and other families of O_3 depleting species such as HO_X and ClO_X. In addition, the formation of catalytically inactive reservoir species like HNO_3 and HCl is facilitated. Above altitudes of 20 km, the O_3 increase is the net effect of the photochemical buffering effects of NO_X and their catalytic O_3 depletion. In the lowermost stratosphere, NO_X may, like in the troposphere, be responsible for catalytic O_3 production. This was recognized by Burrows et al. [1979].

In the tropics, the aforementioned model studies indicated an O_3 decline above altitudes of around 30 km and an O_3 increase below in response to increasing NO_X. The O_3 decline maximises between 30 and 40 km and the increase between 20 and 30 km. A negative/positive response between 30-40 km/20-30 km coincide in altitude with the single-peak structure of negative O_3 trends in the middle tropical stratosphere/double peak structure of positive O_3 trends in the lower tropical stratosphere seen by SCIAMACHY, see Section 6.4.2 and 9.2, and confirmed by instrument comparisons in Chapter 7. However, the model scenarios of Nevison et al. [1999]; Portmann and Solomon [2007]; Fleming et al. [2011] inferred decreases of tropical mid-stratospheric O_3 of 1% per decade at maximum. This is definitely not sufficient to explain negative O_3 trends between 4-10 % per decade seen by SCIAMACHY and other instruments in the middle tropical stratosphere (cf. Figure 7.5). Thus, the response of tropical O_3 with respect to increasing NO_X suggested by modelling studies may offer an explanation only in combination with other sources of NO_X like changes in the partitioning of nitrogen species and/or transport.

Indeed, an increase of NO_X in tropical middle stratosphere around 10 hPa or 30 km is reported in the most recent study of Nedoluha et al. [submitted to JGR] using satellite measurements of stratospheric nitrogen species since the early 1990s. This increase is attributed to an increase of the mid-stratospheric age of air. With the age of air increasing, N_2O is photolysed to a higher extent resulting in a rise of NO_X.

10.5 Role of changes in the stratospheric temperature

Stratospheric O_3 is sensitive to changes in the stratospheric temperature because of the temperature dependence of the reaction rates as described in Section 5.2. A report on the current knowledge on the decadal evolution of stratospheric temperature is given in Randel et al. [2009a]; WMO [2011]. Lower stratospheric temperatures underwent changes in the years following the major volcanic eruption of Pinatubo in 1991 and levelled off after $\sim$1995. Similar findings are obtained for the middle and upper stratosphere. In the lower stratosphere, temperature datasets from satellites and radiosondes corroborate one another. In the middle/upper stratosphere, however, temperature data are mainly from satellites because other measurements have sampling limitations in this altitude range. There, issues with satellite measurements are still a source of uncertainty.

Including years until 2008, the lower stratospheric temperature record in WMO [2011] extends well into the period of SCIAMACHY (2002-2012) and stratospheric temperatures are indicated to have been rather constant (though, this suffers to some extent from remaining uncertainties for middle/upper stratospheric temperature). All in all, changes in stratospheric temperature are not favoured to be a significant driver of trends in stratospheric O_3 as seen by SCIAMACHY during its period from 2002-2012.

10.6 Summary

In this chapter, potential drivers of the O_3 trends seen by SCIAMACHY were discussed. Findings from other trend studies have been considered where relevant. In Section 10.1, declining halogens are favoured as driver of positive upper stratospheric O_3 trends from SCIAMACHY. A shift of the subtropical mixing barriers yields a potential explanation for patterns of O_3 trends seen by SCIAMACHY in the extratropics around the 25-35 km range, see Section 10.3. This may also contribute to positive O_3 trends in the lower tropical stratosphere. In the

middle tropical stratosphere, combined effects arising from the age of air and NO_X chemistry offer an explanation for negative O_3 trends, see Section 10.4. The tropical upwelling and the stratospheric temperature could not be identified to be a main driver in Section 10.2 and 10.5, respectively.

Part III

Bromine monoxide

11 Trends and variabilities of BrO as seen by SCIAMACHY

11.1 Time series

The SCIAMACHY limb BrO retrieval version 3.2 has been described in Section 4.4. The data are retrieved from 13 to 33 km in vertical steps of 1 km. The highest retrieval sensitivity is achieved from 16 to 26 km [Rozanov et al., 2011]. Hence, this altitude range is under analysis in this thesis. BrO data in units of number density are used.

In this chapter, BrO trends are inferred from time series of zonal monthly means for various latitude bands. The time series and trends are shown first for the midlatitudes and tropics, represented by the latitude bands of 60°N-50°N, 50°S-60°S, and 20°N-20°S, respectively. This is followed by a comprehensive time series analysis over all latitudes from 60°N to 60°S, in 5° steps. Linear changes/trends and periodic variabilities of BrO are presented as a function of the latitude and altitude.

Time series and trends from SCIAMACHY are compared to these from other measurements in Chapter 12. Few other data records have sufficient overlap in time and altitude to allow for a trend comparison to SCIAMACHY:

- the satellite-based BrO data from OSIRIS/Odin and
- the ground-based measurements of stratospheric BrO from the NDACC station of Harestua (60.2°N, 10.8°E).

For the trend comparison between SCIAMACHY and OSIRIS/Odin, zonal monthly mean BrO data are used. For the trend comparison between SCIAMACHY and ground-based measurements at Harestua,

data are selected from SCIAMACHY at latitudes and longitudes matching the site of Harestua.

11.2 Periodic variabilities of BrO

Figures 11.1 to 11.3 show time series of zonal monthly mean BrO from SCIAMACHY limb measurements for the latitude bands of 60°N-50°N, 50°S-60°S (midlatitudes), and 20°N-20°S (tropics). The altitudes are 17, 21, and 26 km, respectively. At midlatitudes, BrO has a pronounced annual cycle which has its maximum in winter at all 3 altitudes. Studies concur that this annual cycle is a result of the strong anticorrelation between BrO and $\mathrm{NO_2}$ [e.g. Shoede et al., 2006; Hendrick et al., 2009]. $\mathrm{NO_2}$ shows an out-of-phase annual cycle having its maximum in summer time as a result of enhanced photochemical release from reservoir species like $\mathrm{N_2O_5}$ and $\mathrm{HNO_3}$ [Brohede et al., 2007; Noxon, 1979]. Enhanced $\mathrm{NO_2}$ results in enhanced formation of bromine nitrate ($\mathrm{BrONO_2}$) and reduced BrO via reaction 3.1 (vice versa in winter).

At any altitude shown, the amplitude of the annual variation of BrO at northern midlatitudes is stronger than at southern midlatitudes. Using an early retrieval version of SCIAMACHY limb BrO, a similar hemispheric asymmetry of amplitude was already identified by Shoede et al. [2006]. This may reflect the amplitude of the annual cycle of $\mathrm{NO_2}$ being somewhat stronger in the northern hemisphere. For $\mathrm{NO_2}$ partial columns from 15-27 km, Hendrick et al. [2009] found the amplitude of the annual variation being somewhat stronger at the Observatoire Haut-Provence (43.9°N, France) than at Lauder (45.0°S, New Zealand).

Also in the tropics, the BrO time series from SCIAMACHY exhibit an annual variation which is of low amplitude at 21 km and clearly identifiable at 17 and 26 km. With the tropics represented by the 20°N-20°S band, this arises, however, from the annual cycles of both hemispheres interfering due to the broad meridional averaging. For 20°N-20°S, the annual maxima occur around the time of the boreal winter and, thus, resemble the annual cycle of BrO at northern mid-

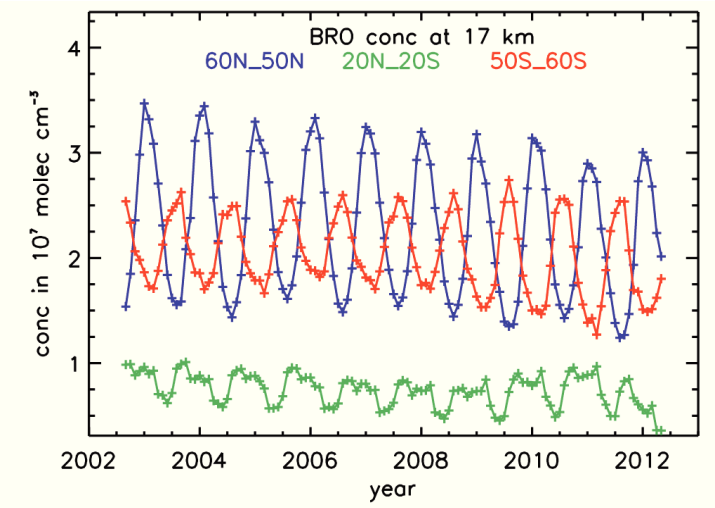

Figure 11.1: SCIAMACHY limb BrO at 17 km. The time series for 60°N-50°N, 20°N-20°S, and 50°S-60°S are shown for the period 08/2002 to 04/2012.

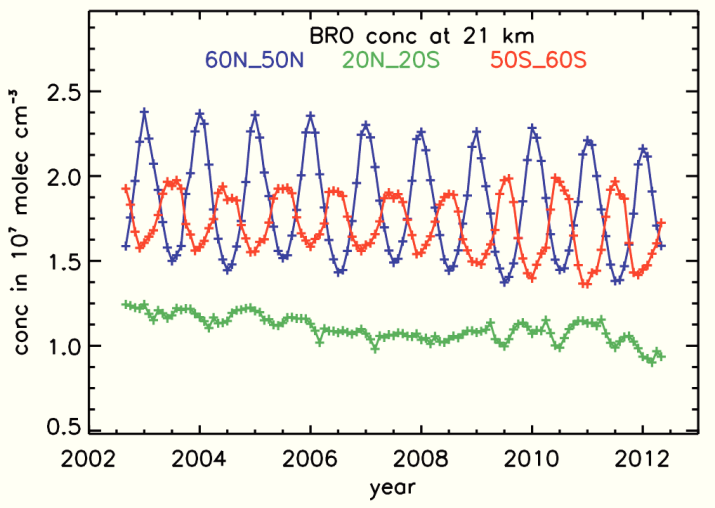

Figure 11.2: Same as Figure 11.1, but for 21 km.

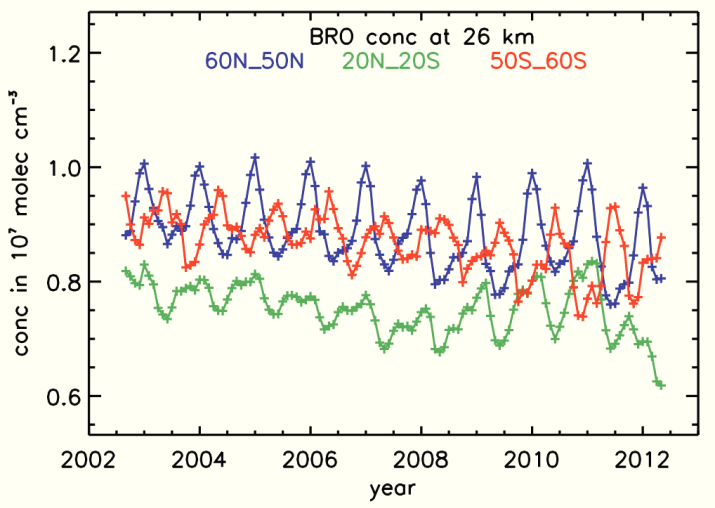

Figure 11.3: Same as Figure 11.1, but for 26 km.

latitudes. However, the annual maxima of BrO for 20°N-20°S are not as sharp as those for 60°N-50°N. They are flattened out or overlaid by secondary minima which is an indication for some out-of-phase annual cycle of smaller amplitude being overlaid. Being out-of-phase, the latter reflects the annual cycle of southern midlatitude BrO.

At the altitude of 26 km, SCIAMACHY shows enhanced amplitude of the annual oscillation for tropical BrO in the years 2008/2009, 2009/2010, and 2010/2011 and for southern midlatitude BrO in the years 2010 and 2011. It is not possible to verify this or to identify this as an artefact of satellite retrieval by comparison with other measurements of stratospheric BrO. The record of vertically resolved BrO of the NDACC station of Lauder (45.0S) ends in 2005 [Hendrick et al., 2009]. Annual variations of BrO seen by SCIAMACHY and OSIRIS/Odin show a different structure on the whole time-scale as follows from Section 12.1.2.

11.3 Time series analysis by multivariate linear regression

11.3.1 Regression model for BrO

In this Section, linear changes/trends in BrO are identified and quantified. The basic concept has already been introduced in Section 6.1 for SCIAMACHY limb $\mathrm{O_3}$. Compared to the $\mathrm{O_3}$ time series from SCIAMACHY in previous chapters, BrO time series considered here have the same length and reflect the vertical resolution of limb measurements as well. The preconditions for applying the concept of linear changes/trends are similar. Potential departures from linearity which accompany the anomalous strong annual oscillation amplitude of BrO in the years 2008-2011, mentioned in Section 11.2, still require consideration (see Section 11.3.2).

As done for $\mathrm{O_3}$ in Section 6.2, a statistic trend model is introduced:

$$Y_t = Lin(t) + Seas(t) + N_t. \tag{11.1}$$

It comprises linear and seasonal terms, $Lin(t)$ and $Seas(t)$, given in accordance with Eq. 6.2 and 6.3, respectively. Other terms are not

included (see also Section 11.3.3). Resulting trends are expressed in relative units of % per decade. This scaling is with respect to the mean value of the analysed time series. The trend model, in the following referred to as regression model, is fitted to any time series under investigation by multivariate linear regression following Section 6.3.

11.3.2 Fit quality

In Figures 11.4 to 11.9, BrO time series from SCIAMACHY limb for 60°N-50°N (northern midlatitudes) and 20°N-20°S (tropics) at the altitudes of 17, 21, and 26 km are shown in combination with their regression models. Each figure is divided into 4 panels. In the upper panel, the corresponding BrO time series (blue) is overlaid by its overall regression model (black). In the 2nd panel, the fit residuals, i.e. the difference between the time series and its regression model, are provided. In the 3rd and 4th panel, different components of the fitting curve are shown such as the seasonal and linear terms. Any of these terms is overlaid by the time series with other terms removed, e.g. the seasonal terms by the time series with the linear terms removed. The linear terms indicate a pronounced decrease at midlatitudes as well as in the tropics at any altitude.

In Figures 11.4 to 11.9, the seasonal terms are shown as combination of all harmonics included, i.e. of 12, 6, 4, and 3 month period (green), and as sum of the 4 and 3 month terms only (light blue). The latter mostly improve the closure between the time series and the regression model, but typically don't change the amplitude of the entire seasonal fit notably. Only for 21 km in the tropics, the contribution from the 4 and 3 month terms is comparable to those from the 12 and 6 month terms. The entire seasonal fits capture the annual oscillation patterns of BrO already described in Section 11.2 well.

At northern midlatitudes, the fit residuals are within ± 5 to $\pm 10\%$ of the fitted time series for any altitude. In the tropics, this is also the case at the altitude of 21 km. In the tropics at 17 and 26 km, the fit residuals partly exceed $+10\%$ from mid of 2008 to mid of 2011. These enhanced values of BrO coincide with the anomalous strong amplitude of the annual oscillation of BrO identified in Section 11.2. After mid of

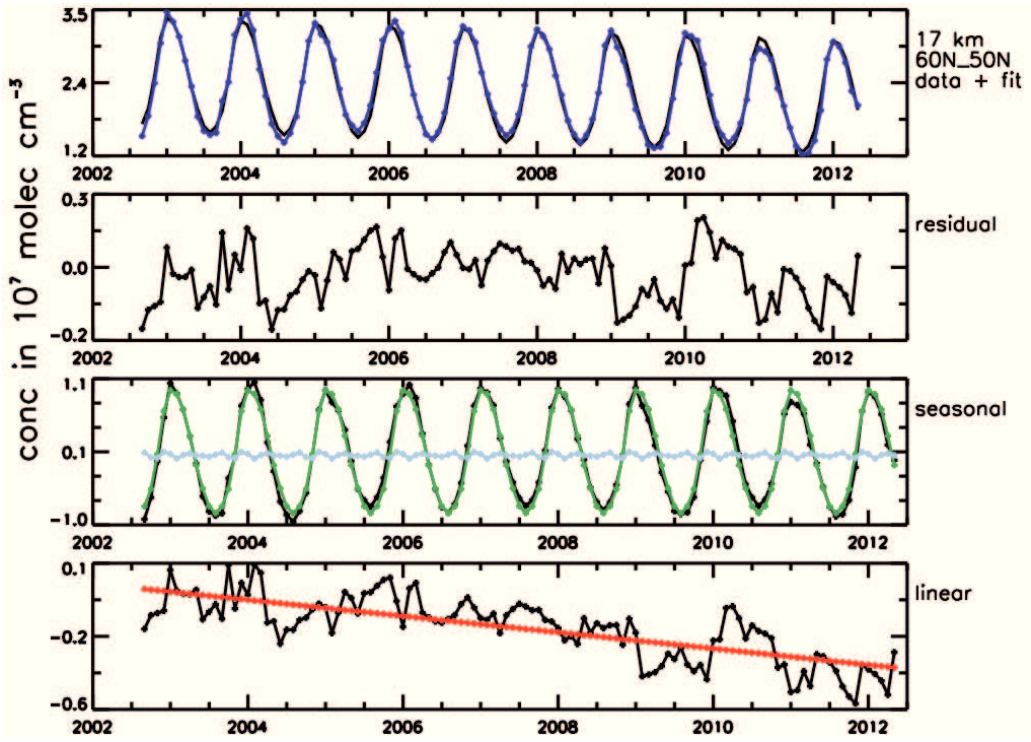

Figure 11.4: Regression model of SCIAMACHY limb BrO at 17 km for 60°N-50°N. In the upper panel, the time series (blue) is overlaid by the fit curve from the regression (black). Below, the fit residuals are shown. In the 3rd and 4th panel, different components of the regression model are shown such as the seasonal terms (green, light blue) and linear terms (red). The seasonal terms are provided as combination of all harmonics included, i.e. of 12, 6, 4, and 3 month period (green), and as combination of the 4 and 3 month terms only (light blue). The linear and seasonal terms are overlaid by the time series with other terms removed.

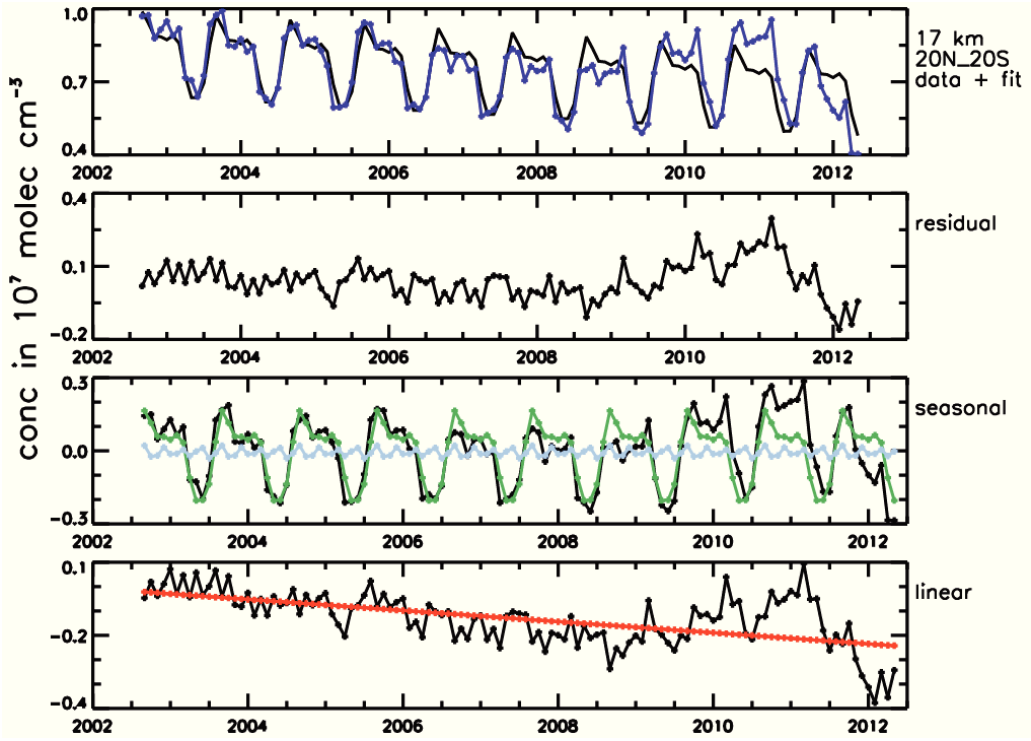

Figure 11.5: Same as Figure 11.4 but for 20°N-20°S.

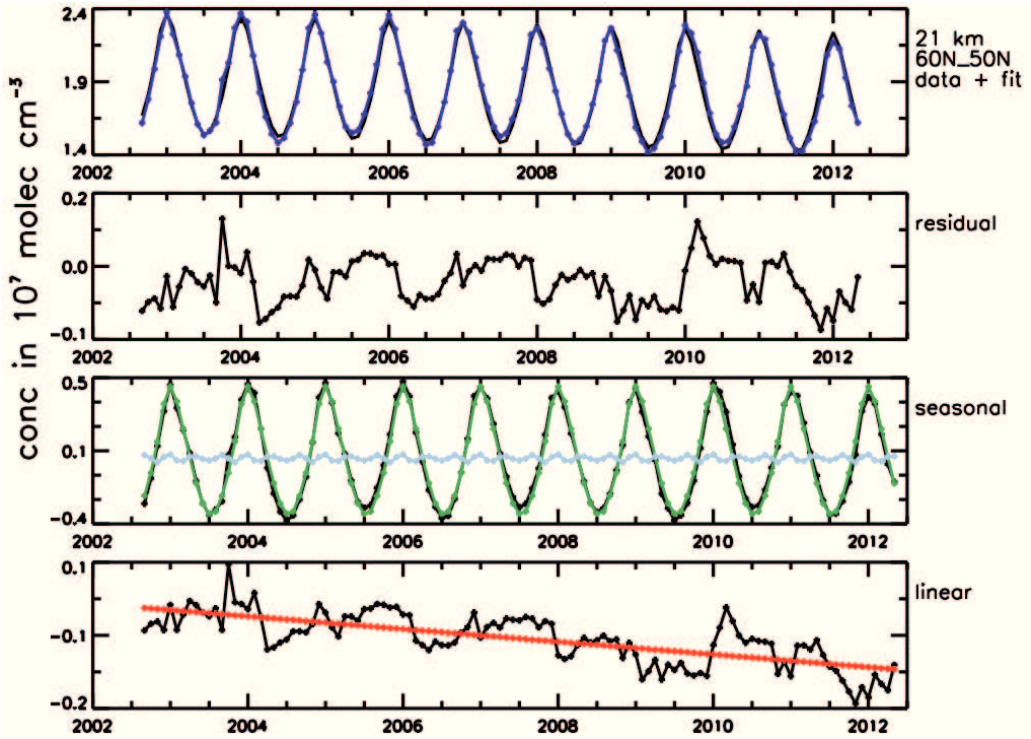

Figure 11.6: Same as Figure 11.4 but for 21 km.

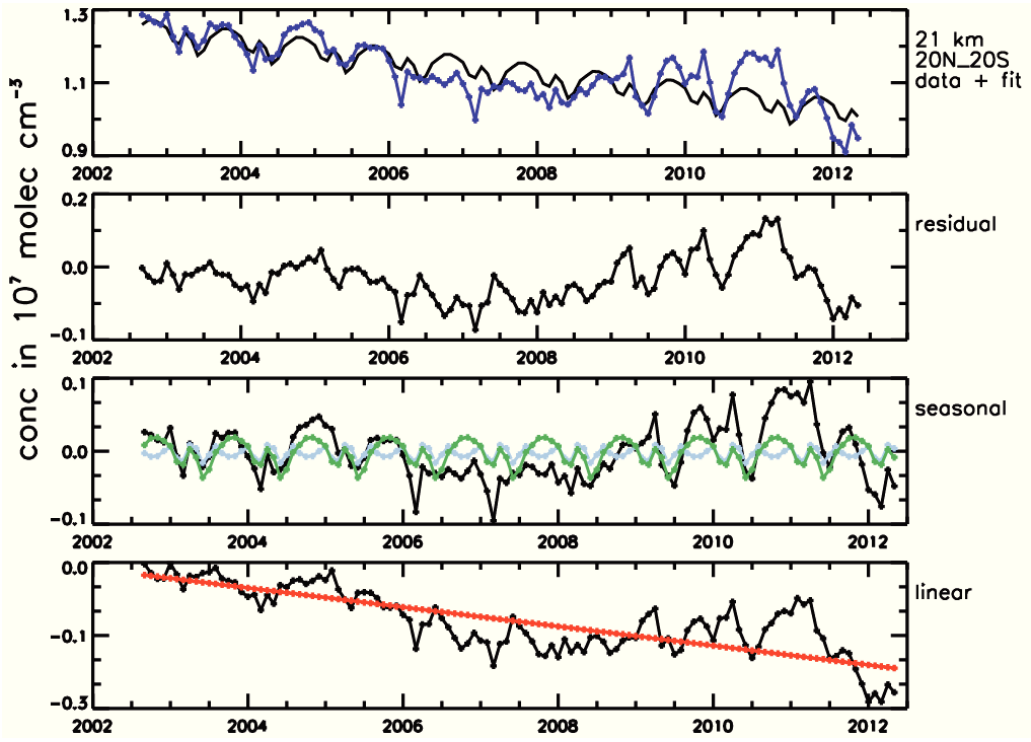

Figure 11.7: Same as Figure 11.4 but for 21 km and 20°N-20°S.

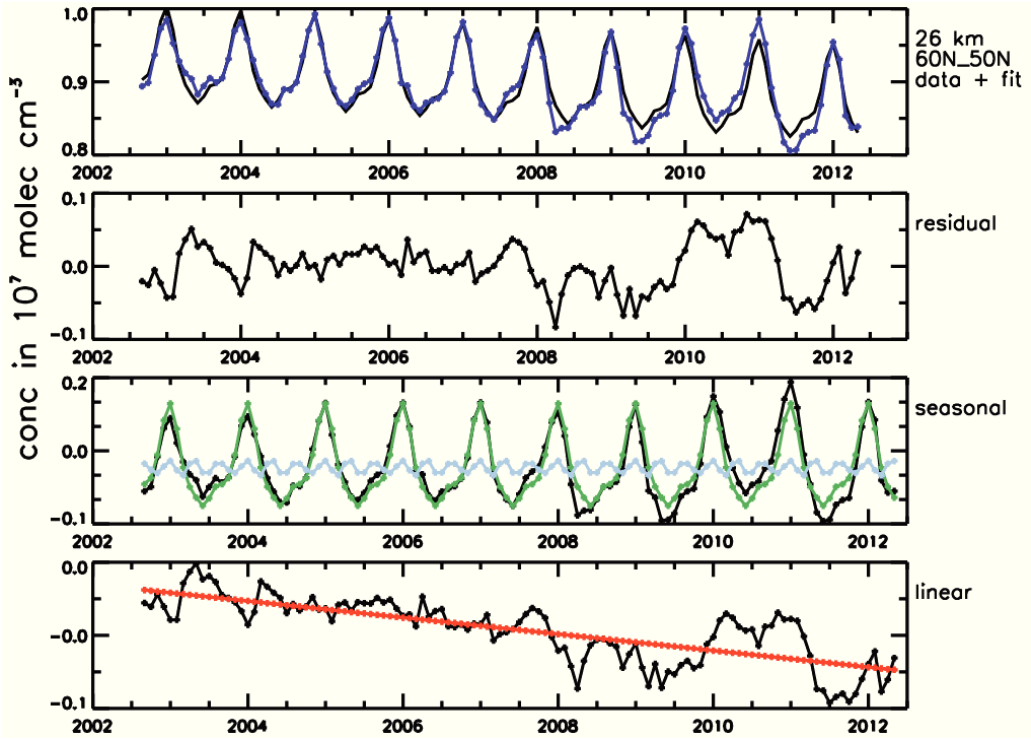

Figure 11.8: Same as Figure 11.4 but for 26 km.

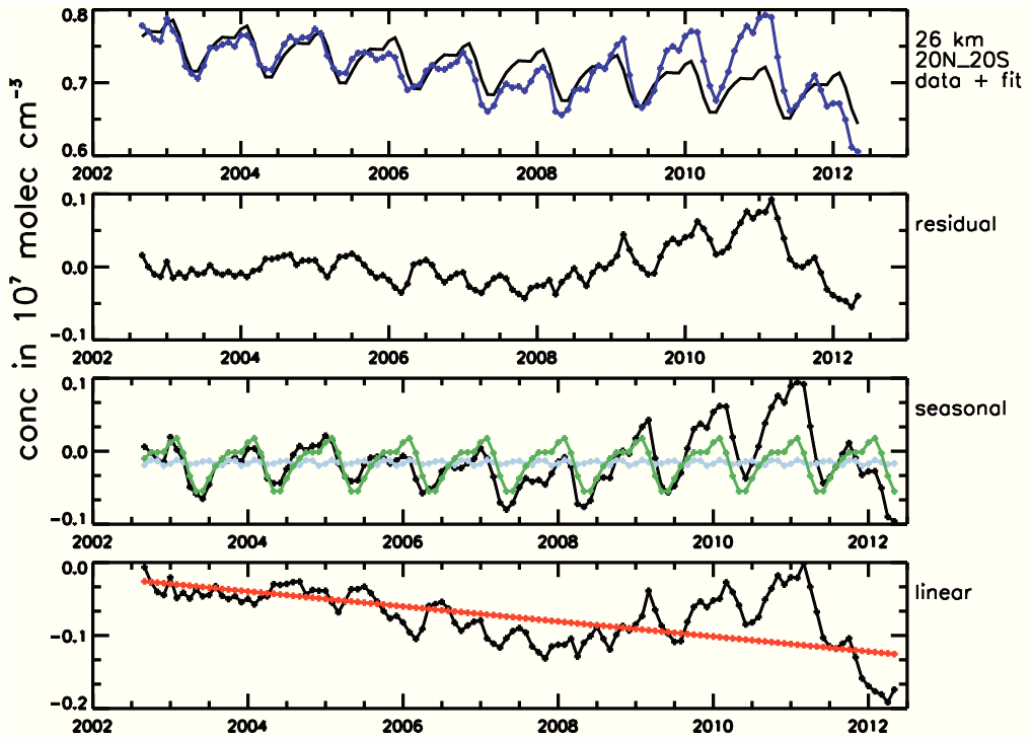

Figure 11.9: Same as Figure 11.4 but for 26 km and 20°N-20°S.

2011, the fit residuals decrease towards values similar to those before mid of 2008. Taken as a whole, the fit quality is considered to be sufficient. This is a criterion for the adequacy of the concept of linear changes/trends which was already discussed in Section 11.3.1. In the following, it is applied within the latitude range from 60°N to 60°S and the altitude range from 16 to 26 km for which the subset of altitudes and latitudes analysed here is considered to be representative of.

11.3.3 Trend profiles at midlatitudes and in the tropics

In Section 11.3.2,the analysis of selected time series at northern midlatitudes and in the tropics has identified clearly negative changes. Here, these changes are quantified as trends in units of % per decade (scaling with respect to the mean value of the analysed time series, cf. Section 11.3.1). The trend analysis is performed at any altitude from 16 to 26 km at 1 km vertical steps. In addition to the northern midlatitudes and tropics, the southern midlatitudes are covered as well. They are represented by the latitude band of 50°S-60°S.

For the midlatitudes and tropics, the resulting BrO trends are plotted as a function of the altitude in Figure 11.10. At any latitude band and altitude, the BrO trends are significant at the 2σ level (significance criterion given by Equation 6.11). At midlatitudes, the trends are roughly hemispherically symmetric. In the 20-26 km range, they have values relatively close to $-10\% dec^{-1}$. Below 20 km, they are larger and reach around $-20\% dec^{-1}$ at 16 km.

In the tropics, a contrast with respect to the midlatitudes appears. At 26 km, the BrO trend in the tropics is similar to those at midlatitudes. With decreasing altitude, the tropical trend profile becomes more negative than those at midlatitudes with the difference amounting for up to $10\% dec^{-1}$. Particularly at altitudes below 20 km, the trend uncertainty in the tropics is larger than that at midlatitudes. It should be minded that the retrieval quality of SCIAMACHY limb BrO decreases rapidly in the tropics below 19 km because of the relatively low BrO abundance [Rozanov et al., 2011].

The terms of the regression model for BrO, introduced in Section

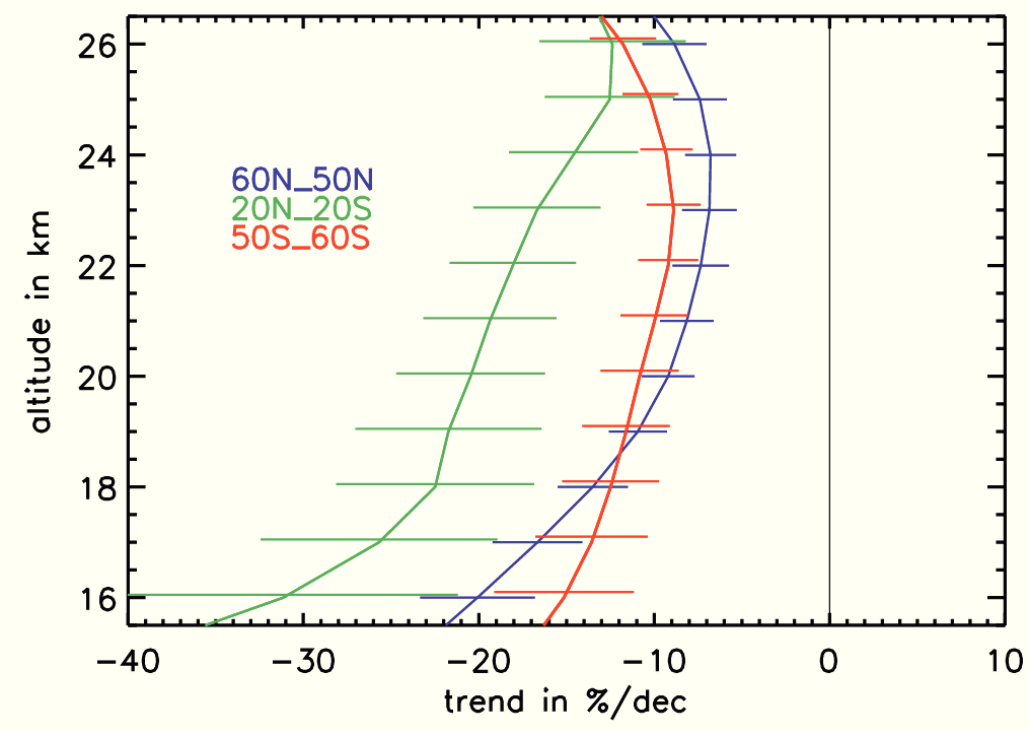

Figure 11.10: Vertical profiles of BrO trends derived from SCIAMACHY limb measurements for the 60°N-50°N, 20°N-20°S, and 50°S-60°S latitude band. The time span analysed is 08/2002-04/2012. Error bars: 1σ.

11.3.1, is a subset of the terms of the regression model for O_3 in prior chapters. The additional terms included for O_3 approximate variabilities related to the quasi-biennial oscillation (QBO), the solar cycle (SC), and the El Niño Southern Oscillation (ENSO), see Section 6.2. In Figures 6.10 and 6.11 of Section 6.4.2, the quality of the resulting O_3 trends has been demonstrated to be sensitive to these fit terms. A similar test with step-by-step including QBO, SC, and ENSO terms was done for BrO time series (using BrO trend profiles for 60°N-50°N, 20°N-20°S, and 50°S-60°S in the 16-26 km altitude range). It was found that QBO, SC, and ENSO terms have have a negligible influence on the resulting BrO trends and their uncertainties. These terms are omitted in the following.

Similar to O_3 in Section 6.4.2, the robustness of BrO trend profiles was tested by shifting the starting point or end point of the BrO time series forward or backward in 6 month steps, starting from the full phase of SCIAMACHY from 08/2002-04/2012. The forward shifts involve the time steps from 08/2002 to 02/2003, ..., 02/2004 to 08/2004 and the backward shifts those from 04/2012 to 10/2011, ..., 10/2010

to 04/2010. At midlatitudes and in the tropics, the shape of the BrO trend profiles is robust against these shifts. The trends and uncertainties vary by not more than few % per decade. The Trends remain significant negative at midlatitudes. In the tropics, the trends partly move into positive direction with time shifts of more than 1 year in forward or backward direction. Still, the tropical BrO trends remain significant negative inside the 16-26 km range. On the whole, the BrO trends from SCIAMACHY limb prove to be robustly negative.

11.4 BrO as seen by SCIAMACHY limb in a global view

In the following, different characteristics of the time series of zonal monthly mean BrO from SCIAMACHY limb measurements are presented as latitude altitude plots. These include the trends, the autocorrelation, and the amplitude of the annual oscillation. The amplitude of the annual oscillation is determined by the same approach as used for $\mathrm{O_3}$, see Eq. 9.3. The plots cover the latitude range of 60°N-60°S and the altitude range of 16-26 km. The latitude step is 5° and the altitude step 1 km. The limits of 60°N and 60°S are selected because of time series having gaps due to the lack of SCIAMACHY limb measurements in polar winter beyond these latitudes.

As follows from Figure 11.11, the BrO trends seen by SCIAMACHY are significantly negative for practically all latitudes and altitudes shown. Only around 20°N-30°N and 25 km, a few insignificances are obtained. In the northern hemisphere north of 10°N and above 20 km and in the southern hemisphere south of 50°S, the trend values are mostly of around $-10\%dec^{-1}$. Between 50°S and 10°N, the trend values are between $-10\%dec^{-1}$ to $-20\%dec^{-1}$ in the 24-26 km range and increase towards more negative values below. The autocorrelation shown in Figure 11.12 is positive for all latitudes and altitudes. The values are mostly between 0.5 and 0.8. The amplitude of the annual oscillation, given in relative units (scaled by the mean value of the analysed time series), is provided in Figure 11.13. At 16 to 18 km, maximum values of more than 20 % are shown over a broad latitude

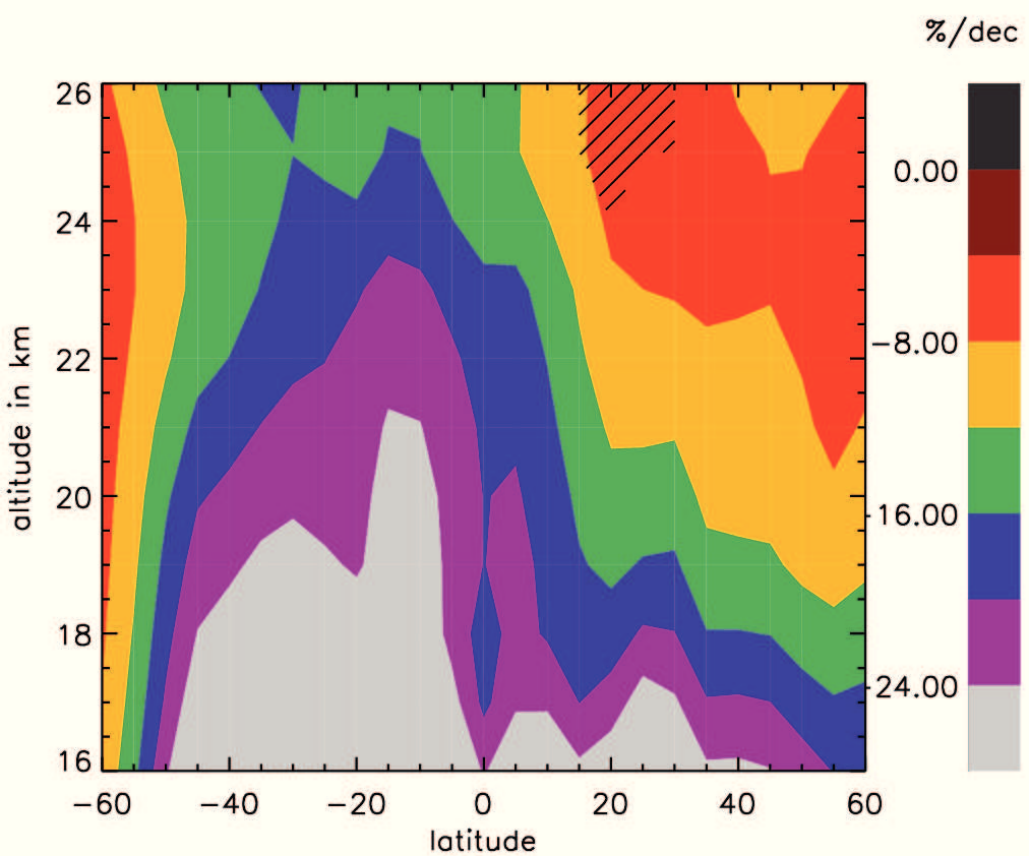

Figure 11.11: BrO trends seen by SCIAMACHY from 60°N to 60°S and 16 to 26 km. Legend on the right (units of $\%dec^{-1}$). Non-hatched areas are significances at the 2σ level.

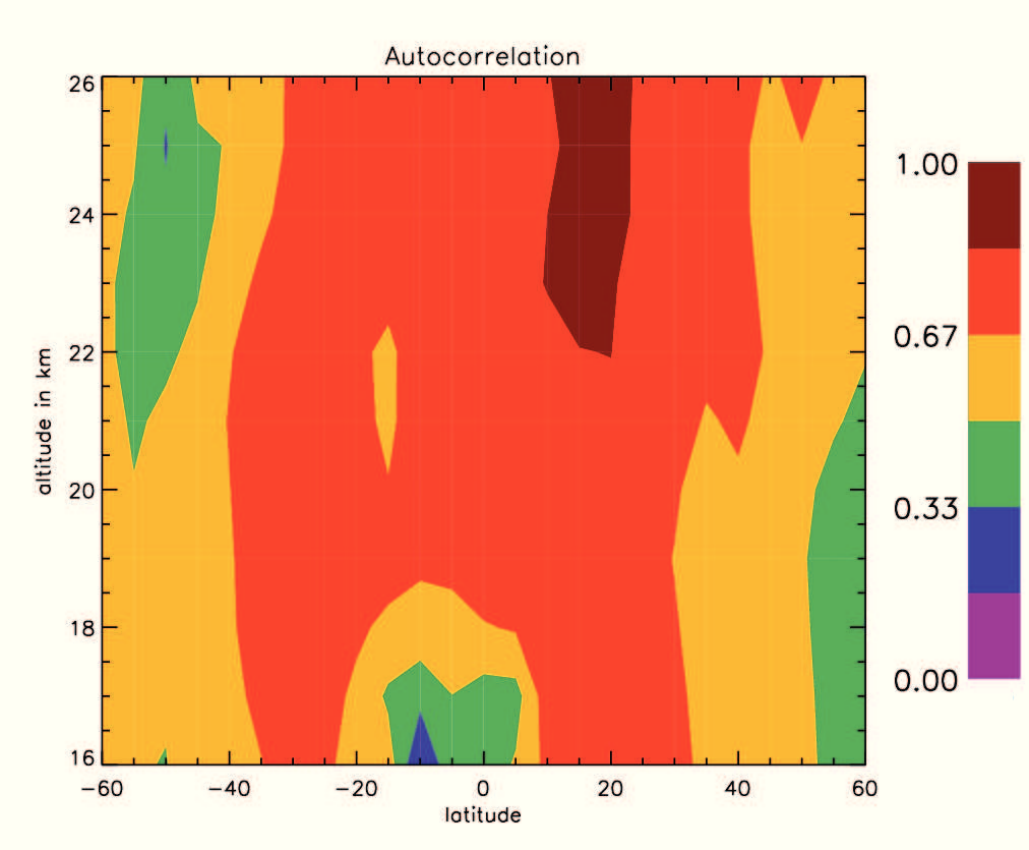

Figure 11.12: The autocorrelation of BrO time series from SCIAMACHY as a function of the latitude and altitude. Colours between magenta and dark red represent values between 0 and 1.

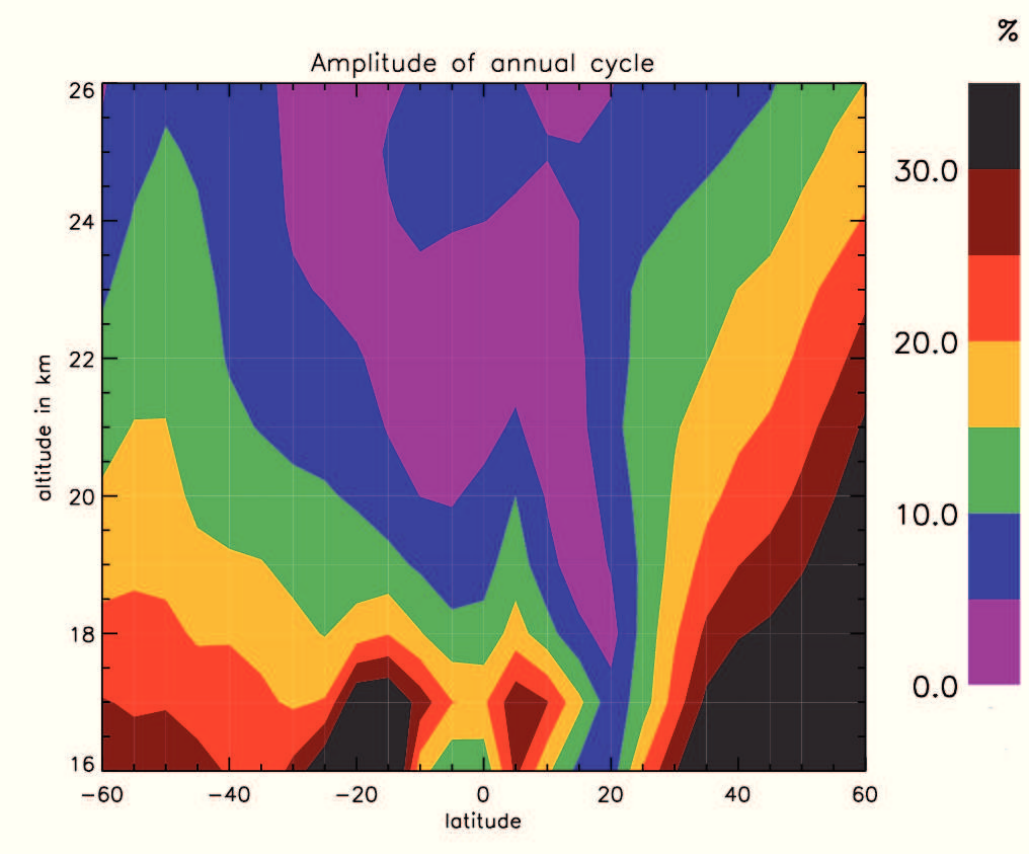

Figure 11.13: The amplitude of the annual oscillation of BrO seen by SCIAMACHY as a function of the latitude and altitude. Legend on the right (units of %).

range including the inner tropics and extratropics. Above 18 km, the annual amplitude of BrO typically increases from the tropics towards the midlatitudes. As pointed out in Section 11.2 for selected time series of BrO, the annual amplitude of BrO at northern midlatitudes is generally somewhat higher than that at southern midlatitudes. In Figure 11.13, a similar contrast is evident with the annual amplitude given in relative units. Above 18 km, its values at northern extratropics are found to be larger than those at the southern extratropics.

12 Comparison of BrO trends

12.1 Comparison to OSIRIS/Odin

12.1.1 Preparation and analysis of data

The instrumentation and orbit of OSIRIS/Odin has already been described in Section 7.2.1. For purposes of signal-to-noise optimisation, BrO data are retrieved from OSIRIS/Odin as daily zonal means at 10° wide latitude steps [McLinden et al., 2010]. Based on monthly mean BrO data, OSIRIS/Odin was validated against SCIAMACHY and ground-based measurements in McLinden et al. [2010]. This resulted in similarity as well as certain discrepancy. The validation against SCIAMACHY raised the following issues: the overall agreement between SCIAMACHY and OSIRIS/Odin was of around 30-40%. In addition, annually varying patterns of difference were evidenced.

Data from OSIRIS/Odin are available from `http://osirus.usask.ca/`. This Section is based on BrO data of version 5-00 (and version 5-01 for months after 10/2010). The comparison of BrO trends between SCIAMACHY and OSIRIS/Odin is made at tropical latitudes with OSIRIS/Odin data from measurements at AM local time being used only, see Section 7.2. In the following, BrO data from OSIRIS/Odin for the latitudes from 25°N to 25°S are in the focus (as mentioned before, the data are available in 10° steps). Data selection criteria following McLinden et al. [2010] are applied: BrO data from OSIRIS/Odin are omitted if the relative retrieval error exceeds 100%, the measurement response of the retrieval is below 0.67, or the mean solar zenith angle of the measurements is larger than 87°.

The orbit of OSIRIS/Odin is drifting [McLinden et al., 2010]. The equator crossing time of OSIRIS/Odin at morning conditions has shifted from values close to 6:00 AM during its first years of mission

towards values between 6:30 and 7:00 AM. Starting in 2008/2009, the orbit has drifted back and reached again equator crossing times close to 6:30 AM around 2011/2012. Hence, the record of OSIRIS/Odin may reflect photochemical variations of BrO during daytime. Uncorrected, they may be misidentified as a trend in BrO. Thus, a photochemical correction is performed using the PRATMO photochemical box model [McLinden et al., 2010, and references therein]. PRATMO provides BrO values as a function of local time/solar zenith angle and is available as look-up tables in 2.5° latitude steps and sub-monthly time steps.

On a daily basis, the BrO data selected from OSIRIS/Odin are corrected to the local time of SCIAMACHY. This is done by assuming linear changes of BrO between adjacent values of PRATMO and performing linear interpolation. At sunrise conditions, this approach may be incomplete due to rapid photochemical variations of BrO. If the latter become relevant, the photochemical correction is relatively large so that any correction error may have an unproportionally strong impact. Sunrise conditions are filtered by omitting data with the mean solar zenith angle exceeding 87°. Here, this criterion is extended as follows: linear interpolation between adjacent PRATMO values is made only if their relative difference is less than 5 %. Otherwise, data are not corrected photochemically and excluded from further analysis.

For the trend comparison, BrO data from SCIAMACHY binned horizontally by 5° latitude $\times$ 15° longitude are used. All BrO data available at latitudes from 25°N to 25°S are selected and monthly means are calculated. The data from SCIAMACHY are excluded for any month with OSIRIS/Odin having no data. The monthly mean time series resulting for SCIAMACHY and OSIRIS/Odin are subsequently used in the trend analysis:

- The results are presented for the altitudes of 24 and 26 km. Below, the time series are fragmented because of the exclusion of data. The vertical step of 2 km is defined by the BrO retrieval from OSIRIS/Odin, which is highly robust at the altitudes of 24 and 26 km [McLinden et al., 2010].

- The time range of analysis is 05/2004-02/2012. Before and after,

all data are excluded at 24 km and large parts at 26 km. Within the selected time range, only few data gaps are obtained.

As before, trends are determined by multivariate linear regression with the autocorrelation being accounted for, see Section 6.3. The regression model used comprises linear terms and harmonics of 12, 6, 4, and 3 month period. In principle, the basic equations of the regression apply to time steps of more than 1 month as well. Any month excluded from analysis, for reasons mentioned before, results in a time step of 2 months (n consecutive months excluded in a time step of n+1 months). Only the handling of autocorrelation requires modification. The noise values N_{t+n+1} and N_t are related via the following approximation (cf. Eq. 6.12):

$$N_{t+n+1} = \epsilon_{t+n+1} + \ldots + \Phi^{n+1} N_t \approx \epsilon_{t+n+1} + \Phi^{n+1} N_t, \tag{12.1}$$

with ϵ_{t+n+1} being the white, i.e. uncorrelated, noise. Accordingly, $-\Phi$ is replaced by $-\Phi^{n+1}$ in matrix 6.20 at the appropriate position.

12.1.2 Comparison of time series and trends

As described in Section 12.1.1, issues are known from validating OSIRIS/Odin against SCIAMACHY in McLinden et al. [2010]. These are reflected in Figure 12.1 which shows the BrO time series obtained from SCIAMACHY and OSIRIS/Odin for the altitude of 24 km: OSIRIS/Odin shows generally smaller values of BrO than SCIAMACHY. The annual oscillation shown by OSIRIS/Odin is, however, stronger and different in phase. While the tendency of OSIRIS/Odin towards smaller values is rather uniform with latitude, the difference in the annual variability arises mainly from the southern edge of the analysed latitude band. With respect to trends, this is, however, not necessarily a source of error:

- As pointed out by McLinden et al. [2010], the overall difference between SCIAMACHY and OSIRIS/Odin may arise, for large parts, from systematic errors at satellite retrieval. BrO trends given in relative units are, however, not necessarily affected by systematic errors.

- At time series analysis, annually varying patterns are accounted for by harmonic regression terms which are able to adjust a wide range of phase and amplitude.

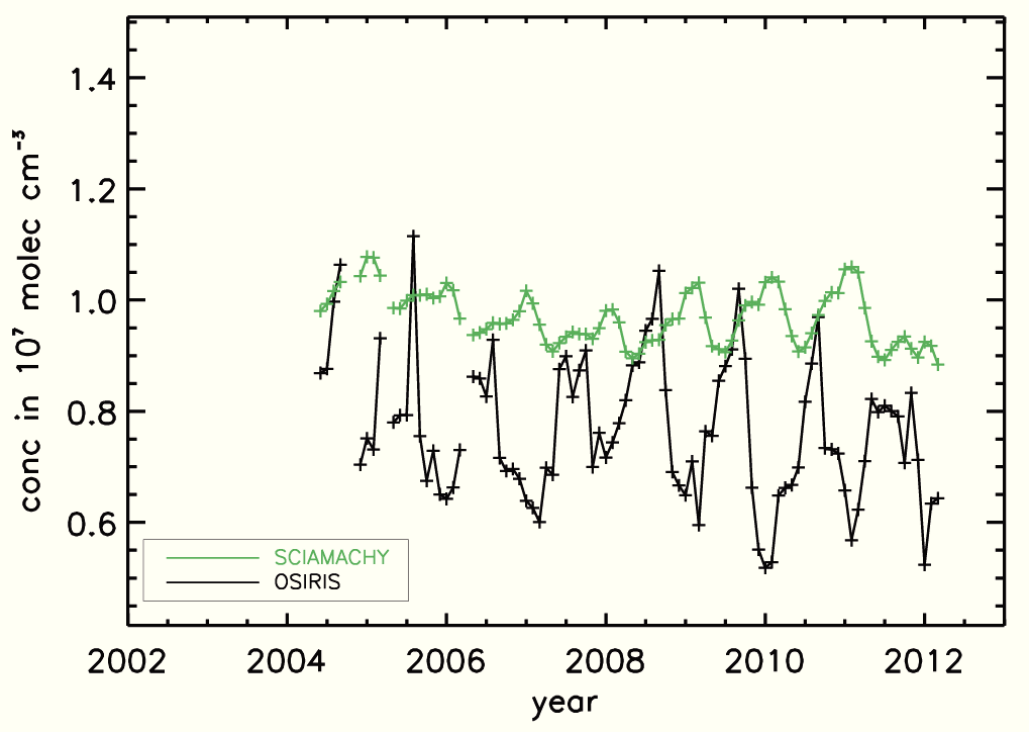

Figure 12.1: Comparison of BrO time series from SCIAMACHY and OSIRIS/Odin at the altitude of 24 km. Both time series represent the tropics. The time span covered is 05/2004-02/2012. OSIRIS/Odin has been photochemically corrected to account for photochemical variations of BrO during daytime.

In Figure 12.2, the BrO trends from SCIAMACHY and OSIRIS/Odin at the altitudes of 24 and 26 km are shown. Both instruments are in good agreement and see significant negative trends close to $-15\% dec^{-1}$. Their detailed values are provided in table 12.1.

	24 km	26 km
SCIAMACHY	-14.8 ± 4.6	-12.3 ± 5.2
OSIRIS/Odin	-14.7 ± 6.6	-13.6 ± 6.3

Table 12.1: BrO trends from SCIAMACHY and OSIRIS/Odin at the altitudes of 24 and 26 km (in units of % per decade).

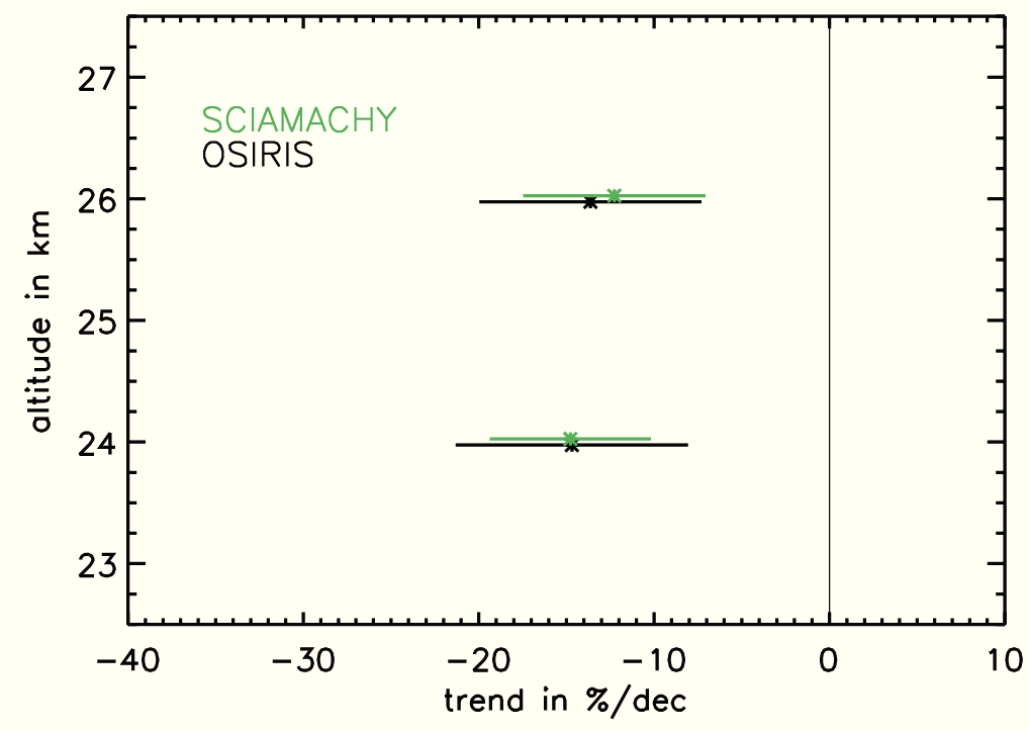

Figure 12.2: Comparison of tropical BrO trends between SCIAMACHY and OSIRIS/Odin at the altitudes of 24 and 26 km. The analysed time span is 05/2004-02/2012. Error bars: 1σ.

12.2 Comparison to ground-based measurements at Harestua

12.2.1 Ground-based measurements of stratospheric BrO

In the validation study of Hendrick et al. [2009], the BrO data version 3.2 from SCIAMACHY limb has already been compared to BrO data from ground-based UV-visible measurements (GB UV VIS) from the NDACC station of Harestua, Norway. Both the record of SCIAMACHY and Harestua GB UV VIS were separated into measurements at morning and evening conditions. With only few percent difference, both datasets match each other in the long-term average in the 15-22 km range for morning conditions and in the 18-27 km range for evening conditions (in this thesis, SCIAMACHY data from measurements at morning conditions are considered only).

GB UV VIS measurements are carried out at the site of Harestua since the mid 90s. The instrumentation is given by two grating spectrometers with zenith sky viewing direction, one measuring radiances

in the UV and the other in the visible spectral range [Van Roozendael et al., 1998]. They use photodiode array detectors which are cooled to allow for a better signal-to-noise ratio. The UV measurements cover the 330-390 nm spectral range and are utilised for retrieving BrO.

The GB UV VIS retrieval of vertical profiles of stratospheric BrO employs 2 major steps. In the first step, slant columns of BrO are retrieved using a DOAS (=Differential Optical Absorption Spectroscopy) approach [Theys et al., 2007]. In addition to BrO, the other absorbers accounted for by the DOAS approach are $\mathrm{NO_2}$, $\mathrm{O_3}$, $\mathrm{O_4}$, and OClO. Different from Hendrick et al. [2009], the wavelength range of Harestua GB UV VIS retrieval is 342-357 nm instead of 345-359 nm for the data used here. More improvements of the DOAS settings have been implemented by the NDACC UV-VIS Working Group, BIRA-IASB, in the mean-time (among others, the retrieval quality in winter months has been slightly improved by modified threshold settings). In the second retrieval step, a profiling technique based on the optimal estimation approach is applied [Hendrick et al., 2009, and references therein]. Thereby, low vertical resolution profiles of BrO for the solar zenith angle (sza) of 80° are obtained. As pointed out in Hendrick et al. [2009], the retrieval information is somewhat reduced at Harestua from end of October until mid February as only solar zenith angles larger than 80° are reached. Still, it is possible to retrieve results at a somewhat larger sza and adjust the results to 80° sza. The latter is accomplished by a stacked box photochemical model which is an integral part of the radiative transfer model used at the GB UV VIS retrieval.

12.2.2 Preparation of data

In the following, the record of stratospheric BrO from the NDACC station of Harestua is selected for a trend comparison to SCIAMACHY, in accordance with recommendation by the NDACC UV-VIS Working Group, BIRA-IASB. Only Harestua GB UV VIS data from measurements at PM local time, i.e. at afternoon/evening conditions, are used. This follows the previous trend study of Hendrick et al. [2008] (AM measurements have larger instrumental noise). Instead of stratospheric columns, the BrO number density at 21 km is under analysis

here.

Similar to Hendrick et al. [2009], SCIAMACHY limb BrO data are selected within ±5° latitude and ±10° longitude around the site of Harestua (60.2°N, 10.8°E). Photochemical variations of BrO during daytime are accounted for by scaling the SCIAMACHY data to a solar zenith angle of 80°, which is characteristic for the GB UV VIS measurements as described in Section 12.2.1. This photochemical correction is based on tables from the PRATMO photochemical box model as in Section 12.1.1 (here, no filter criteria are used).

GB UV VIS measurements have a vertical resolution of 10 to 12 km at best. As illustrated by averaging kernels typical for the station of Harestua at PM conditions, shown in Hendrick et al. [2009], the vertical resolution and measurement sensitivity with respect to BrO maximise at around 21 km. Hence, the trend comparison between SCIAMACHY and Harestua GB UV VIS is made at the altitude of 21 km. In the following, monthly mean averaging kernels for Harestua are used to convolve SCIAMACHY limb BrO, which has a finer vertical resolution of around 3-4 km (see Section 4.1). The convolution is applied to the profiles of BrO from SCIAMACHY after being monthly averaged and follows Equation (1) in Hendrick et al. [2009]:

$$x_{conv} = x_a + A(x_{scia} - x_a), \tag{12.2}$$

with x_{scia} denoting the original BrO profiles from SCIAMACHY and x_{conv} their convolution. A is the averaging kernel matrix of Harestua GB UV VIS and x_a its a priori data. The SCIAMACHY data are convolved over the full nominal altitude range of the BrO retrieval from 13-33 km. After the convolution, the SCIAMACHY data at 21 km should still be largely determined by the altitude range of high retrieval sensitivity, which is 16-26 km [Rozanov et al., 2011] (this is concluded from the GB UV VIS measurements having a vertical resolution of 10-12 km as mentioned before). Similar to Hendrick et al. [2009], additional convolution due to the finite vertical resolution of SCIAMACHY is neglected.

Both for SCIAMACHY and GB UV VIS, time series of monthly mean BrO are analysed over the period 08/2002-04/2012. For GB UV VIS, all data available from January to November are included (the indi-

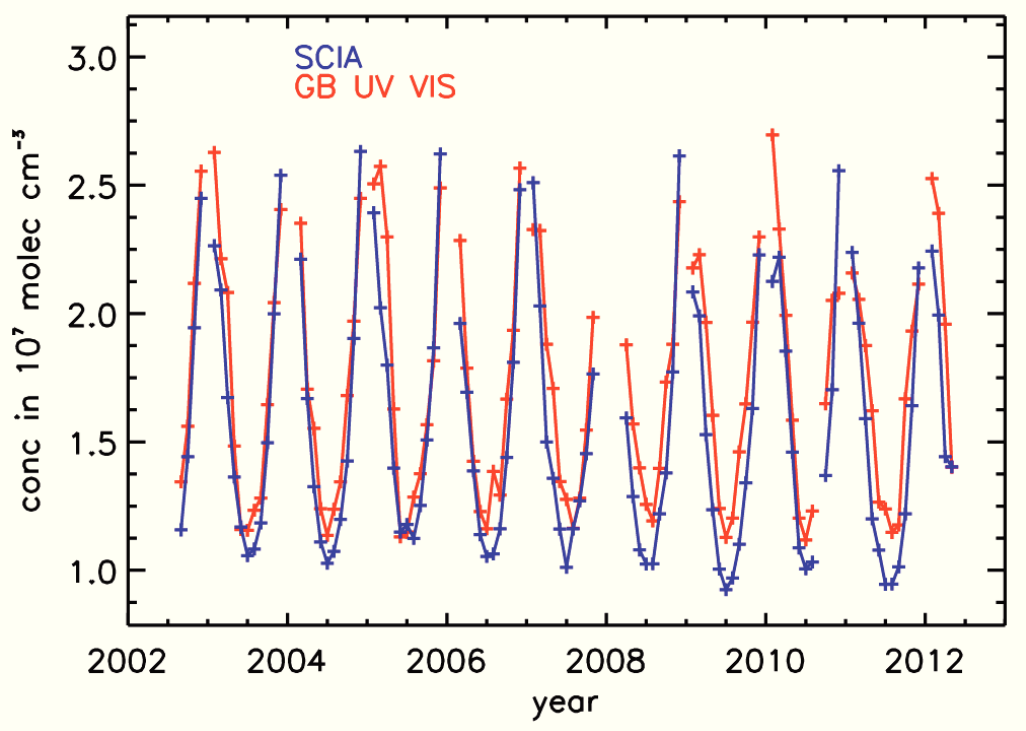

Figure 12.3: Time series of the BrO number density at the altitude of 21 km from SCIAMACHY and GB UV VIS measurements at Harestua. The data from SCIAMACHY have been selected at latitudes and longitudes close to the site of Harestua (60.2°N, 10.8°E). In addition, they were convoluted by the averaging kernels from GB UV VIS and photochemically corrected to a solar zenith angle of 80°.

vidual days of data availability are not necessarily identical to those in Hendrick et al. [2008] because of the improved retrieval settings described in Section 12.2.1). By implication, the time series from Harestua GB UV VIS have no data in the month of December. Sporadically, there are other months without data from Harestua (for different reasons). For those months, SCIAMACHY data are excluded from the analysis accordingly. Trends are determined by multivariate linear regression with the regression model comprising linear terms and harmonics of 12, 6, 4, and 3 month period. Data gaps are accounted for as described in Section 12.1.1.

12.2.3 Comparison of time series and trends

The BrO time series (for the altitude of 21 km) obtained from SCIAMACHY and GB UV VIS measurements at Harestua are plotted in Figure 12.3. Despite the photochemical correction and convolution, the time series from SCIAMACHY is similar to that for the 60°N-50°N

latitude band at 21 km described in Section 11.2 (see Figure 11.2). BrO undergoes a pronounced annual oscillation having its maximum in winter and minimum in summer. Time series gaps due to the missing of data from Harestua occur constantly in December and only sporadically in other months. The time series gaps amount for less than 10% of the analysed time span.

The time series from SCIAMACHY and GB UV VIS match each other closely. Some differences are evident before and after data gaps in December. This may be related to the retrieval quality being somewhat reduced at Harestua from late October to November and January to mid February as described in Section 12.2.1. The annual minima of BrO, which are observed in summer, are mostly seen by SCIAMACHY at values somewhat lower than GB UV VIS. While this is almost inapparent in the first years of the analysed time span, the annual minimum values drift notably apart from one another afterwards.

In Figures 12.4 and 12.5, both time series are shown in combination with their fit curve from the regression model. The latter is provided as the overall fit curve with all regression terms included and as the linear fit only. As can be concluded from the closure between the time series and their overall fit curves, sufficient fit quality is achieved. For both time series, the linear terms reflect decreases of BrO during the time span under study and the resulting trends are significant: -11.6±2.3 $\%dec^{-1}$ for SCIAMACHY and -5.0±2.5 $\%dec^{-1}$ for Harestua GB UV VIS (the latter has been checked to meet the significance criterion, given by Equation 6.11, without being rounded). The trend uncertainties are similar, but the trends do not agree within their uncertainties. The trend from SCIAMACHY is more negative than GB UV VIS by a factor of more than 2.

Different factors were considered as potential contributors to the discrepancy of trends. As discussed in Section 12.2.1, the data from Harestua may be affected by reduced retrieval quality particularly in the months of November and January. However, the record of Harestua GB UV VIS exhibits also a less pronounced decrease of BrO in summer time as described before. As pointed out in the validation study of Hendrick et al. [2009], the BrO retrieval of SCIAMACHY and Harestua use different absorption cross sections of BrO. This has,

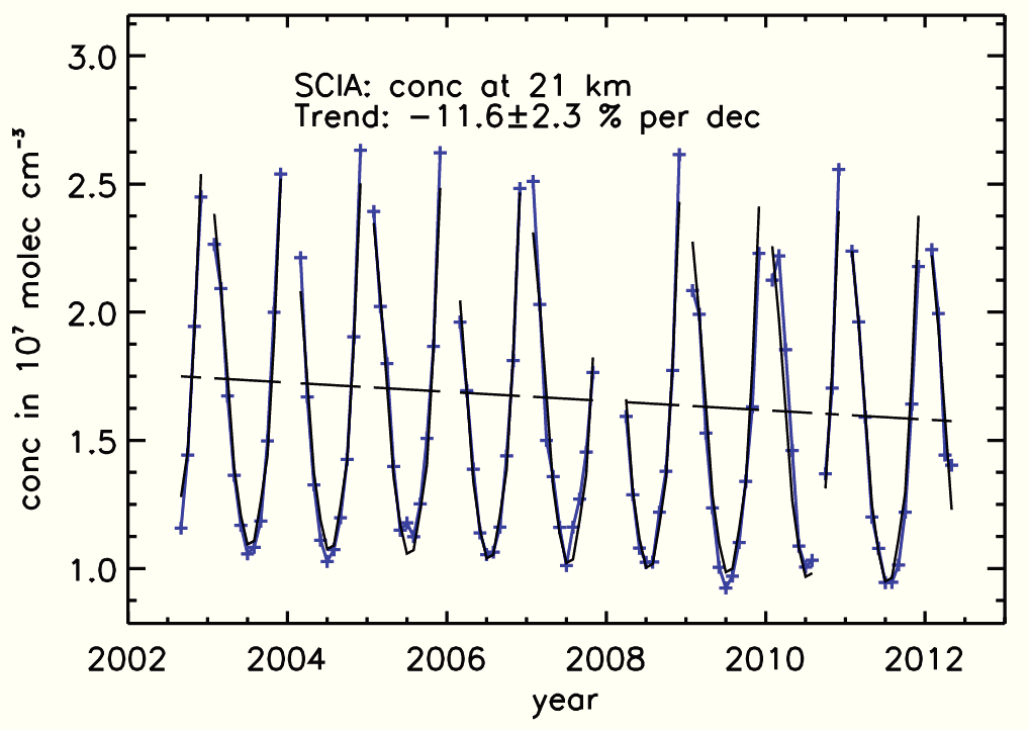

Figure 12.4: BrO time series from SCIAMACHY (blue) in combination with the fit curve from the regression model (black). The latter is provided as the overall fit curve and its linear part only.

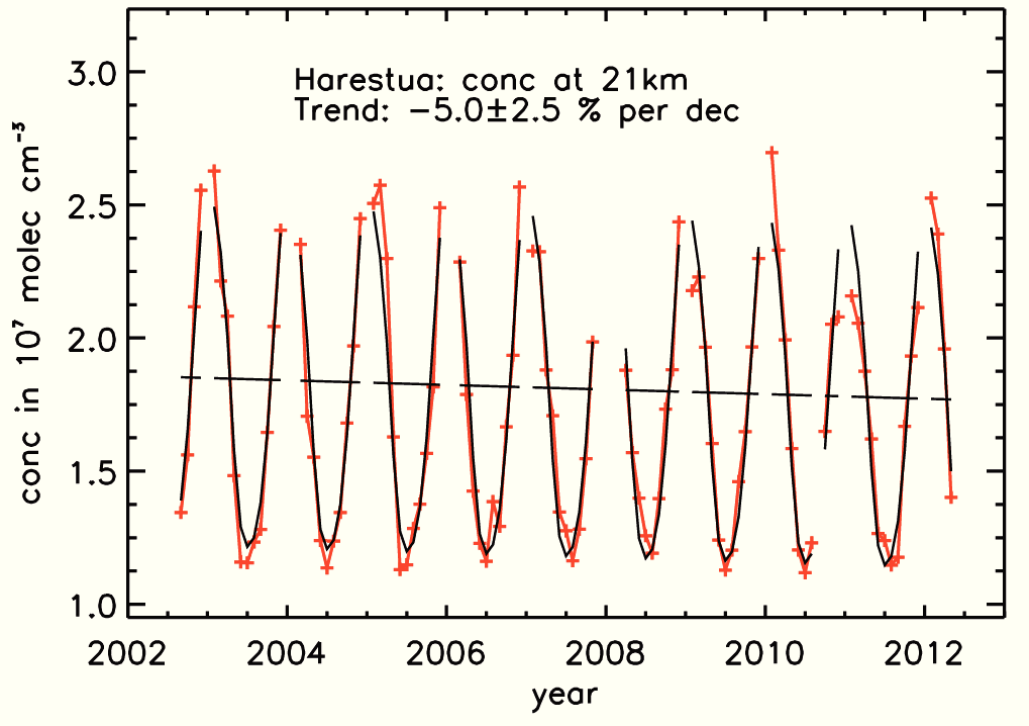

Figure 12.5: Same as Figure 12.4, but for GB UV VIS measurements at Harestua.

however, only the potential to distort BrO data by a constant factor as follows from Rozanov et al. [2011]. As BrO trends are provided in relative units, this is expected not to be of consequence. Other factors like the temporal sampling of data at Harestua could not be identified to be major sources of error either.

The convolution of SCIAMACHY limb BrO data with the averaging kernels of GB UV VIS is practically equivalent with convolution of the trends from SCIAMACHY over a broad altitude range. With the vertical resolution of GB UV VIS being of around 10-12 km, the SCIAMACHY BrO trend at 21 km is expected to be influenced by the non-convoluted trends within the 15-27 km range. It is worth mentioning that the discrepancy of trends at 21 km, obtained before, arises mainly from the altitudes below 20 km. This has been proven by inferring a non-convoluted vertical trend profile from SCIAMACHY: in the 20-27 km range, the trends do not exceed $-10\% dec^{-1}$ and agree with trend from Harestua GB UV VIS at 21 km, which is $-5.0 \pm 2.5\% dec^{-1}$, within the 1σ uncertainty. Below 19 km, the trends from SCIAMACHY become more negative and reach around $-15\% dec^{-1}$ at 17 km.

13 Summary and conclusion

13.1 O_3 related chapters

In this thesis, a comprehensive analysis of O_3 time series from SCIAMACHY limb measurements was performed. The latitude range from 60°N to 60°S and altitudes from 15 to 50 km were in the focus. The method of multivariate linear regression was applied. The regression terms accounted both for long-term changes and periodic variabilities in the O_3 time series. Long-term changes of O_3 were approximated by linear terms and quantified as linear changes/trends. Variabilities of O_3 on sub-decadal to decadal time scale were comprised such as (semi-)annual variations, the quasi-biennial oscillation, and signatures of the solar cycle and the El Niño Southern Oscillation. This proved to be a sufficiently complete approach. The fit residuals were typically within $\pm$5-10% of the time series.

The resulting O_3 trends were presented as a function of the altitude and latitude and potential drivers were discussed. One conclusion is that positive upper stratospheric O_3 trends seen by SCIAMACHY are similarly indicative of declining halogens as findings in related studies. In addition, positive O_3 trends in the lower tropical stratosphere and negative O_3 trends in the middle tropical stratosphere were identified from SCIAMACHY. Particularly in the lower tropical stratosphere, halogens are known to be rather ineffective at the O_3 depletion [Yang et al., 2006; WMO, 2007]. This leads to the expectation of these changes being controlled by drivers different from halogens. Combined effects from a shift of the subtropical mixing barriers/increase of the age of air and the NO_X chemistry were considered as one possible explanation.

Trend comparisons between SCIAMACHY and other measurements,

both from limb sounders (OSIRIS/Odin and EOS MLS) and balloon-borne ozonesondes (part of the SHADOZ network), were performed in the tropics and at midlatitudes. The comparisons to other limb sounders covered the 15-50 km range and those to ozonesondes the 15-30 km range. In the tropics, positive trends seen by SCIAMACHY were confirmed by OSIRIS, MLS, and SHADOZ in the lower stratosphere and by OSIRIS in the upper stratosphere. The comparison of SCIAMACHY, OSIRIS, and MLS showed negative trends for all three instruments in the middle tropical stratosphere. There is good qualitative agreement although the maximum values of the negative trends vary between the instruments. In the lowermost tropical stratosphere, all three instruments showed positive trends. MLS exhibited larger positive trends than SCIAMACHY and OSIRIS. Similarly, SHADOZ ozonesondes showed larger positive trends than SCIAMACHY in the inner tropics. At midlatitudes, the comparison of trends between SCIAMACHY and MLS showed good agreement. A hemispheric asymmetry of trends in the 25-35 km range was confirmed by MLS at southern midlatitudes and partly at northern midlatitudes. The trends from MLS agreed with positive trends seen by SCIAMACHY in the northern midlatitude upper stratosphere. A discrepancy between the trends from SCIAMACHY and MLS was found in the 30-35 km range at northern midlatitudes.

Potential sources of error with relevance to O_3 trends were investigated. Reduced retrieval sensitivity of SCIAMACHY limb measurements was discussed as one possible cause for the discrepancies found in the 30-40 km range.

13.2 BrO related Chapters

BrO time series from SCIAMACHY limb measurements were analysed in the 16-26 km altitude range and 60°N-60°S latitude range. This followed the method of multivariate linear regression. Linear changes/trends were derived using linear regression terms. Patterns of annual variability of BrO were approximated by harmonic regression terms. This approach was proven to achieve overall reasonable fit quality with fit residuals typically being within $\pm$5-10% of the analysed

time series. Only for the years from 2008 to 2011, fit residuals partly exceeding 10 % were found in the tropics and southern hemisphere.

As a function of the latitude and altitude, the overall pattern of BrO trends from SCIAMACHY limb measurements is practically everywhere significant negative. Here, only the trends with values not more negative than around -5 to -15 % per decade (this is the range of trends obtained at instrument comparisons, see below) are summarised. The trends are typically of around -10 % per decade in the northern hemisphere above 20 km and at southern midlatitudes. From the tropics to the southern subtropics/midlatitudes, the trends are between -10 and -20 % per decade in the 24-26 km range.

BrO trends from SCIAMACHY were compared to those from OSIRIS/Odin and ground-based measurements at Harestua. The comparison instruments confirmed a clear tendency towards negative changes in BrO. The comparison to OSIRIS/Odin was performed in the tropics at the altitudes of 24 and 26 km. In agreement, the trends from SCIAMACHY and OSIRIS/Odin were close to -15 % per decade. For the comparison to ground-based measurements, data from SCIAMACHY were selected close to the site of Harestua. While SCIAMACHY saw negative trends of around -10 % decade, the ground-based measurements at Harestua were at around -5 % decade.

Taken as a whole, the trends obtained at instrument comparisons vary between around -5 and -15 % per decade. On the order of magnitude, these trend values are consistent with the decrease of stratospheric bromine expected from the decrease of tropospheric source gases, which is roughly 5 % per decade as mentioned in Section 3.3. Stratospheric bromine having a general tendency to decline stronger than that remains speculative. To conclude, our findings are similarly indicative of a decline of the stratospheric bromine load as a consequence of the Montreal Protocol and its amendments as those in related studies.

Still, BrO time series and/or trends differ considerably from instrument to instrument. Further work is necessary for investigating potential sources of error in the individual datasets.

Bibliography

Adams, C., Bourassa, A. E., Sofieva, V., Froidevaux, L., McLinden, C. A., Hubert, D., Lambert, J.-C., Sioris, C. E., and Degenstein, D. A.: Assessment of Odin-OSIRIS ozone measurements from 2001 to the present using MLS, GOMOS, and ozonesondes, Atmos. Meas. Tech., 7, 49-64, doi:10.5194/amt-7-49-2014, 2014.

Andrews, D. G., Holton, J. R., and Leovy, C. B.: Middle Atmosphere Dynamics, Academic Press, San Diego, CA, 1987.

Aschmann, J., Sinnhuber, B.-M., Atlas, E. L., and Schauffler, S. M.: Modeling the transport of very short- lived substances into the tropical upper troposphere and lower stratosphere, Atmos. Chem. Phys., 9 (23), 9237-9247, doi: 10.5194/acp-9-9237-2009, 2009.

Aschmann, J., Burrows, J. P., Gebhardt, C., Rozanov, A., Hommel, R., Weber, M., and Thompson, A. M.: On the hiatus in the acceleration of tropical upwelling since the beginning of the 21st century, Atmos. Chem. Phys. Discuss., 14, 9951-9973, doi:10.5194/acpd-14-9951-2014, 2014.

Baldwin, M. P., Gray, L. J., Dunkerton, T. J., Hamilton, K., Haynes, P. H., Randel, W. J., Holton, J. R., Alexander, M. J., Hirota, I., Horinouchi, T., Jones, D. B. A., Kinnersley, J. S., Marquardt, C., Sata, K., and Takahashi, M.: The quasi-biennial oscillation, Rev. Geophys., 39, 179-229, doi:10.1029/1999RG000073, 2001.

Banwell, C. N. and McCash, E. M.: Fundamentals of molecular spectroscopy, McGraw-Hill, fourth edition, 1994.

Bates, D. R. and Nicolet, M.: The photochemistry of atmospheric water vapour, J. Geophys. Res., 55, 301, 1950.

Bergmann-Schäfer, Lehrbuch der Experimentalphysik, Bd.1, Mechanik, Akustik, Wärme; de Gruyter, Berlin, New York, 11. Auflage, 1998.

Bogumil, K., Orphal, J., Homann, T., Voigt, S., Spietz, P., Fleischmann, O. C., Vogel, A., Hartmann, M., Bovensmann, H., Frerick, J., and Burrows, J. P.: Measurements of molecular absorption spectra with the SCIAMACHY pre-flight model: instrument characterisation and reference data for atmospheric remote-sensing in the 230–2380 nm region, J. Photochem. Photobio. A., 157, 157–167, 2003.

Bourassa, A. E., Degenstein, D. A., Randel, W. J., Zawodny, J. M., Kyrölä, E., McLinden, C. A., Sioris, C. E., and Roth, C. Z.: Trends in stratospheric ozone derived from merged SAGE II and Odin-OSIRIS satellite observations, Atmos. Chem. Phys. Discuss., 14, 7113-7140, doi:10.5194/acpd-14-7113-2014, 2014.

Bovensmann, H., Burrows, J. P., Buchwitz, M., Frerick, J., Noël, S., Rozanov, V. V., Chance, K. V., and Goede, A. P. H.: SCIAMACHY: Mission Objectives and Measurement Modes, J. Atmos. Sci., 56, 127-150, 1999.

Bramstedt, K., Noël, S., Bovensmann, H., Gottwald, M., and Burrows, J. P.: Precise pointing knowledge for SCIAMACHY solar occultation measurements, Atmos. Meas. Tech., 5, 2867-2880, doi:10.5194/amt-5-2867-2012, 2012.

Brewer, A. W.: Evidence for a world circulation provided by the measurements of helium and water vapour distribution in the stratosphere, Q. J. R. Meteorol. Soc., 75, 351–363, 1949.

Brohede, S., McLinden, C. A., Berthet, G., Haley, C. S., Murtagh, D., Sioris, C. E.: A stratospheric NO_2 climatology from Odin/OSIRIS limb-scatter measurements, Can. J. Phys., 85(11), 1253-1274, doi: 10.1139/p07-141, 2007.

Burrows, J. P., Cliff, D. I., Harris, G. W., Thrush, B. A., and Wilkinson, J. P. T.: Atmospheric reactions of the HO_2 radical studied by laser magnetic resonance, P. R. Soc. A, 368, 463-481, 1979.

Burrows, J. P., Weber, M., Buchwitz, M., Rozanov, V. V., Ladstätter-Weißenmayer, A., Richter, A., DeBeek, R., Hoogen, R., Bramstedt, K., and Eichmann, K.-U.: The Global Ozone Monitoring Experiment (GOME): Mission Concept and First Scientific Results, J. Atmos. Sci., 56, 151-174, 1999.

Butchart, N., Scaife, A. A., Austin, J., Hare, S. H. E., and Knight, J. R.: Quasi-biennial oscillation in ozone in a coupled chemistry-climate model, J. Geophys. Res., 108, 4486, doi:10.1029/2002JD003004, 2003.

Butchart, N., Cionni, I., Eyring, V., Shepherd, T.G., Waugh, D. W., Akiyoshi, H., Austin, J., Brühl, C., Chipperfield, M. P., Cordero, E., Dameris, M., Deckert, R., Dhomse, S., Frith, S. M., Garcia, R. R., Gettelman, A., Giorgetta, M. A., Kinnison, D. E., Li, F., Mancini, E., McLandress, C., Pawson, S., Pitari, G., Plummer, D. A., Rozanov, E., Sassi, F., Scinocca, J. F., Shibata, K., Steil, B., and Tian, W.: Chemistry-climate model simulations of 21st century stratospheric climate and circulation changes, J. Clim., 23 (20), doi:10.1175/2010JCLI3404.1, 2010.

Butler, J. H., Battle, M., Bender, M. L., Montzka, S. A., Clarke, A. D., Saltzman, E. S., Sucher, C. M., Severinghaus, J. P. and Elkins, J. W.: A record of atmospheric halocarbons during the twentieth century from polar firn air, Nature, 399(6738), 749-755, doi:10.1038/21586, 1999.

Chapman, S.: A theory of upper-atmosphere ozone, Mem. Roy. Meteorol. Soc. 3, 103, 1930.

Chen, W. and Huang, R.: The propagation and transport effect of planetary waves in the Northern Hemisphere winter, Adv. Atmos. Sci., 19, ,1113-1126, 2002.

Chipperfield, M. P., Gray, L. J., Kinnersley, J. S., and Zawodny, J.: A Two-Dimensional Model Study of the QBO Signal in SAGE II NO_2 and O_3, Geophys. Res. Lett., 21, 589-592, doi:10.1029/94GL00211, 1994.

Crutzen, P. J.: The influence of nitrogen oxides on the atmospheric ozone content, Q. J. Roy. Meteorol. Soc., 96, 320-325, 1970.

Crutzen, P. J.: Estimates of possible future ozone reductions from continued use of fluorochloro-methanes (CF_2Cl_2, $CFCl_3$), Geophys. Res. Lett., 1, 205-208, 1974.

Degenstein, D. A., Bourassa, A. E., Roth, C. Z., and Llewellyn, E. J.: Limb scatter ozone retrieval from 10 to 60 km using a multiplicative algebraic reconstruction technique, Atmos. Chem. Phys., 9, 6521-6529, doi:10.5194/acp-9-6521-2009, 2009.

Deters, B., Burrows, J. P., and Orphal, J.: UV-visible absorption cross-sections of bromine nitrate determined by photolysis of $BrONO_2$/Br_2 mixtures, J. Geophys. Res., 103, 2156-2202, 1998.

Dhomse, S., Weber, M., Wohltmann, I., Rex, M., and Burrows, J. P.: On the possible causes of recent increases in northern hemispheric total ozone from a statistical analysis of satellite data from 1979 to 2003, Atmos. Chem. Phys., 6, 1165-1180, doi:10.5194/acp-6-1165-2006, 2006.

Dobson, G. M.: Origin and distribution of the polyatomic molecules in the atmosphere, Proc. Roy. Soc. Ldn., A236, 187–193, 1956.

Dorf, M., Butler, J. H., Butz, A., Camy-Peyret, C., Chipperfield, M. P., Kritten, L., Montzka, S. A., Simmes, B., Weidner, F., and Pfeilsticker, K.: Long-term observations of stratospheric bromine reveal slow down in growth, Geophys. Res. Lett., 33, L24803, doi:10.1029/2006GL027714, 2006

Eckert, E., von Clarmann, T., Kiefer, M., Stiller, G. P., Lossow, S., Glatthor, N., Degenstein, D. A., Froidevaux, L., Godin-Beekmann, S., Leblanc, T., McDermid, S., Pastel, M., Steinbrecht, W., Swart, D. P. J., Walker, K. A., and Bernath, P. F.: Drift-corrected trends and periodic variations in MIPAS IMK/IAA ozone measurements, Atmos. Chem. Phys., 14, 2571-2589, doi:10.5194/acp-14-2571-2014, 2014.

Edelson, R. A. and Krolik, J. H.: The discrete correlation function: A new method for analyzing unevenly sampled variability data, Astrophys. J., 333, 646-659, 1988.

Farman, J. C., Gardiner, B. G., and Shanklin, J. D.: Large losses of total ozone in Antarctica reveal seasonal ClO_X/NO_X interaction, Nature, 315, 207-10, 1985.

Fioletov, V. E.: Estimating the 27-day and 11-year solar cycle variations in tropical upper stratospheric ozone, J. Geophys. Res., 114, D02302, doi:10.1029/2008JD010499, 2009.

Fleischmann, O. C., Hartmann, M., Burrows, J. P., and Orphal, J.: New ultraviolet absorption cross-sections of BrO at atmospheric temperatures measured by time-windowing Fourier transform spectroscopy, J. Photoch. Photobio. A, 168, 117–132, 2004.

Fleming, E. L., Jackman, C. H., Stolarski, R. S., and Douglass, A. R.: A model study of the impact of source gas changes on the stratosphere for 1850-2100, Atmos. Chem. Phys., 11, 8515-8541, doi:10.5194/acp-11-8515-2011, 2011.

Flittner, D. E., Bhartia, P. K., and Herman, B. M.: O_3 profiles retrieved from limb-scatter measurements: Theory, Geophys. Res. Lett., 27, 2601 – 2604, 2000.

Froidevaux, L., Jiang, Y. B., Lambert, A., Livesey, N. J., Read, W. G., Waters, J. W., Browell, E. V., Hair, J. W., Avery, M. A., McGee, T. J., Twigg, L. W., Sumnicht, G. K., Jucks, K. W., Margitan, J. J., Sen, B., Stachnik, R. A., Toon, G. C., Bernath, P. F., Boone, C. D., Walker, K. A., Filipak, M. J., Fuller, R. A., Manney, G. L., Schwartz, M. J., Daffer, W. H., Drouin, B. J., Cofield, R. E., Cuddy, D. T., Jarnot, R. F., Knosp, B. W., Perun, V. S., Snyder, W. V., Stek, P. K., Thurstans, R. P., and Wagner, P. A.: Validation of Aura Microwave Limb Sounder stratospheric ozone measurements, J. Geophys. Res., 113, D15S20, doi:10.1029/2007JD008771, 2008.

Fussen, D. and Bingen, C.: A volcanism dependent model for the extinction profile of stratospheric aerosols in the UV-visible range, Geophys. Res. Lett., 26, 703–706, 1999.

Gebhardt, C., Rozanov, A., Hommel, R., Weber, M., Bovensmann, H., Burrows, J. P., Degenstein, D., Froidevaux, L., and Thompson, A. M.: Stratospheric ozone trends and variability as seen by SCIAMACHY from 2002 to 2012, Atmos. Chem. Phys., 14, 831-846, doi:10.5194/acp-14-831-2014, 2014.

Gottwald, M. and Bovensmann, H.: SCIAMACHY - Exploring the Changing Earth’s Atmosphere, Springer, Dordrecht, 2011.

Gray, L. J., Beer, J., Geller, M., Haigh, J. D., Lockwood, M., Matthes, K., Cubasch, U., Fleitmann, D., Harrison, G., Hood, L., Luterbacher, J., Meehl, G. A., Shindell, D., van Geel, B., and White, W.: Solar Influences on Climate, Rev. Geophys., 48, RG4001, doi:10.1029/2009RG000282, 2010.

Hendrick, F., Johnston, P. V., De Mazière, M., Fayt, C., Hermans, C., Kreher, K., Theys, N., Thomas, A., and Van Roozendael, M.: One-decade trend analysis of stratospheric BrO over Harestua (60°N) and Lauder (45°S) reveals a decline, Geophys. Res. Lett., 35, L14801, doi:10.1029/2008GL034154, 2008.

Hendrick, F., Rozanov, A., Johnston, P. V., Bovensmann, H., De Mazière, M., Fayt, C., Hermans, C., Kreher, K., Lotz, W., Sinnhuber, B.-M., Theys, N., Thomas, A., Burrows, J. P., and Van Roozendael, M.: Multi-year comparison of stratospheric BrO vertical profiles retrieved from SCIAMACHY limb and ground-based UV-visible measurements, Atmos. Meas. Tech., 2, 273-285, 2009.

Jackman, C. H., Fleming, E. L., Chandra, S., Considine, D. B., and Rosenfield, J. E.: Past, present, and future modeled ozone trends with comparisons to observed trends, J. Geophys. Res., 101, 28753-28767, 1996.

Jones, A., Urban, J., Murtagh, D. P., Eriksson, P., Brohede, S., Haley, C., Degenstein, D., Bourassa, A., v. Savigny, C., Sonkaew, T., Rozanov, A., Bovensmann, H., and Burrows, J. P.: Evolution of stratospheric ozone and water vapour time series studied with satellite measurements, Atmos. Chem. Phys., 9, 6055-6075, doi:10.5194/acp-9-6055-2009, 2009.

Kyrölä, E., Laine, M., Sofieva, V., Tamminen, J., Päivärinta, S.-M., Tukiainen, S., Zawodny, J., and Thomason, L.: Combined SAGE II-GOMOS ozone profile data set for 1984–2011 and trend analysis of the vertical distribution of ozone, Atmos. Chem. Phys., 13, 10645–10658, doi:10.5194/acp-13-10645-2013, 2013.

Lary, D. J.: Gas phase atmospheric bromine photochemistry, J. Geophys. Res. D, 101, 1505–1516, 1996.

Llewellyn, E. J., Lloyd, N. D., Degenstein, D. A., Gattinger, R. L., Petelina, S. V., Bourassa, A. E., Wiensz, J. T., Ivanov, E. V., McDade, I. C., Solheim, B. H., McConnell, J. C., Haley, C. S., v. Savigny, C., Sioris, C. E., McLinden, C. A., Griffioen, E., Kaminski, J., Evans, W. F. J., Puckrin, E., Strong, K., Wehrle, V., Hum, R. H., Kendall, D. J. W., Matsushita, J., Murtagh, D. P., Brohede, S., Stegman, J., Witt, G., Barnes, G., Payne, W. F., Piché, L., Smith, K., Warshaw, G., Deslauniers, D.-L., Marchand, P., Richardson, E. H., King, R. A., Wevers, I., McCreath, W., Kyrölä, E., Oikarinen, L., Leppelmeier, G. W., Auvinen, H., Mégie, G., Hauchecorne, A., Lefèvre, F., de La Nöe, J., Ricaud, P., Frisk, U., Sjoberg, F., von Schéele, F., and Nordh, L.: The OSIRIS instrument on the Odin spacecraft, Can. J. Phys., 82, 411-422, 2004.

Matthews, E.: Global vegetation and land use: new high resolution data bases for climate studies, J. Appl. Meteorol., 22, 474–487, 1983.

McElroy, M. B., Salawitch, R. J., Wofsy, S. C., and Logan, J. A.: Reductions Of Antarctic Ozone Due To Synergistic Interactions Of Chlorine And Bromine, Nature, 321, 759–762, doi:10.1038/321759a0, 1986.

McLinden, C. A. and Fioletov, V.: Quantifying stratospheric ozone trends: Complications due to stratospheric cooling, Geophys. Res. Lett., 38, L03808, doi:10.1029/2010GL046012, 2011.

McLinden, C. A., Haley, C. S., Lloyd, N. D., Hendrick, F., Rozanov, A., Sinnhuber, B.-M., Goutail, F., Degenstein, D. A., Llewellyn, E. J., Sioris, C. E., Van Roozendael, M., Pommereau, J. P., Lotz, W., and Burrows, J. P.: Odin/OSIRIS observations of stratospheric BrO: Retrieval methodology, climatology, and inferred Bry, J. Geophys. Res., 115, D15, doi:10.1029/2009JD012488, 2010.

McLinden, C. A., Bourassa, A. E., Brohede, S., Cooper, M., Degenstein, D. A., Evans, W.J. F., Gattinger, R. L., Haley, C. S., Llewellyn, E. J., Lloyd, N. D., Loewen, P., Martin, R. V., McConnell, J. C., McDade, I. C., Murtagh, D., Rieger, L., v. Savigny, C., Sheese, P. E., Sioris, C. E., Solheim, B., and Strong, K.: OSIRIS - A Decade of Scattered Light, B. Am. Meteorol. Soc., 93, pp. 1845-1863, doi: http://dx.doi.org/10.1175/BAMS-D-11-00135.1, 2012.

Mieruch, S., Weber, M., v. Savigny, C., Rozanov, A., Bovensmann, H., Burrows, J. P., Bernath, P. F., Boone, C. D., Froidevaux, L., Gordley,

L. L., Mlynczak, M. G., Russell III, J. M., Thomason, L. W., Walker, K. A., and Zawodny, J. M.: Global and long-term comparison of SCIAMACHY limb ozone profiles with correlative satellite data (2002-2008), Atmos. Meas. Tech., 5, 771-788, doi:10.5194/amt-5-771-2012, 2012.

Molina, M. J. and Rowland, F. S.: Stratospheric sink for chlorofluoromethanes: chlorine atom catalysed destruction of ozone, Nature, 249, 810–812, 1974.

Molina, L. T. and Molina, M. J.: Production of Cl_2O_2 from the Self-Reaction of the ClO Radical, J. Phys. Chem., 91, 433–436, 1987.

Montzka, S. A. and Fraser, P. J. (Lead Authors), Butler, J. H., Cunnold, D., Daniel, J., Derwent, D., Connell, P., Lal, S., McCulloch, A., Oram, D., Reeves, C., Sanhueza, E., Steele, P., Velders, G. J. M., Weiss, R. F., and Zander, R.: Controlled substances and other source gases, Chapter 1 in Scientific Assessment of Ozone Depletion: 2002, Global Ozone Research and Monitoring Project–Report No. 47, World Meteorological Organization, Geneva, Switzerland, 2003.

Montzka, S. A., Butler, J. H., Hall, B. D., Mondeel, D. J., and Elkins, J. W.: A decline in tropospheric organic bromine, Geophys. Res. Lett., 30(15), doi:10.1029/2003GL017745, 2003.

Naujokat, B.: An update of the observed Quasi-Biennial Oscillation of stratospheric winds over the tropics, J. Atmos. Sci., 43, 1873-1877, 1986.

Nedoluha, G. E., Siskind, D. E., Lambert, A., and Boone, C.: The Dynamical Implications of Changes in mid-Stratospheric Ozone since 1991, submitted to J. Geophys. Res..

Nevison, C. D. and Holland, E. A.: A reexamination of the impact of anthropogenically fixed nitrogen on atmospheric N_2O and the stratospheric O_3 layer, J. Geophys. Res., 102, 25519-25536, 1997.

Nevison, C. D., Solomon, S., and Gao, R. S.: Buffering interactions in the modeled response of stratospheric O_3 to increased NO_X and HO_X, J. Geophys. Res., 104, 3741-3754, doi:10.1029/1998JD100018, 1999.

Newchurch, M. J., Yang, E.-S., Cunnold, D. M., Reinsel, G. C., Zawodny, J. M., and Russell III, J. M.: Evidence for slowdown in stratospheric ozone loss: First stage of ozone recovery, J. Geophys. Res., 108, 4507, doi:10.1029/2003JD003471, 2003.

Noxon, J. F.: Stratospheric NO_2: 2. Global behavior, J. Geophys. Res., 84, 2156-2202, doi:10.1029/JC084iC08p05067, 1979.

Oman, L. D., Douglass, A. R., Ziemke, J. R., Rodriguez, J. M., Waugh, D. W., and Nielsen, J. E.: The ozone response to ENSO in Aura satellite measurements and a chemistry-climate simulation, J. Geophys. Res., 118(2), 965–976, doi:10.1029/2012JD018546, 2013.

Osterman, G. B., Salawitch, R. J., Sen, B., Toon, G. C., Stachnik, R. A., Pickett, H. M., Margitan, J. J., and Peterson, D. B.: Balloon-borne measurements of stratospheric radicals and their precursors: Implications for the production and loss of ozone, Geophys. Res. Lett., 24, 1107-1110, 1997.

Perliski, L.M., Solomon, S., and London, J.: On the interpretation of seasonal variations of stratospheric ozone, Planet. Space Sci., 37, 1527-1538, 1989.

Plumb, R. A.: Stratospheric Transport, J. Meteor. Soc. Japan, 80, 793-809, 2002.

Portmann, R. W. and Solomon, S.: Indirect radiative forcing of the ozone layer during the 21st century, Geophys. Res. Lett., 34, L02813, doi:10.1029/2006GL028252, 2007.

Rahpoe, N., v. Savigny, C., Weber, M., Rozanov, A. V., Bovensmann, H., and Burrows, J. P.: Error budget analysis of SCIAMACHY limb ozone profile retrievals using the SCIATRAN model, Atmos. Meas. Tech., 6, 2825-2837, doi:10.5194/amt-6-2825-2013, 2013.

Randel, W. J. and Wu, F.: A stratospheric ozone profile data set for 1979–2005: Variability, trends, and comparisons with column ozone data, J. Geophys. Res., 112, 2156-2202, doi:10.1029/2006JD007339, 2007.

Randel, W. J. and Thompson, A. M.: Interannual variability and trends in tropical ozone derived from SAGE II satellite data

and SHADOZ ozonesondes, J. Geophys. Res., 116, D07303, doi:10.1029/2010JD015195, 2011.

Randel, W. J., Park, M., Wu, F., and Livesey, N: A large annual cycle in ozone above the tropical tropopause linked to the Brewer-Dobson circulation, J. Atmos. Sci., 64, 4479-4488, 2007.

Randel, W. J., Shine, K. P., Austin, J., Barnett, J., Claud, C., Gillett, N. P., Keckhut, P., Langematz, U., Lin, R., Long, C., Mears, C., Miller, A., Nash, J., Seidel, D. J., Thompson, D. W. J., Wu, F., and Yoden, S.: An update of observed stratospheric temperature trends, J. Geophys. Res., 114, 2156-2202, doi:10.1029/2008JD010421, 2009, a).

Randel, W. J., Garcia, R. R., Calvo, N., and Marsh, D.: ENSO influence on zonal mean temperature and ozone in the tropical lower stratosphere, Geophys. Res. Lett., 36, L15822, doi:10.1029/2009GL039343, 2009, b).

Ravishankara, A. R., Daniel, J. S., and Portmann, R. W.: Nitrous Oxide (N_2O): The Dominant Ozone-Depleting Substance Emitted in the 21st Century, Science, 326, 123 – 125, doi:10.1126/science.1176985, 2009.

Remsberg, E. and Lingenfelser, G.: Analysis of SAGE II ozone of the middle and upper stratosphere for its response to a decadal-scale forcing, Atmos. Chem. Phys., 10, 11779-11790, doi:10.5194/acp-10-11779-2010, 2010.

Rosenfield, J. E., Frith, S. M., and Stolarski, R. S.: Version 8 SBUV ozone profile trends compared with trends from a zonally averaged chemical model, J. Geophys. Res., 110, 2156-2202, 2005.

Rozanov, A., Eichmann, K.-U., v. Savigny, C., Bovensmann, H., Burrows, J. P., von Bargen, A., Doicu, A., Hilgers, S., Godin-Beekmann, S., Leblanc, T., and McDermid, I. S.: Comparison of the inversion algorithms applied to the ozone vertical profile retrieval from SCIAMACHY limb measurements, Atmos. Chem. Phys., 7, 4763-4779, doi:10.5194/acp-7-4763-2007, 2007.

Rozanov, A., Kühl, S., Doicu, A., McLinden, C., Pukite, J., Bovensmann, H., Burrows, J. P., Deutschmann, T., Dorf, M., Goutail, F., Grunow,

K., Hendrick, F., von Hobe, M., Hrechanyy, S., Lichtenberg, G., Pfeilsticker, K., Pommereau, J. P., Van Roozendael, M., Stroh, F., and Wagner, T.: BrO vertical distributions from SCIAMACHY limb measurements: comparison of algorithms and retrieval results, Atmos. Meas. Tech., 4, 1319-1359, doi:10.5194/amt-4-1319-2011, 2011.

Rozanov, V. V., Rozanov, A. V., Kokhanovsky, A. A., and Burrows, J. P.: Radiative transfer through terrestrial atmosphere and ocean: Software package SCIATRAN, J. QUANT. SPECTROSC. RA., 133, 13B-71, 2014.

v. Savigny, C., Kaiser, J. W., Bovensmann, H., Burrows, J. P., McDermid, I. S., and Leblanc, T.: Spatial and temporal characterization of SCIAMACHY limb pointing errors during the first three years of the mission, Atmos. Chem. Phys., 5, 2593-2602, doi:10.5194/acp-5-2593-2005, 2005.

Sheode, N., Sinnhuber, B.-M., Rozanov, A., and Burrows, J. P.: Towards a climatology of stratospheric bromine monoxide from SCIAMACHY limb observations, Atmos. Chem. Phys. Discuss., 6, 6431-6466, 2006.

Sinnhuber, B.-M., Rozanov, A., Sheode, N., Afe, O. T., Richter, A., Sinnhuber, M., Wittrock, F., Burrows, J. P., Stiller, G. P., von Clarmann, T., and Linden, A.: Global observations of stratospheric bromine monoxide from SCIAMACHY, Geophys. Res. Lett., 32, 1944-8007, doi:10.1029/2005GL023839, 2005.

Sioris, C. E., McLinden, C. A., Fioletov, V. E., Adams, C., Zawodny, J. M., Bourassa, A. E., Roth, C. Z., and Degenstein, D. A.: Trend and variability in ozone in the tropical lower stratosphere over 2.5 solar cycles observed by SAGE II and OSIRIS, Atmos. Chem. Phys., 14, 3479-3496, doi:10.5194/acp-14-3479-2014, 2014.

Soukharev, B. E. and Hood, L. L.: Solar cycle variation of stratospheric ozone: Multiple regression analysis of long-term satellite data sets and comparisons with models, J. Geophys. Res., 111, D20314, doi:10.1029/2006JD007107, 2006.

SPARC CCMVal (2010), SPARC Report on the Evaluation of Chemistry-Climate Models, V. Eyring, T. G. Shepherd, D. W. Waugh (Eds.),

SPARC Report No. 5, WCRP-132, WMO/TD-No. 1526, http://www.atmosp.physics.utoronto.ca/SPARC.

Stahel, W. A.: Statistische Datenanalyse: eine Einführung für Naturwissenschaftler, Vieweg, Braunschweig, 2000.

Steinbrecht, W., Claude, H., Schönenborn, F., McDermid, I. S., Leblanc, T., Godin, S., Song, T., Swart, D. P. J., Meijer, Y. J., Bodeker, G. E., Connor, B. J., Kämpfer, N., Hocke, K., Calisesi, Y., Schneider, N., de la Noë, J., Parrish, A. D., Boyd, I. S., Brühl, C., Steil, B., Giorgetta, M. A., Manzini, E., Thomason, L. W., Zawodny, J. M., McCormick, M. P., Russel III, J. M., Bhartia, P. K., Stolarski, R. S., and Hollandsworth-Frith, S. M.: Long-term evolution of upper stratospheric ozone at selected stations of the Network for the Detection of Stratospheric Change (NDSC), J. Geophys. Res., 111, D10308, doi:10.1029/2005JD006454, 2006.

Steinbrecht, W., Claude, H., Schönenborn, F., McDermid, I. S., Leblanc, T., Godin-Beekmann, S., Keckhut, P., Hauchecorne, A., Van Gijsel, J. A. E., Swart, D. P. J., Bodeker, G. E., Parrish, A., Boyd, I. S., Kämpfer, N., Hocke, K., Stolarski, R. S., Frith. S. M., Thomason, L. W., Remsberg, E. E., v. Savigny, C., Rozanov, A., and Burrows, J. P.: Ozone and temperature trends in the upper stratosphere at five stations of the Network for the Detection of Atmospheric Composition Change, Int. J. Remote Sens. , 30, 3875-3886, 2009.

Stiller, G. P., von Clarmann, T., Haenel, F., Funke, B., Glatthor, N., Grabowski, U., Kellmann, S., Kiefer, M., Linden, A., Lossow, S., and López-Puertas, M.: Observed temporal evolution of global mean age of stratospheric air for the 2002 to 2010 period, Atmos. Chem. Phys., 12, 3311-3331, doi:10.5194/acp-12-3311-2012, 2012.

Stolarski, R. S., and Cicerone, R. J.: Stratospheric chlorine: a possible sink for ozone, Can. J. Chem., 52, 1610–1615, 1974.

Tanii, R. and Hasebe, F.: Ozone feedback stabilizes the quasi-biennial oscillation against volcanic perturbations, Geophys. Res. Lett., 29, doi:10.1029/2001GL013965, 2002.

Tegtmeier, S., Hegglin, M. I., Anderson, J., Bourassa, A., Brohede, S., Degenstein, D., Froidevaux, L., Fuller, R., Funke, B., Gille, J.,

Jones, A., Kasai, Y., Krüger, K., Kyrölä, E., Lingenfelser, G., Lumpe, J., Nardi, B., Neu, J., Pendlebury, D., Remsberg, E., Rozanov, A., Smith, L., Toohey, M., Urban, J., von Clarmann, T., Walker, K. A., and Wang, R. H. J.: SPARC Data Initiative: A comparison of ozone climatologies from international satellite limb sounders, J. Geophys. Res. Atmos., 118, 12229–12247, doi:10.1002/2013JD019877, 2013.

Theys, N., Van Roozendael, M., Hendrick, F., Fayt, C., Hermans, C., Baray, J.-L., Goutail, F., Pommereau, J.-P., and De Mazière, M.: Retrieval of stratospheric and tropospheric BrO columns from multi-axis DOAS measurements at Reunion Island (21°S, 56°E), Atmos. Chem. Phys., 7, 4733-4749, 2007.

Thompson, A.M., Witte, J. C., McPeters, R. D., Oltmans, S. J., Schmidlin, F. J., Logan, J. A., Fujiwara, M., Kirchhoff, V. W. J. H., Posny, F., Coetzee, G. J. R., Hoegger, B., Kawakami, S., Ogawa, T., Johnson, B. J., Vömel, H., and Labow, G.: Southern Hemisphere Additional Ozonesondes (SHADOZ) 1998-2000 tropical ozone climatology 1. Comparison with Total Ozone Mapping Spectrometer (TOMS) and ground-based measurements, J. Geophys. Res., 108, 8238, doi:10.1029/2001JD000967, 2003.

Thompson, A. M., Witte J. C., Oltmans, S. J., and Schmidlin, F. J.: SHADOZ - A tropical ozonesonde-radiosonde network for the atmospheric community, Bull. Am. Met. Soc., 85, 1549-1564,DOI: 10.1175/BAMS-85-10-1549, 2004.

Tian, W., Chipperfield, M. P., Gray, L. J., and Zawodny, J. M.: Quasi-biennial oscillation and tracer distributions in a coupled chemistry-climate model, J. Geophys. Res., 111, D20301, doi:10.1029/2005JD006871, 2006.

Tiao, G. C., Reinsel, G. C., Xu, D., Pedrick, J. H., Zhu, X., Miller, A. J., DeLuisi, J. J., Mateer, C. L., and Wuebbles, D. J.: Effects of autocorrelation and temporal sampling schemes on estimates of trend and spatial correlation, J. Geophys. Res., 95(D12), 20507-20517, doi:10.1029/JD095iD12p20507, 1990.

Van Roozendael, M., Fayt, C., Hermans, C., and Lambert, J.-C.: Ground-based UV-visible Measurements of BrO, $\mathrm{NO_2}$, $\mathrm{O_3}$ and OClO at

Harestua (60°N) since 1994, Proceedings of the 4th European Workshop on Polar Stratospheric Ozone, Schliersee, Germany, 22–26 Sept 1997, Air Pollution Research Report no 66, European Commission – DG XII, Brussels, 1998.

Wallace, J. M. and Hobbs, P. V.: Atmospheric Science - An introductory survey, Second Edition, Elsevier, 2006.

Wayne, R. P.: Chemistry of Atmospheres, Oxford University Press, New York, 1985, 1991, 2000, reprinted 2006.

Weatherhead, E. C., Reinsel,G. C., Tiao, G.C., Meng, X.-L., Choi, D., Cheang, W.-K., Keller, T., DeLuisi, J., Wuebbles, D. J., Kerr, J. B., Miller, A. J., Oltmans, S. J., and Frederick, J. E.: Factors affecting the detection of trends: Statistical considerations and applications to environmental data, J. Geophys. Res., 103, 17149–17161, doi: 10.1029/98JD00995, 1998.

Weber, M., Dikty, S., Burrows, J. P., Garny, H., Dameris, M., Kubin, A., Abalichin, J., and Langematz, U.: The Brewer-Dobson circulation and total ozone from seasonal to decadal time scales, Atmos. Chem. Phys., 11, 11221-11235, doi:10.5194/acp-11-11221-2011, 2011.

Weber, M., Pagaran, J., Dikty, S., v. Savigny, C., Burrows, J. P, DeLand, M., Floyd, L. E., Harder, J. W., Mlynczak, M. G., and Schmidt, H.: Investigation of solar irradiance variations and their impact on middle atmospheric ozone, Chapter 3, doi:10.1007/978-94-007-4348-9_3, in: Climate And Weather of the Sun-Earth System (CAWSES): Highlights from a priority program, ed. F.-J. Lübken, Springer, Dordrecht, The Netherlands, 2013.

World Meteorological Organization, Scientific Assessment of Ozone Depletion: 1998, WMO Global Ozone Research and Monitoring Project - Report No. 44, 1999.

World Meteorological Organization, Scientific Assessment of Ozone Depletion: 2002, WMO Global Ozone Research and Monitoring Project - Report No. 47, 2003.

World Meteorological Organization, Scientific Assessment of Ozone Depletion: 2006, WMO Global Ozone Research and Monitoring Project - Report No. 50, 2007.

World Meteorological Organization, Scientific Assessment of Ozone Depletion: 2010, WMO Global Ozone Research and Monitoring Project - Report No. 52, 2011.

Yang, E.-S., Cunnold, D. M., Salawitch, R. J., McCormick, M. P., Russell III, J. M., Zawodny, J. M., Oltmans, S., and Newchurch, M. J.: Attribution of recovery in lower-stratospheric ozone, J. Geophys. Res., 111, D17309, doi:10.1029/2005JD006371, 2006.

Ziemke, J. R., Chandra, S., Oman, L. D., and Bhartia, P. K.: A new ENSO index derived from satellite measurements of column ozone, Atmos. Chem. Phys., 10, 3711-3721, doi:10.5194/acp-10-3711-2010, 2010.

Erklärung

Hiermit erkläre ich, dass ich die Arbeit ohne fremde Hilfe angefertigt habe, dass ich keine anderen als die angegebenen Quellen und Hilfsmittel benutzt und die den benutzten Werken wörtlich oder inhaltlich entnommenen Stellen als solche kenntlich gemacht habe.

Claus Gebhardt

Acknowledgement

I thank Prof. J. P. Burrows and Dr. M. Weber for the opportunity to work at the Institute of Environmental Physics, University of Bremen. As well, I acknowledge the financial funding of my work by the DFG Research Unit SHARP (FOR 1095).

I am grateful to Dr. A. Rozanov and Dr. M. Weber for supervising my PHD studies. In particular, I acknowledge their great expertise in the field of my research and the very fruitful discussion with me. In addition, I would like to thank the limb satellite group and atmospheric modelling group of the Institute for their professional support.

I thank all colleagues from the Institute and the whole team involved in the satellite mission SCIAMACHY/ENVISAT. The data record from SCIAMACHY limb measurements was the basis for this PHD thesis. In addition, I thank our external partners for the valuable exchange of information, in particular for sharing their measurement data with us.